A Theoretical Study of Stress Induced Slip at Polymer-Polymer Interfaces

A THESIS
SUBMITTED TO THE FACULTY OF THE GRADUATE SCHOOL
OF THE UNIVERSITY OF MINNESOTA
BY

Andrew Aaron Gustafson

IN PARTIAL FULFILLMENT OF THE REQUIREMENTS
FOR THE DEGREE OF
DOCTOR OF PHILOSOPHY

David Morse, Advisor

December, 2013

For Katie, and for Mom, Dad, Franny, and Simon.

Contents

List of Tables

List of Figures

Chapter 1

Introduction

Polymers are chain molecules made up of simple repeating chemical units. These repeating units, called monomers, are covalently bonded, and a polymer could be composed of tens to many thousands of them. Polymer molecules vary in characteristics such as stiffness and length. Some polymers contain branches while others do not. This work examines unbranched linear polymers long enough to be flexible. Solutions of linear flexible polymers share many universal characteristics regardless of their particular chemical makeup.

When many polymers are combined into a liquid the result is a complex fluid with properties partially governed by polymer interactions. In concentrated solutions the polymers become entangled with each other, and this has a significant effect on the response of the fluid to strain. When polymers become entangled, interactions between the polymer chains, and the fact that they cannot pass through each other (topological interactions), affect the polymer behavior. In particular, topological interactions affect the transmission of stress, and the time it takes for polymers to equilibrate or relax following a deformation. The particular polymer liquids examined in this work are known as "melts"; a polymer melt is composed entirely of polymer

molecules with no solvent present. As liquid-like substances polymer melts tend to be incompressible, and are treated as such in this work.

Some polymers experience repulsive interactions with polymers of certain other chemical species. A mixture of two such immiscible (repelling, non-mixing) polymers will tend to separate into pure species regions similar to the way oil and water separate. At the boundary between the two separated regions there will in general be a lower viscosity (lower resistance to flow under an applied force). For this reason when a stress is applied to such a system it often results in a "slip" between the two different species polymer melts. The velocity of the slip and the stress transmitted across the interface during slip are affected by the entanglements between the two polymer species.

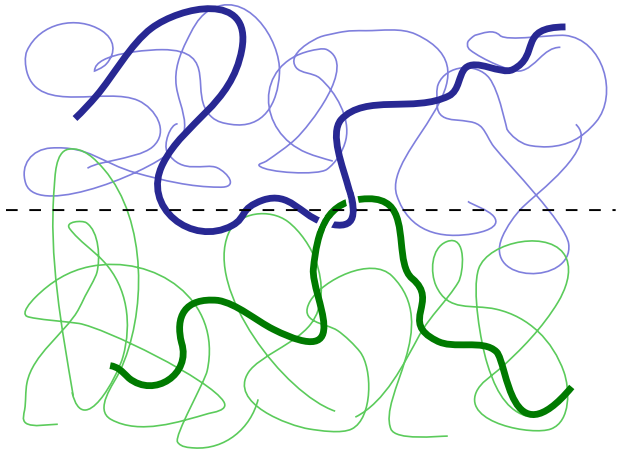

Figure 1.1: An illustration of a planar interface between immiscible polymer melts at equilibrium. The polymers are of two different immiscible chemical species, and consequently they separate into different melt regions. At the interface between the two melts the viscosity is lower than in either polymer bulk. If a force parallel to the interfacial plane is applied to the system it results in a "slip" at the interface. In such a situation the interfacial stress and slip velocity are affected by entanglements between the two melts. Here two polymers of different chemical species which are entangled at the interface are highlighted to illustrate the idea of interfacial entanglement. The dotted line represents the plane along which the average concentrations of each polymer species are equal; this is referred to as the interfacial plane.

The purpose of this work is to examine the phenomenon of slip at entangled planar interfaces between immiscible polymer melts. This phenomenon is examined through theory and simulation in order to develop predictions for the relationship between the interfacial stress (force per area) and the slip velocity. Some previous theoretical and experimental work has been done on the topic of polymer-polymer interfacial slip, and the current state of knowledge in this area is briefly examined below in Section 1.2 and in more detail during the history review in Chapter 2.

1.1 Polymer Melts

Polymer melts are densely packed collections of polymers with no solvent present. In homo-polymer melts all of the polymers are of the same chemical species. Polymer melts often behave as visco-elastic liquids; that is, polymer melts exhibit both viscous flow, and elastic response, when subjected to external forces. The degree to which a melt exhibits viscous or elastic behavior depends on variables including properties of the melt (such as degree of entanglement, and polymer length), the rate of deformation the melt is subjected to, and the time scale being considered.

In a homo-polymer melt in equilibrium, the conformation of any single polymer can usually be approximated as a random walk. An accurate random walk description requires that the polymer be long enough relative to any "stiffness" in the polymer backbone that sections of the polymer can be considered to have independent orientations (the random walk "step size" must be at least as large as such polymer sections). Because all of the polymers in a homo-polymer melt are of the same chemical species any single polymer will have the same energy interactions whether in contact with itself or with a neighboring polymer. For this reason a polymer residing in a melt will tend to have a randomly wandering conformation, as opposed to a polymer located in a solvent in which solvent-philic (or phobic) interactions could cause the polymer to expand (or contract).

Any sufficiently long polymer located in a melt is partly topologically confined by the neighboring polymer molecules. The motion of a polymer is consequently partially constricted by these topological interactions. A method of understanding this was proposed by de Gennes [1] in the concept of reptation. Reptation (from the Latin *reptar*: to creep or slither) refers to diffusive motion of a polymer directed approximately along its own length. When located in a melt a polymer is roughly

confined by its neighbors to a tube-like region of space along its own length. This topological confinement restricts polymer diffusion perpendicular to its length, but diffusion along its length is possible. It was argued by de Gennes that polymer reptation is the primary mechanism by which entangled polymers move, and that the polymer melt relaxation time is the "reptation time", which is the time it takes for a polymer to diffuse along its own length into entirely new surroundings. The reptation picture was successful in explaining many aspects of polymer melt stress behavior, and is described in greater detail in Chapter 2.

1.2 Previous Studies

Understanding the phenomena of stress induced slip at polymer-polymer interfaces is relevant to a number of commercial and scientific materials and processes. For example, understanding the phenomena is necessary for predicting the strength and viscosity of materials composed of polymer layers [2,3]. The phenomenon of polymer-polymer interfacial slip has been previously examined through both experiment and theory.

In the realm of experiment, interfacial slip between polymer layers has been found to reduce the apparent viscosity of layered polymer materials [4–9]. In some cases the low viscosity at polymer-polymer interfaces has been exploited to reduce friction during polymer product extrusion by coating extruder surfaces with a second polymer substance [10]. Experimental work has also demonstrated that the presence of slip between polymer layers reduces the adhesion between the layers [11–14], and it has been argued that the reduced adhesion between layers is the result of slip-induced disentanglement of the interfacial polymers. Some experiments have suggested that interfacial slip plays a role in the stability of polymer blends of the droplet/bulk

variety [15, 16]. During the last decade experiments done by the Macosko group at the University of Minnesota, and by others, have studied in detail the phenomenon of polymer-polymer interfacial slip, including determining the relationship between interfacial stress and slip velocity [17–23]. Some of these experiments have produced data indicating that the interfacial stress / slip velocity relationship undergoes qualitative changes at specific values of the applied stress.

In the realm of theory, an early model for interfacial slip and interfacial viscosity was constructed by Furukawa [24]. Detailed theoretical predictions regarding the scaling behavior of the interfacial stress/slip velocity relationship for polymer-polymer interfaces were initially made by de Gennes, Brochard-Wyart, and coworkers [25–27]. The work by de Gennes and co-workers is the most comprehensive previous theoretical treatment of interfacial slip at an entangled interface between polymer melts. Predictions for slip behavior at an unentangled (Rouse-like [28]) interface between entangled melts were made by Goveas and Fredrickson [29], as well as phenomenological predictions for entangled interfaces. Theoretical and simulation studies of slip at an interface between melts of short polymers (too short to be significantly entangled in the melt bulk; below the Rouse limit) were performed by Barsky and Robbins [30, 31]. Dai and coworkers have examined the mechanisms of polymer-polymer friction through molecular dynamics simulation [32]. A self-consistent field theory for slip between unentangled polymer blends was developed by Lo and coworkers [33].

Of the previous theoretical studies, this work is most similar to the examination performed de Gennes and co-workers [25–27], in that this study considers slip at a significantly entangled polymer-polymer interface. However, the theory developed in this work includes the physical mechanism of polymer retraction, which is a mechanism de Gennes rejects [34]. Consequently the theory here presented uses very different physical reasoning.

1.3 Objectives and Outline

In this work a study is made of stress induced slip at entangled planar polymer-polymer interfaces through a combination of analytic theory and simulation. The goal of this study is to better understand the relationship between stress and slip at a polymer-polymer interface, and to make predictions regarding this relationship. The stress/slip predictions are compared to recently gathered experimental data.

The remainder of this work is divided into seven chapters. Chapter 2 provides a review of the concepts of polymer physics which are relevant to the study of polymer-polymer interfacial slip. In Chapter 3 an analytic theory of interfacial slip is developed, and this theory is used to make predictions for the interfacial slip velocity as a function of interfacial stress for a polymer-polymer interface. Chapters 4, 5, and 6 present a developed computer simulation of a simplified model of interfacial slip, and describe the results: In Chapter 4 the basic simulation algorithm and model employing a slip-link description of polymer entanglement is presented. In Chapter 5 an extension of the simulation to incorporate a self-consistent field description of a polymer-polymer interface is described. Chapter 6 explains the simulation of interfacial slip, and presents the simulation results for the stress / slip velocity relationship. Chapter 7 compares the predictions of the theory and simulation with current experimental data. Chapter 8 summarizes the findings and states the conclusions.

Chapter 2

A Brief History of Relevant Polymer Physics Concepts

The purpose of this chapter is to give a brief history of the concepts of polymer physics related to melt behavior and interfacial slip. This chapter highlights some of the important relevant ideas and their development.

2.1 Basic Polymer Models

Polymers consist of repeating chemical units, and polymers of significant length are flexible. Some basic models treat polymers as random walks of freely jointed linear segments of fixed length (the straight segments are often referred to as "monomers"). Such simple models can accurately describe polymer end-to-end distance distributions and stretching force properties for long polymers in melt or in non-selective solvent. These models predict the average polymer end-to-end distance to be proportional to Nb^2, where b is a length parameter known as the monomer length, and N is a dimensionless measure of the polymer arc-length (the number of monomers in the polymer arc). When comparing the predictions of such models to experimental data

it is often the scaling that is most significant, as a precise values of N and b may not be unique due to the polymer configuration being self-similar. The addition of stiffness criteria to such models, or bond angle constraints, can help to describe polymers that are not perfectly flexible.

In the 1950's some polymer models were developed in which polymers were treated as a series of beads of specified mass connected by Hookean springs. Such a model developed by Rouse in 1951 [28] helped to explain the diffusion properties and relaxation times of polymers in dilute solution. In Rouse's model the polymer mass and frictional drag are associated exclusively with the beads, while the springs connecting the beads are massless and do not contribute to drag. His model did not consider topological interactions between polymers. In the Rouse model the fundamental polymer relaxation time is known as the Rouse time and is, roughly speaking, the time taken for the polymer center of mass to diffuse a distance of the average polymer spatial extension in three dimensional space. After the polymer center of mass has diffused a distance of the polymer spatial extension the polymer has randomized its configuration with the polymer beads in new positions, consequently it has relaxed from or "forgotten" any previous deformations or strains it had experienced. The total polymer drag is proportional to the number of beads in the polymer, which is proportional to the total polymer arc-length N. Through the Einstein diffusion relation [35] this results in a polymer diffusion constant $D = \mathrm{k_B}T/(N\xi)$, where T is the absolute temperature, and ξ is a drag constant. Consequently the Rouse model center of mass diffusion obeys $\langle \Delta \vec{r}^2 \rangle = 6\frac{\mathrm{k_B}T}{N\xi}t$. The equilibrium polymer spatial extension in the Rouse model obeys random walk statistics and is proportional to Nb^2. Altogether, this results in the Rouse relaxation time t_R:

$$t_R \sim \frac{N^2 \xi b^2}{\mathrm{k_B}T} \tag{2.1}$$

Here and throughout this work $\sim$ indicates equality to within an order of magnitude. The Rouse time is the fundamental relaxation time of unentangled linear polymers, and has found some good agreement with experiment in the dilute regime [36]. The Rouse time is proportional to the square of the polymer arc-length, and this relaxation time scaling is considered characteristic for unentangled linear polymers.

Polymer subsections short enough to be individually unentangled are often thought to explore their configuration space in the subsection Rouse time $\sim N_s^2 \xi b^2/(\mathrm{k_B}T)$, where N_s is the subsection arc-length. Consequently, even long entangled polymers may contain subsections that partially equilibrate (or equilibrate relative to other subsections) in a timescale comparable to the subsection Rouse time.

The addition of excluded volume effects to a bead-spring model by Zimm in 1956 [37] helped to better explain the dependence of viscosity on polymer length for dilute polymer solutions. Bead-spring polymer models helped to shed light on the behavior of polymers in dilute solution, but the behavior of polymers in melt was not well understood until the development of the concept of reptation.

2.2 Reptation

Probably the most important concept to have been developed in the physics of entangled polymer melts is the concept of reptation, which was introduced by de Gennes in 1971 [1]. Reptation is the diffusion of a polymer along its own length. When located in a melt, topological interactions with other polymers prevent polymer diffusion perpendicular to the polymer length, but diffusion along its own length is possible. Thus the polymer is confined to an approximately one-dimensional space, and must diffuse along this dimension a distance of its own length in order to vacate its constraints and lose the "memory" of its previous configuration. The time it takes to do this is

the fundamental relaxation time of strongly entangled polymers, and is known as the reptation time.

An illustration of a polymer confined in a tube-like space is shown below.

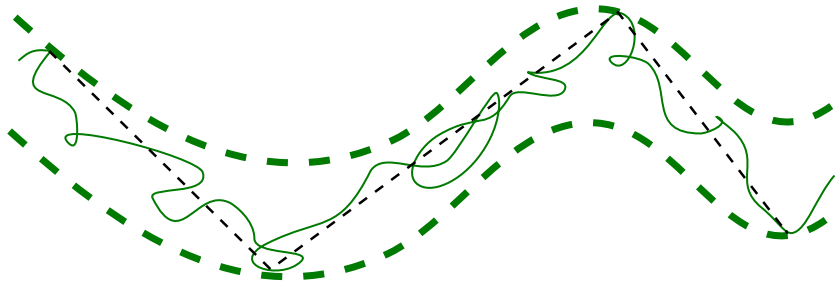

Figure 2.1: An illustration of a polymer topologically confined in a tube-like space. The confining tube is an abstraction; the tube walls represent other polymers. Places of close topological interaction are sometimes referred to as "entanglement" points. The straight dotted lines in the diagram are connecting entanglement points; the average length of these lines is known as the "entanglement distance" or "tube diameter", and is denoted as a. The average sum of all the dotted line lengths is known as the "primitive path length" or "tube length", and is denoted as L.

In the illustration shown in Figure 2.1 a polymer is pictured as confined in a tube-like space. The confining tube is an abstraction which represents neighboring polymers; polymers are unable to pass through each other and, consequently, any given polymer is topologically confined in the space between its polymer neighbors. In some places a polymer will have close interactions with neighboring polymers, and in Figure 2.1 these are represented as the places where the polymer comes into contact with the tube. Such places of close interaction are often idealized as point-like entities known as "entanglements". In the figure the entanglement points are connected by straight dotted lines, and the average value of the length of one such line is known as the "entanglement distance" or "tube diameter", and shall by denoted in this work as a. The average sum of all the lengths of the straight dotted lines connecting entanglement points is known as the "primitive path length", or just

the "tube length", and is denoted as L. The distances between the entanglements fluctuate, and a and L are average value quantities that tend to be most useful when constructing scaling arguments.

Within the space of the confining tube a polymer will undergo diffusion that will be mostly one dimensional and directed along the tube contour. The center of mass diffusion of the polymer along the tube will obey the one dimensional diffusion equation:

$$\langle \Delta s^2 \rangle = 2\frac{\mathrm{k_B}T}{\zeta L}t \tag{2.2}$$

Here Δs is the polymer center of mass displacement along the tube length, and the factor $\mathrm{k_B}T/(\zeta L)$ is the polymer diffusion coefficient. The form of the diffusion coefficient arises from the Einstein diffusion relation [35], taking the total friction to be proportional to the total polymer length (or to the total primitive path length L since this is proportional to the total polymer length). ζ is a drag friction coefficient conjugate to primitive path length, T is the absolute temperature, and $\mathrm{k_B}$ is Boltzmann's constant.

It was argued by de Gennes [38] that the relaxation time for an entangled polymer is the time it takes for the polymer to diffuse along its own length (reptate) a distance on the order of the total primitive path length $\sim L$ so that the confining tube in which it resides is completely new. This time is known as the reptation time t_{rep}. Using the diffusion relation in Equation 2.2 the reptation time is found to be:

$$t_{rep} \sim \frac{L^3\zeta}{\mathrm{k_B}T} \tag{2.3}$$

This is the characteristic relaxation time for an entangled polymer, and consequently is also the characteristic relaxation time for a polymer melt composed of entangled (long) polymers. The specific prefactor for the reptation time depends on the par-

ticular model being used to make predictions, or on the details of the polymer melt being studied. The reptation time prediction that the relaxation time will scale as L^3 has been approximately verified in experiment, though experiments often indicate the exponent is slightly more than 3, often approximately 3.4 [39, 40]. There is evidence that for extremely long polymers pure reptation relaxation scaling will be found with $t_{rep} \propto L^3$ [40, 41], but the discussion is ongoing.

When studying the phenomenon of slip at an interface between two polymer melts the characteristic relaxation time of the melts plays a role in determining the interfacial stress / slip velocity relationship. For this reason it is necessary to understand the reptation mechanism of polymer melt relaxation when constructing physical models for slip at an entangled interface between polymer melts.

The reptation picture predicts that polymer relaxation times will be proportional to the cube of the polymer length, while the Rouse polymer model predicts that unentangled polymer relaxation times will be proportional to the square of the polymer length; both of these predictions have received experimental support within the relevant regimes [36].

2.3 Tube Models

Following the development of the concept of reptation more specific tube models of polymer entanglement were developed and used to quantitatively predict specific properties of polymer melts, such as stress responses and relaxation times. These models incorporated reptation by allowing polymer diffusion along the lengths of confining tubes which were described in mathematically specific ways. The first and most influential tube model was developed by Doi and Edwards [36]. A portion of the mathematical structure of the Doi-Edwards model is used in Chapter 3 of this

work, and a further outline of the Doi-Edwards model is given in Appendix A.

Many tube models employ a physical prediction that the stress in a polymer following a deformation is in a sense stored in the polymer tube constraints, and as a polymer diffuses out of the tube that existed at the time of deformation this stored stress is lost. In simpler tube treatments the polymer stress decay can be taken as simply proportional to the rate of total fractional loss of the tube that existed at the time of deformation. In more complex treatments the stress contribution of individual tube segments can be considered [36].

The mathematical tube models based on the reptation idea were used to calculate many physical melt quantities such as melt viscosity and stress response to different types of deformations, giving results that were sometimes in good agreement with experiment [36].

2.4 Additional Effects

After the initial development of polymer tube models based on reptation, such models were extended to include additional effects such as contour length fluctuations [40]. Inclusion of contour length fluctuations in some models produced reptation times scaling approximately as $L^{3.4}$ as found in experiment [41]. This has lent support to the view that reptation is the primary relaxation mechanism of entangled polymer melts, with deviations from reptation predictions being due to smaller physical effects such as contour length fluctuations.

In early tube theories creation and destruction of tube segments occurred only at the polymer ends. However, all polymers in melt are experiencing reptation and entanglements in central polymer arc regions can be created and destroyed by the motions of the surrounding polymers. This phenomenon is collectively known as

constraint release, and some polymer tube theories attempt to take it into account [42, 43]. The influence of constraint release is thought to be greater on melts of relatively short polymers with few entanglements, where the loss of of few central entanglements could more significantly affect diffusive motion. Branched and star polymers are also thought to be significantly affected by constraint release [42]. Melts of long linear polymers with many entanglements are thought to be less affected as their final relaxation will remain governed by the reptation process [42].

When an entangled polymer melt undergoes a deformation, such as a shear step, the melt stress increases and then decreases as the polymer chains relax via the reptation process. However, upon further analysis it was found that the deformation itself can induce another relaxation process known as convective constraint release [44–47]. When a deformation stretches a polymer tube the polymer can spring back, or retract, thereby vacating sections of the tube near the polymer ends, and releasing some entanglements with other polymers. This process is known as convective constraint release, and it increases the rate of stress relaxation in polymer melts under deformation. Including convective constraint release in polymer tube models has resulted in predictions that are in better agreement with experiment. For example, the Doi-Edwards tube model predicts that polymer melts undergoing a continuous shear deformation will exhibit a stress maximum in the stress vs. shear rate data. Such a maximum is not found in experiment, and including convective constraint release in the predictive tube model alters the prediction so that such a maximum does not occur [44–46].

Extending polymer models with the additional effects of contour length fluctuations, constraint release, and convective constraint release, allows for models that are in better agreement with experiment in certain cases. Including such effects increases the model complexity, and may or may not be necessary depending on the precise

physical behavior being studied.

2.5 Polymer-Polymer Interfaces

Some polymer species are non-mixing, or have repulsive free energy interactions upon contact. Such polymer mixtures may separate into regions of pure species types, and such separations can have distinctly patterned geometries. Theoretical analysis of polymer-polymer energy interactions has produced better understanding of such separation geometries, and of polymer-polymer interfaces in general.

Early consideration of polymer-polymer mixing was made by Huggins and Flory [48–50]. In their work they consider the energy and entropy costs of polymer mixing, and derive physically motivated expressions for these quantities. In their work they express the free energy cost for contact between different species polymers (or polymer and solvent) as proportional to an interaction parameter χ. One form of the free energy expression gives the contact free energy penalty as $\Delta N_A \mathrm{k_B} T \chi \phi_B$, where ΔN_A is an amount of species A polymer arc-length, and ϕ_B is local volume fraction of species B polymer. In essence χ represents the degree of repulsion between the polymer species, and larger χ leads to more strongly separated species regions (the interfacial "thickness" of a polymer-polymer interface scales as $\chi^{-1/2}$). This manner of polymer interface description is further examined in Chapter 5 of this work where it is used to describe a planar interface between immiscible polymer melts.

The theoretical description of polymer melt interfaces was further advanced by the work of others, notably the work of Helfand and Tagami [51, 52]. Methods of numerically calculating self-consistent solutions for the free energy equations of polymer melt interfaces were developed, which have been successful in describing self assembling polymer-polymer interfaces (particularly for block copolymers) [53–60].

Such self-consistent calculation of a chemical potential field describing a polymer-polymer interface is used in Chapter 5 in which a planar polymer-polymer interface is simulated.

2.6 Polymer-Polymer Interfacial Slip

In this work it is proposed to study the relationship between interfacial stress and slip at an entangled planar interface between immiscible polymer melts. The only previous theoretical work on this topic (slip at interfaces between melts of long and entangled polymers) was performed by de Gennes, Brochard-Wyart, and collaborators [25–27]. Experiments on the topic of polymer-polymer interfacial slip have been recently performed by the Macosko group in the department of Chemical Engineering and Materials Science at the University of Minnesota [11, 17–19, 61]. An outline of the previous theoretical and experimental work on interfacial slip between entangled polymer melts is given below.

2.6.1 Theoretical Work

The only previous theoretical work on slip between entangled polymer melts was done by de Gennes and collaborators [25–27]. de Gennes et al. make predictions for the behavior of the interfacial stress as a function of slip velocity, but the language and argument they use is in some places difficult to interpret. I have not been able to interpret the meanings of all of their statements, and their arguments are presented here with some direct quotes (from [25, 26]) when the precise meaning of their statements is uncertain. de Gennes et al. predict that for low interfacial slip velocities the interfacial stress depends linearly on the interfacial slip velocity like a viscous fluid stress "measured at the scale" of the interfacial thickness, and predict

the interfacial viscosity $\eta_I = \eta_1(w/b)^2$, with η_1 being the in-melt monomer viscosity, w the interfacial thickness, and b the monomer length.

de Gennes et al. predict that at a critical interfacial slip velocity V^*, which they give as the entanglement distance divided by the reptation time (a/t_{rep}), the interface will begin to disentangle, leading to a stress plateau in this slip velocity regime. Their argument states that at this slip velocity the tension in an entangled polymer will be $k_B T/a$, which will cause it to disentangle (their reason for picking this precise value is unclear to us). They then predict that a disentangled interfacial polymer will go through a sort of repeated entangling / disentangling process which will cause the interfacial stress to be constant over a range of slip velocities greater than V^*. They state that if an interfacial polymer disentangles "we would lose the entanglement effect, and the force would reduce to a Rouse force". With the reduced force the polymer is not so stretched in the slip direction "thus the chain expands", which leads to the formation of new entanglements. Thus interfacial polymers are considered "marginally stable" over a range of slip velocities above V^*, leading to an interfacial stress plateau in this slip velocity regime. It is clear that de Gennes does not believe the process is related to polymer retraction (convective constraint release), which he clearly rejects [34]. Finally, de Gennes et al. predict that at a large enough slip velocity $V_2 = Z^2 V^*$ (Z is the equilibrium number of bulk entanglements per polymer), all interfacial entanglements will have been destroyed and Rouse-like interfacial rubbing friction will be the dominant mechanism of interfacial stress, causing the interfacial stress to depend linearly on the interfacial slip velocity.

The reasoning behind the disentanglement mechanism that de Gennes et al. propose is non-classical and rather obscure, and seems to have its origin in de Gennes' paper "Molten Polymers in Strong Flows: A Nonclassical Proposal", MRS Bulletin, January, 1991 [34]. In this paper de Gennes rejects the concept of strain induced

retraction of polymer ends, and instead proposes his own "non-classical" mechanism of strain induced polymer disentanglement, based on the concept of an induced tube velocity. Despite his mechanism involving a different physical picture, de Gennes uses his non-retraction mechanism to derive some quantities (such as the viscosity of an entangled polymer melt, Equation 7 in [34]) which are then found to have the same value as when derived via the classical retraction mechanism. The polymer physics community has remained convinced of the retraction mechanism, and has not followed de Gennes in his non-classical proposal. However, de Gennes' conclusions based on his non-classical mechanism are often identical or similar to those derived via classical retraction, which can make it difficult to interpret some of de Gennes' arguments.

de Gennes et al. predict that during polymer-polymer interfacial slip, for slip velocities above $V^* = a/t_{rep}$, the interfacial polymers will begin to disentangle, which will then cause them to expand, which will lead to re-entanglement, causing interfacial polymers to be in a continual semi-entangled state, resulting in interfacial stress being constant over a range of slip velocities above V^*. Though their disentanglement mechanism is non-classical, the concept of an expansion of polymer chains due to reduced flow tension is more straightforward, and is discussed by Brochard-Wyart (one of de Gennes' co-authors) in other works [62, 63]. Before working on the topic of slip between polymer melts de Gennes et al. did work analyzing the slip between a polymer melt and a grafted solid (a solid surface onto which polymer chains were bound) [64–66]. Their work on the topic of slip at a grafted surface appears to have influenced their treatment of polymer-polymer interfacial slip; de Gennes et al. often parameterize their equations in the same way as for the grafted slip case (for instance, treating the number of interfacial polymers per area as a constant parameter), though this might not necessarily be the best way to approach the polymer-polymer slip system.

In this work predictions are derived for the relationship between interfacial stress and slip velocity, and a comparison is made to de Gennes previous treatment. The method of analysis used includes (and depends on) the physical effect of polymer retraction, which de Gennes rejects, making this approach significantly different.

A theoretical and simulation analysis of slip at an unentangled interface between polymer melts was made by Barsky and Robbins [30, 31]. The analysis in this work considers an entangled interface, and is thus physically different from the situation Barsky and Robbins consider. However, the treatment of interfacial stress due to Rouse-like rubbing friction in Chapter 3 is equivalent to their analysis of this aspect. Further theoretical analyses of unentangled interfaces have been made by a handful of other groups with similar predictions [29, 33].

2.6.2 Experimental Work

Detailed experimental analysis of stress induced polymer-polymer slip has presented technical difficulty, and the most significant results have been obtained by the Macosko group at the University of Minnesota, and collaborators [11, 15, 17–19, 61]. The Macosko group has performed some delicate interfacial slip experiments in which blocks of polymer composed of alternating layers of polymer melt species were exposed to a shearing force. By observing the deformation of the total melt block the slip between the layers could be calculated. In the data obtained the relationship between the interfacial stress and slip velocity tended to obey power-law scaling, and sometimes seemed to exhibit a plateau over a range of slip velocities [17, 19] in qualitative agreement with the prediction of de Gennes. Examining this behavior is part of the motivation for this further theoretical study. The theoretical analysis leads to slip/stress predictions which are compared with experimental data at the end of this work. In other experiments by this group polymer-polymer interfacial slip was found

to reduce the adhesion between polymer layers, possibly indicating a slip-induced loss of interfacial entanglements [11, 61]. Some slip experiments have been performed by other researchers as well, though the focus of many of the other experiments is on verifying that interfacial slip does occur, rather than in determining a stress / slip velocity relationship [20, 22].

Experimental observance of a viscosity reduction in polymer melt blends was one of the first experimental indications of polymer-polymer interfacial slip [4–9]. Because a number of plastics products and processing operations involve layers of different species polymer melts [2, 3, 10], gaining a better theoretical understanding of polymer-polymer interfacial slip is likely to be practically useful.

2.7 Polymer Simulation: Slip-link Models

Many computational methods and models have been used to simulate polymer behavior. In the simulation portion of this work a particular entangled polymer model known as a slip-link model is used. A slip-link polymer model treats entanglements between polymers as sliding rings known as slip-links. The use of slip-links to represent entanglements between polymers has been a convenient abstraction that has allowed for more tractable theoretical and simulation analysis of entangled polymers. In some cases, such as in the simulation model presented in Chapter 4, using slip-links to represent entanglements between polymers makes it possible to simulate each polymer independently. Physically realistic detailed balance rules governing the creation and destruction of slip-links are necessary for such a simulation to give realistic physical results. Such models have been successful in producing polymer melt responses consistent with experiment, and this simulation strategy allows for easy simulation parallelization.

The idea of using slip-links to represent polymer entanglements gained traction in the last two decades of the twentieth century. Treating an entanglement between polymers as a connecting ring is a convenient abstraction for theoretical analysis, and a number of papers analyzed the theoretical properties of slip-link polymer models [67–118]. A significant number of further analyses have compared the physical predictions of slip-link models to experimental data (primarily melt stress response), sometimes with very good result [119–138]. Slip-link models have been examined in reviews of polymer simulation methods in which different simulation strategies are compared [139–144].

In particular the slip-links simulations used in this work were inspired by those of Schieber et al. [145–157] in which the polymer is modeled as a Gaussian filament, with the simulation being coarse grained to only resolve entanglement positions. The types of simulation presented in Chapters 4, and 5 follow a similar strategy.

Chapter 3

An Analytic Model of Polymer-Polymer Interfacial Slip

3.1 Introduction

In this chapter a specific theoretical model of polymer-polymer interfacial slip is constructed. The model is used to make physical predictions regarding the relationship between the interfacial stress and the interfacial slip velocity at a planar boundary between immiscible polymer melts. The model predicts several parameter regimes in which the interfacial stress / slip velocity relationship is qualitatively different, and makes quantitative predictions for stress induced interfacial slip velocity values.

The purpose of this chapter is to derive the relationship between interfacial stress and slip velocity for a planar interface between immiscible polymer melts composed of long (highly entangled in melt) polymers using a specific model for the microstructure of entanglement. Because an entangled interface is being considered, the analysis in this chapter is most similar to the previous treatment by de Gennes and co-workers [25–27], but the model here presented relies on the concept of polymer retraction, a concept de Gennes rejected [34]. Consequently this treatment of interfacial slip uses

very different physical reasoning.

In this chapter the analysis is divided into three major sections: Section 3.2 presents an outline of the physical model used as well as scaling arguments for different physical quantities. In section 3.3 an analysis is made of the population dynamics of interfacial entanglements during slip. In section 3.4 more detailed mathematical predictions for the interfacial stress behavior are made using the entanglement population dynamics information obtained in section 3.3.

3.2 Overview

To begin, the axioms and assumptions of the model are clearly specified:

In order to construct a model of polymer-polymer interfacial slip it is first hypothesized that the stress across the interface between two polymer melts is transmitted primarily by entanglements between the different polymer species, where an "entanglement" is a localized topological interaction. For simplicity and for relevance to recent experiments [17, 19, 20] a planar interface between two immiscible polymer species is considered. The polymer solutions are treated as being in densely packed "melt" form with no solvent present. Melts are considered to be incompressible and of fixed polymer density. Individual polymers are modeled as inextensible flexible non-self-interacting threads. Polymers interact topologically with other polymers; they cannot pass through each other.

To study how interfacial entanglements between the polymer species transmit stress across the polymer-polymer interface entanglements are modeled as "slip-links." Here a slip-link is a frictionless ring-like constraint in space through which a polymer is able to slide. Though an entangled polymer is constrained to pass through a slip-link the polymer is not required to pass through it in a particular direction; i.e. slip-links

do not constrain polymer tangent vectors. Slip-link descriptions of entanglement have been previously studied and used in simulation, with some success in reproducing realistic rheological response [153, 154]. In this analysis slip-links are considered to be created and destroyed only at polymer ends when polymer end motion forms or releases a new entanglement (this model does not include constraint release [142]). Polymers are considered to be of fixed length (contour length fluctuations are not included).

In this model entanglements are treated as slip-links, and interfacial entanglements (between the two polymer species) are given special consideration. The process of slip is modeled as a constant velocity translation of the interfacial entanglements (interfacial slip-links) in a direction parallel to the planar interface. The case of a sharply defined interface is considered (the interfacial width is much less than the average polymer spatial extension because the melts are highly immiscible), and the slip deformation is approximated as a "perfect" slip between melts. By perfect slip it is meant that all of the polymers of one species are in translation at constant slip velocity V with respect to the polymers of the other species. Variations in slip velocity within the interfacial region are ignored in this approximation; also ignored is the stress resulting from strain deformations of the two melts. It is assumed that the slip deformations studied do not significantly alter the interfacial density profiles. The model presented studies the behavior of interfacial stress as induced by perfect slip along a planar interface between highly immiscible entangled polymer melts.

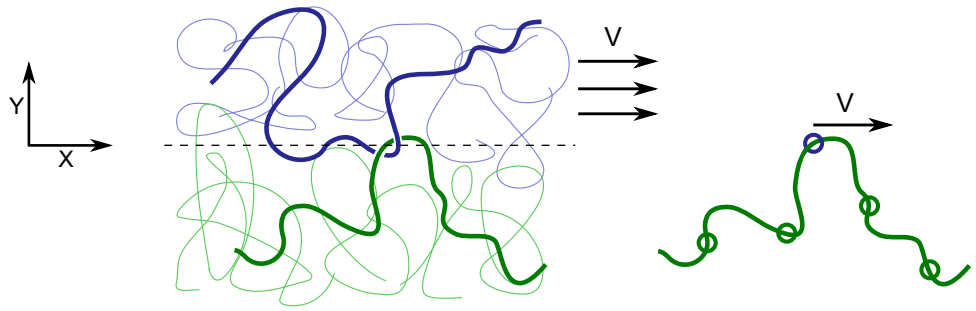

Figure 3.1: Illustration of the interfacial slip model for a polymer entangled at the polymer-polymer interface. Entanglements are treated as ring-like constraints called slip-links. The constant velocity translation ("slip") of one melt relative to the other is modeled by having interfacial entanglements translate at a constant velocity V. The polymer is subject to drag friction proportional to its length and proportional to its velocity relative to the melt it resides in.

The slip velocity V is directed parallel to the planar interface. In Figure 3.1 the slip velocity is directed in the positive x-coordinate direction, while the y-coordinate is perpendicular to the planar interface. The coordinate conventions in Figure 3.1 are used throughout this entire work.

The polymer melts considered are composed of "long" polymers in the sense that the average length available for single polymer transverse motion without encountering another is much less than the total polymer length. That is, the polymers in the melt bulk are highly entangled, and their final configurational relaxation is governed by diffusion along their length known as reptation [1]. For simplicity, the polymer species meeting at the interface are considered symmetric; the melts have the same polymer density and are composed of polymers that have the same length, average distance between entanglements, monomer volumes, and friction interactions. The entire system is at the same absolute temperature T.

In this model it is convenient to communicate in terms of polymer primitive path length L, corresponding to the average length of the "tube" confining a given polymer.

In the usual monomer polymer description a polymer in-melt is described as a random walk of N straight monomer segments of length b. Each polymer resides in a tube-like cage composed of the other surrounding polymers. The polymer experiences some close topological interactions with the surrounding polymers; each such interaction shall be idealized as a localized entity known as an entanglement, which in this model is represented by a slip-link. Denoting the average number of monomers between entanglements as N_e, and the average spatial distance between entanglements as a (equal to $\sqrt{N_e}b$), the polymer primitive path can be defined as the path of N/N_e straight segments of average length a connecting the points of entanglement. The total length of the primitive path is given by $L = (N/N_e)\, a$. It should be emphasized that the spatial and arc-length distances between entanglements fluctuate, and the primitive path idea is most applicable as a scaling argument concept. The total polymer primitive path length is related to the total number of monomers through $L = Nb^2/a$. Though primitive path length is a concept that primarily applies to entire polymers, or polymer sections long enough to be significantly entangled, in this work a section with ΔN monomers will be referred to as having primitive path s given by $s = \Delta N b^2/a = \Delta N b/\sqrt{N_e}$. The polymer must diffuse a distance on the order of the total primitive path length L along its own length before it has vacated all of its entanglement constraints and its configuration is independent of its previous configuration.

Each polymer experiences viscous frictional drag, and the drag force on a polymer section is proportional to the number of monomers in the section, or equivalently to the section primitive path length, and to the velocity of the section relative to the melt background. The drag force magnitude f on a polymer section with ΔN monomers, primitive path length s, and velocity magnitude v relative to the melt

background is given by:

$$f = \xi \Delta N v = \zeta s v \tag{3.1}$$

ξ is the drag coefficient conjugate to number of monomers and ζ is the drag coefficient conjugate to primitive path length. ξ and ζ have different units and are related by $\zeta = \xi a/b^2$ so that $\xi \Delta N = \zeta s$. The drag force on each polymer section is directed opposite to the section velocity. Throughout this work all polymer sections are treated as being at force equilibrium; it is assumed that reaching force equilibrium with frictional drag happens extremely quickly relative to entanglement processes, and the short time scales at which accelerations exist are not resolved.

For tractability, and because a sharp interface between highly immiscible polymers is being considered, at first the approximation is made that even polymers located near the interface will have low interfacial penetration and will have at most one interfacial entanglement. This assumption is later relaxed in section 3.3.2, and the possibility of single polymers with multiple interfacial entanglements is discussed.

During slip if an interfacial entanglement is located asymmetrically along a polymer arc-length the shorter of the two polymer strands connected to the slip-link will have less path-length to drag through the viscous medium and will experience a lower total drag force. Consequently the viscous drag forces on the polymer will cause the shorter of the polymer strands to retract toward the slip-link. This drag induced retraction will tend to pull the nearest polymer end toward and through the slip-link. This means that during slip retractive polymer motion will increase the rate of interfacial disentanglement; this retractive motion will also cause surviving interfacial entanglements to tend to be located nearer to the polymer ends.

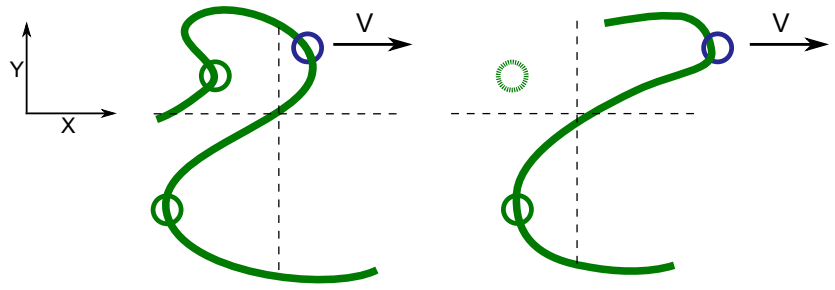

Figure 3.2: Illustration of slip induced retraction. The two graphics are separated by a time interval. The shorter of the two polymer strands experiences less total friction under slip, and moves more quickly toward the moving slip-link than the longer strand. The shorter polymer strand retracts toward the moving slip-link and becomes shorter still. That is, slip motion causes the interfacial (blue) slip-link to be located nearer to the polymer end in terms of arc-length. If the polymer retracts completely through a slip-link that slip-link is lost. Axes are shown for perspective.

Relaxation of a given polymer takes place via diffusion through the polymer's one dimensional tube-like surroundings. A polymer is spatially confined by its polymer neighbors and to re-equilibrate must diffuse along its own length a distance on the order of its own primitive path length L so that its surroundings and spatial configuration are completely new. For a polymer with frictional drag proportional to path-length (as is the case in this model) the polymer diffusion coefficient for motion along its primitive path is $D = \frac{\mathrm{k_B}T}{L\zeta}$ (via the Einstein diffusion relation [35]). The time needed for full polymer re-equilibration via diffusion is known as the reptation time. Using $\langle \Delta s^2 \rangle = 2D\Delta t$ the reptation time is given up to a scaling constant by:

$$t_{rep} \sim \frac{L^3 \zeta}{\mathrm{k_B}T} \tag{3.2}$$

Using this model of interfacial polymer interaction it is possible to make predictions regarding the dependence of interfacial stress on slip velocity. Throughout this work "interfacial stress" refers to the single component of the stress tensor σ_{yx} corresponding to the transmitted interfacial force parallel to the slip direction per area of the interface. In the following subsections the physical mechanisms affecting interfacial stress are examined, and an outline of the qualitative behavior of interfacial stress at different slip velocities is presented.

3.2.1 Interfacial Stress

During slip the polymer strands connected to an interfacial entanglement partially align in the slip direction. The slip direction stress transmitted across the interface by interfacial entanglements σ^e_{yx} will be given by the sum of the slip direction polymer tension forces on all interfacial entanglements divided by the interfacial area. There will additionally be a stress contribution σ^R_{yx} from Rouse-like [28] rubbing friction between the layers that is linear with respect to slip velocity. The total interfacial stress σ_{yx} will be given by:

$$\sigma_{yx} = \sigma^e_{yx} + \sigma^R_{yx} \tag{3.3}$$

The stress transmitted by interfacial entanglements may be expressed as:

$$\sigma^e_{yx} = \frac{1}{A_y} \sum_{i=1}^{2Z_e} \vec{\tau}_i \cdot \hat{x} \tag{3.4}$$

Here $\vec{\tau}_i$ is the tension force acting on an interfacial entanglement from the i^{th} polymer strand. Z_e is the total number of interfacial entanglements, and the sum goes to $2Z_e$ because each interfacial entanglement is connected to two polymer strands (one on each side). A_y is the total interfacial area.

σ^e_{yx} can be altered by any of three processes: change in the total number of inter-

facial entanglements Z_e, change in the magnitude of the interfacial polymer strand tensions $|\tau_i|$, or change in the alignment of the interfacial polymer strands in the slip ($\hat{x}$) direction.

If retractive polymer motion during interfacial slip causes a polymer end to pull out of an interfacial entanglement the entanglement is lost. New entanglements are formed at polymer ends by the motion of the polymer chain into new regions, but if entanglement destruction happens more quickly than entanglement creation via polymer diffusion the result will be a decrease in the average number of interfacial entanglements. For slip-induced interfacial entanglement destruction to occur the entanglement must slip a distance on the order of the polymer primitive path length L. If entanglement destruction takes place on a timescale less than the polymer re-equilibration time (the reptation time t_{rep}) the average number of interfacial entanglements will be significantly reduced. This defines a slip velocity scale V^{**} for the onset of significant entanglement destruction:

$$V^{**} \sim \frac{L}{t_{rep}} \sim \frac{\mathrm{k_B}T}{L^2\zeta} \tag{3.5}$$

When the interfacial slip velocity exceeds V^{**} the concentration of interfacial entanglements will be significantly reduced below the equilibrium value.

During slip a polymer attached to a moving interfacial entanglement will be pulled through the viscous melt background, and the frictional drag forces acting on it will cause an increase in the average polymer tension. An upper bound estimate of the scale of this tension increase may be obtained by considering the case where an interfacial entanglement is located exactly in the polymer center. When the slipping interfacial entanglement is located exactly in the polymer center the drag forces on the strands on either side of the entanglement are balanced and no retraction will occur (until fluctuations cause the interfacial entanglement to be displaced from the

polymer center). While the interfacial entanglement is centrally located the entire polymer will be pulled along at the entanglement slip velocity V. The absence of retraction means that the polymer is experiencing the maximum possible total drag force because retractive motion lessens the total drag experienced by a polymer.

With the entire polymer translating at slip velocity V the total drag experienced by a polymer strand (length $L/2$), and consequently the increase in tension at the position of the slip-link $\Delta\tau$, will be given by:

$$\Delta\tau = \frac{\zeta L V}{2} \tag{3.6}$$

It was previously argued that above slip velocity V^{**} (Equation 3.5) the number of interfacial entanglements between the melts is significantly reduced. If $V^{**} = L/t_{rep}$ is taken as the characteristic slip velocity for the onset of significant slip-induced disentanglement the magnitude of the maximum polymer tension increase at this onset is:

$$\Delta\tau(V^{**}) = \frac{L^2\zeta}{2t_{rep}} \sim \frac{\mathrm{k_B}T}{L} \tag{3.7}$$

The polymer possesses a thermal equilibrium tension τ_0, and if the polymer is treated as a Gaussian filament in a manner like that used in the model of Doi and Edwards [36] this tension is given by:

$$\tau_0 = \frac{3\mathrm{k_B}T}{a} \tag{3.8}$$

This equilibrium tension can be derived if a polymer is considered to be a Gaussian filament fixed average distance between entanglements a, with a stretching force between entanglements $\vec{f} = 3\mathrm{k_B}T\vec{Q}_s/a^2$, where $\vec{Q}_s$ is the end-to-end vector between two entanglements. When at equilibrium at temperature T, the $\vec{Q}_s$ distribution will be Gaussian: $P(\vec{Q}_s) \propto \exp[-3\vec{Q}_s^2/(2a^2)]$. The root-mean-square value of $\vec{Q}_s$ is then

equal to a, and this results in the average force between entanglements at equilibrium (the tension) being equal to $3k_BT/a$.

As can be seen from Equations 3.7 and 3.8 for tightly confined polymers with $a \ll L$ the thermal equilibrium tension will be much greater than the drag induced tension increase at slip velocity V^{**}; that is $\Delta\tau(V^{**}) \ll \tau_0$. In fact the maximum drag induced tension increase only becomes comparable to the equilibrium thermal tension at a slip velocity on the order of $\frac{L}{a}V^{**}$. This argument estimates the upper bound for the drag-induced tension increase, and if a given entanglement is located nearer to a polymer end the tension increase will be smaller. For tightly confined polymers this means that, for the purposes of calculating stress, the polymer strand tensions are well approximated by the thermal tension τ_0 for all slip velocities up to and exceeding the disentanglement characteristic velocity V^{**}. Additionally, for slip velocities significantly above V^{**} the interface is expected to become disentangled as previously discussed, which suggests that drag induced polymer tension increase never significantly contributes to the interfacial stress.

During interfacial slip the polymer strands attached to a translating interfacial entanglement will partially align in the slip direction. As the polymer tension forces acting on an interfacial entanglement become more aligned in the slip direction interfacial stress will increase.

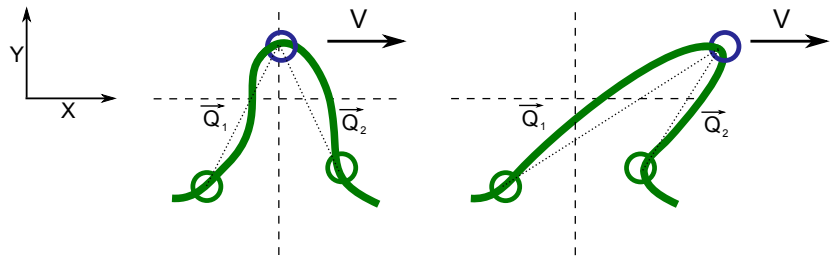

Figure 3.3: Illustration of slip-induced strand alignment. The polymer strands connected to an interfacial entanglement align during interfacial slip. The strand end-to-end vectors between entanglements $\vec{Q}_i$ become more aligned in the slip ($\hat{x}$) direction. Consequently the strand tension forces become more aligned in the slip direction, causing an increase in interfacial stress. The polymers are considered to continue to the left and right beyond what is pictured. Axes are shown for perspective.

If the average equilibrium spatial distance between polymer entanglements is a an interfacial entanglement will need to slip a distance of order a for the connected strands to become significantly aligned in the direction of slip. If this alignment happens in a timescale shorter than the polymer relaxation time (t_{rep}) the existing interfacial entanglements will be connected to polymer strands which are nearly aligned in the direction of slip. This defines a slip velocity scale V^* for the onset of interfacial strand alignment:

$$V^* \sim \frac{a}{t_{rep}} \sim \frac{a\mathrm{k_B}T}{L^3\zeta} \tag{3.9}$$

This velocity scale argument predicts that when the interfacial slip velocity exceeds V^* the existing polymer strands connected to interfacial entanglements will be

nearly aligned in the direction of slip. The characteristic velocity of alignment is smaller than the characteristic velocity of entanglement destruction by the ratio of the entanglement distance to the polymer primitive path length; $V^* = (a/L)V^{**}$.

For tightly confined polymers ($a \ll L$) the characteristic slip velocities V^* and V^{**} will be widely separated. At intermediate slip velocities $V^* < V < V^{**}$ the polymer strands will be nearly aligned in the slip direction but the number of interfacial entanglements will not be significantly changed from the zero slip value. This allows the definition of a characteristic stress scale σ^*_{yx} for this intermediate velocity regime:

$$\sigma^*_{yx} = 2\rho_0 \frac{3\mathrm{k_B}T}{a} \tag{3.10}$$

ρ_0 is the zero slip equilibrium number of interfacial entanglements per area, and $3\mathrm{k_B}T/a$ is the strand thermal equilibrium tension (polymer tension is little altered at this slip velocity scale, as previously discussed). A factor of 2 is present in Equation 3.10 because each interfacial entanglement is attached to two interfacial strands. σ^*_{yx} is the interfacial stress corresponding to the presence of the zero slip equilibrium number of interfacial entanglements each connected to two polymer strands with equilibrium tension completely aligned in the slip direction.

The value of ρ_0 may be estimated in terms of the interfacial width w and monomer volume ν. If the interfacial region has width w the number of monomers per area of the interface may be estimated as w/ν. If the average number of monomers between entanglements in the bulk is N_e the probability of a monomer possessing an entanglement of any type can be approximated as N_e^{-1}. If the same entanglement probability applies in the interface, the probability of a monomer in the interface forming an interfacial (inter-species) entanglement may be approximated as $(2N_e)^{-1}$, where here the factor of two arises from the approximation that interfacial monomers are on average in contact half with monomers of the same species and half with monomers

of the other species. Altogether then ρ_0 is estimated as:

$$\rho_0 \sim \frac{w}{2N_e\nu} = \frac{w}{2\nu}\frac{b^2}{a^2} \tag{3.11}$$

Finally, if the Flory-Huggins description of polymer interaction [48, 49] is used the interfacial width w may be expressed as:

$$w = \frac{b}{\sqrt{6\chi}} \tag{3.12}$$

Here χ is the Flory-Huggins polymer-polymer interaction strength parameter [48, 49].

At the interface between two slipping polymer melts the polymers belonging to each melt will experience Rouse-like rubbing friction from their interaction with the opposite melt polymers which are in relative motion. A number of polymers from each melt will penetrate some amount into the other, and will experience a drag force from the surrounding polymers which are in relative translation at the slip velocity V. If the friction coefficient for interactions between the polymer species is the same as the friction coefficient for polymer self-interactions an order of magnitude estimate for the Rouse-like stress contribution σ_{yx}^R may be made:

$$\sigma_{yx}^R \sim \frac{w}{\nu}\xi V \tag{3.13}$$

Here ξ is the monomer friction coefficient, V is the interfacial slip velocity, w is the width of the interface, and ν is the monomer volume (considered the same for both polymer species). w/ν is the number of monomers per area present in the interfacial region. It is assumed that the interfacial monomer density profiles are not significantly altered by the slip deformation. An expression for σ_{yx}^R which includes numerical prefactors can be obtained through a method employing the Helfand-Tagami analytic description of concentration profiles at an interface between immiscible melts of long

polymers [51, 52], as discussed in section 3.4.3.

The stress due to Rouse-like rubbing friction increases linearly with slip velocity, and the stress transmitted via interfacial entanglements decreases for slip velocities above V^{**} as interfacial entanglements are destroyed. Consequently, at some slip velocity the stress due to rubbing friction will become the dominant component of the interfacial stress. The behavior of the stress due to Rouse-like rubbing friction is independent of the total polymer length (assuming $L \gg w$). As a measure of when the Rouse-like stress becomes dominant consider the slip velocity V_R where the Rouse-like stress σ_{yx}^R is equal to the characteristic stress due to polymer strand alignment σ_{yx}^* (Equation 3.10). V_R is found to be:

$$V_R \sim \frac{\nu}{w}\frac{\rho_0}{\xi}\frac{\mathrm{k_B}T}{a} \tag{3.14}$$

Using the estimate for ρ_0 in Equation 3.11 this becomes:

$$V_R \sim \frac{1}{N_e\xi}\frac{\mathrm{k_B}T}{a} = \frac{\mathrm{k_B}T}{a^2\zeta} \tag{3.15}$$

This may be compared to the characteristic slip velocity for the onset of interfacial entanglement destruction V^{**} (Equation 3.5):

$$V_R \sim \left(\frac{L}{a}\right)^2 V^{**} \tag{3.16}$$

This result indicates that for strongly confined polymers ($a \ll L$) the Rouse-like friction will only become dominant at slip velocities much larger than V^{**} where all interfacial entanglements have been destroyed.

3.2.2 Interfacial Stress Slip Velocity Regimes

The physical mechanisms altering interfacial stress during slip become significant at different slip velocity scales. The characteristic slip velocity at which the polymer strands become aligned in the slip direction is $V^* \sim a/t_{rep}$. For tightly confined polymers at slip velocities below V^* interfacial stress increase is primarily due to strand alignment. At slip velocities above V^* the polymer strands are primarily aligned in the slip direction, and strand alignment is therefore incapable of increasing stress further.

The characteristic slip velocity of interfacial entanglement destruction is $V^{**} \sim L/t_{rep}$. Above V^{**} slip-induced polymer retraction significantly reduces the number of interfacial entanglements. For tightly confined polymers, with $a \ll L$, a wide slip velocity regime between V^* and V^{**} will exist in which the interfacial polymer strands are nearly aligned, but the number of interfacial entanglements is not significantly reduced from the equilibrium value. In this intermediate regime an interfacial stress plateau is expected, with a plateau stress σ^*_{yx} (Equation 3.10).

An estimate was made for the maximum possible slip induced polymer tension increase. It was found that the interfacial slip velocity at which the maximum possible slip induced tension increase becomes comparable to the equilibrium tension is on the order of $\frac{L}{a}V^{**}$. This upper bound estimate for the tension increase ignores tension decreasing retraction effects. For this reason the polymer tension is well approximated by its equilibrium thermal tension value $\tau_0 = 3\mathrm{k_B}T/a$ for slip velocities even significantly exceeding the interfacial disentanglement slip velocity V^{**}. Because the polymer-polymer interface is expected to be nearly disentangled at slip velocities much greater than V^{**} it is expected that polymer tension increase never significantly contributes to the interfacial stress.

The slip velocity at which Rouse-like rubbing friction becomes the dominant in-

terfacial stress mechanism is expected to be much larger than V^{**}. The Rouse-like friction contribution to interfacial stress will only become comparable to the plateau stress σ^*_{yx} at a slip velocity $V_R \sim (L/a)^2 V^{**}$. As a consequence a stress decrease is expected to occur in the slip velocity regime $V^{**} < V < V_R$, where the interface will have become significantly disentangled but the Rouse-like stress will not yet have become dominant. Below is a schematic of the expected behavior of interfacial stress as a function of slip velocity.

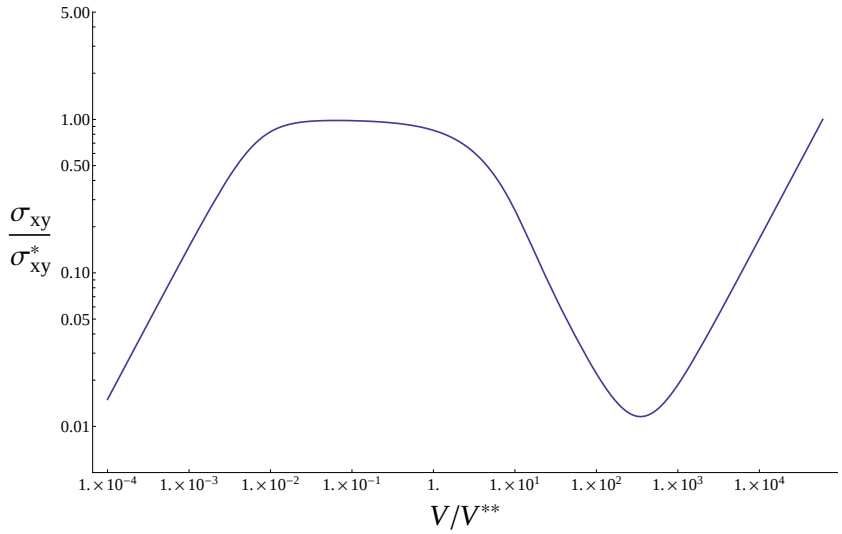

Figure 3.4: Schematic of the qualitative behavior of interfacial stress σ_{yx} as a function of slip velocity V. Stress is in units of the characteristic alignment stress $\sigma^*_{yx} = 6\rho_0 \frac{k_B T}{a}$. Slip velocity is in units of the characteristic slip velocity for onset of slip-link destruction $V^{**} \sim L/t_{rep}$. A stress plateau region exists at slip velocities above the characteristic slip velocity of interfacial strand alignment $V^* \sim a/t_{rep}$ but below the characteristic disentanglement slip velocity V^{**}. $t_{rep} \sim \frac{L^3 \zeta}{k_B T}$. At some slip velocity V_R stress due to Rouse-like rubbing friction becomes dominant. The plot is for a system with $L = 100a$ giving $V^* = 0.01V^{**}$ and $V_R = 60000V^{**}$. Both axes are in logarithmic scale.

3.3 Slip-link Population Dynamics

In this section an analysis of the population dynamics of interfacial entanglements during slip is made. First the case where each polymer near the interface has at most one interfacial entanglement is considered. Then the more general case of multiple interfacial entanglements per polymer is considered, including how the presence of multiple interfacial entanglements affects the interfacial slip-stress relationship.

3.3.1 Single Interfacial Slip-link Per Chain

As slip proceeds the polymer strands on either side of an interfacial slip-link experience an increase in tension due to the drag force opposing motion. This tension increase due to drag (though expected to be small compared to the polymer thermal equilibrium tension τ_0 as discussed in section 3.2.1) is the mechanical effect that drives slip-induced polymer retraction. Considering the polymer strands connected to an interfacial entanglement such as in Figure 3.3, the tensions τ in the polymer strands meeting at the position of the interfacial slip-link can be approximated for slip velocities above V^*. For slip velocities $V > V^*$ the strands are primarily aligned in the direction of slip, and the strand tensions are given by:

$$\tau_1 = \zeta s(V - \dot{s}) + \tau_0 \tag{3.17}$$

$$\tau_2 = \zeta(L - s)(V + \dot{s}) + \tau_0 \tag{3.18}$$

Here s is the primitive path position of the interfacial slip-link relative to one polymer end (the primitive path length between the slip-link and that polymer end). L is the total polymer primitive path length, and V is the slip velocity (the translational velocity of the interfacial slip-link). τ_0 is the thermal equilibrium tension present in

each strand (Equation 3.8), which is on average uniform over the entire polymer and identical for each strand.

The mechanical requirement that the strand tensions immediate to the sides of the interfacial slip-link be equal ($\tau_1 = \tau_2$, the slip-link is considered frictionless in this model) results in an equation for polymer path length retraction through the slip-link:

$$\dot{s} = V\left(\frac{2s}{L} - 1\right) \tag{3.19}$$

The meaning of this equation can be briefly summarized in the statement that the shorter of the polymer strands experiences less total viscous drag friction during slip, and consequently has its path length reduced as it is pulled through the slip-link. This "retraction" of the shorter strand under slip can also be intuitively understood as a tendency of the interfacial entanglement to pull off the nearest polymer end.

In addition to slip-induced retractive motion the polymer also experiences one dimensional diffusion, known as reptation, within its tube like surroundings. In the absence of slip the diffusive motion of the polymer would eventually distribute the interfacial entanglements evenly along the polymer path length (the approximation is made that entanglement position along the chain contour is independent of entanglement position in space when in equilibrium without slip).

The combined effects of reptation and retraction can be expressed in a Fokker-Planck equation for the density of slip-links along the polymer primitive path length.

$$\frac{\partial\tilde{\rho}(V,s,t)}{\partial t} = -\frac{\partial}{\partial s}\left(\dot{s}\tilde{\rho}(V,s,t)\right) + \frac{\mathrm{k_B}T}{L\zeta}\frac{\partial^2\tilde{\rho}(V,s,t)}{\partial s^2} \tag{3.20}$$

Here $\tilde{\rho}(V,s,t)$ is the slip-link area density per primitive path length. The first term on the right in Equation 3.20 represents the effect of retraction by which the shorter polymer strand is pulled toward the interfacial entanglement during slip. The second

term on the right represents the effect of the one-dimensional diffusive motion of the polymer in its tube-like surroundings. At zero slip velocity $\tilde{\rho}$ satisfies the condition $\int_0^L \tilde{\rho}\, dL = \rho_0$, with ρ_0 being the zero-slip equilibrium interfacial entanglement area density. Including the expression for $\dot{s}$ (Equation 3.19) the expression becomes:

$$\frac{\partial \tilde{\rho}(V,s,t)}{\partial t} = V\left(1-\frac{2s}{L}\right)\frac{\partial \tilde{\rho}(V,s,t)}{\partial s} - \frac{2V}{L}\tilde{\rho}(V,s,t) + \frac{k_B T}{L\zeta}\frac{\partial^2 \tilde{\rho}(V,s,t)}{\partial s^2} \tag{3.21}$$

It is possible to find steady state solutions to Equation 3.21 after imposition of boundary conditions. To determine what boundary conditions are appropriate the modeling choice is made that interfacial entanglements are created only at polymer ends by the motion of a polymer end into new regions (the motion of a polymer end into new regions provides the possibility of new entanglement with other polymers). Similarly slip-link destruction takes place only at polymer ends. If the creation and destruction processes are sufficiently fast the slip-link density at the polymer ends will be constant. The dangling polymer ends are considered to explore their surrounding space very quickly (via Rouse-like motion) compared to the time it takes for the configuration of the central entangled portions of the polymer to significantly change. For this reason very fast slip-link creation and destruction at the polymer ends is assumed, and thus the boundary conditions for Equation 3.21 are that the slip-link probability density at the polymer ends is constant, and equal to its equilibrium value when no slip is present. That is, the boundary conditions are:

$$\tilde{\rho}(0,0,t) = \tilde{\rho}(0,L,t) = \frac{\rho_0}{L} \tag{3.22}$$

Finding the steady state ($\frac{\partial \tilde{\rho}}{\partial t} = 0$) solutions for 3.21 using the conditions in 3.22 gives:

$$\tilde{\rho}(V,s) = \frac{\rho_0}{L}\exp\left[-\frac{V}{V^{**}}\frac{s}{L}\left(1-\frac{s}{L}\right)\right] \tag{3.23}$$

V^{**} is the solution characteristic velocity found to have the value:

$$V^{**} = \frac{k_B T}{L^2 \zeta} \tag{3.24}$$

Plotting this for different values of the slip velocity V yields:

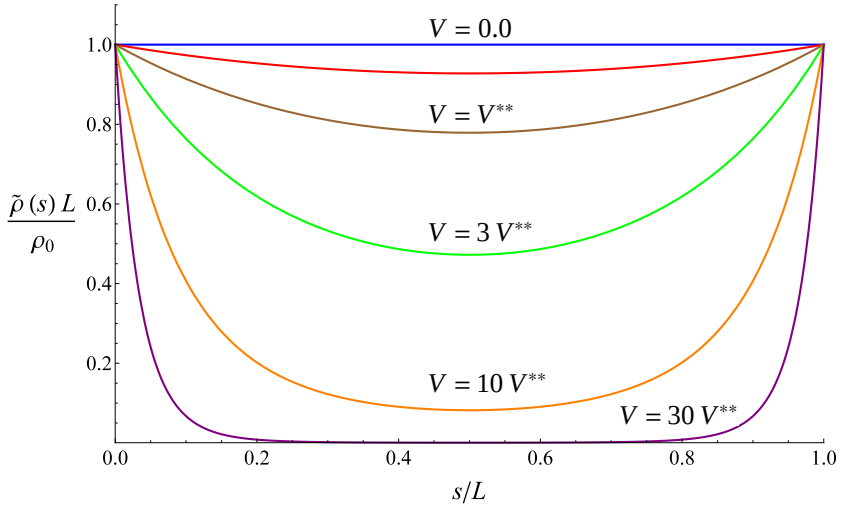

Figure 3.5: Interfacial entanglement density $\tilde{\rho}$ (interfacial entanglements per interfacial area per primitive path length) as a function of primitive path position s. L is the total polymer primitive path length and ρ_0/L is the zero slip equilibrium density. Steady state solutions at different slip velocities V are shown. For higher slip velocities slip-links become more clustered near the polymer ends. The slip-link density is fixed at the polymer ends due to fast creation and destruction in those regions. The model has characteristic disentanglement slip velocity $V^{**} = \frac{k_B T}{L^2 \zeta}$. Slip velocities indicated near the associated curve.

As slip velocity increases it can be seen that the interfacial entanglements become more closely clustered around the polymer ends. Because slip-links are created at the polymer ends they reach the center of the polymer only through reptative polymer diffusion. For larger slip velocities the process of polymer retraction becomes stronger, which tends to pull the nearest polymer end toward the slip-link more quickly and increase the rate of slip-link disentanglement. Consequently, for higher slip velocities the retractive polymer motion, and the decreased average time of slip-link existence,

tend to decrease the likelihood that polymer reptation will enable an interfacial entanglement to reach the middle of the polymer.

The steady state interfacial entanglement area density for slip velocity V can be obtained through integration, $\rho(V) = \int_0^L \tilde{\rho}(V,s)\,ds$. As can be seen from Figure 3.5 when slip velocity V is increased the area under the $\tilde{\rho}(V,s)$ curve is decreased, resulting in a decreased number of interfacial entanglements. Integrating to find $\rho(V)$ yields:

$$\rho(V) = \int_0^L \frac{\rho_0}{L} \exp\left[-\frac{V}{V^{**}}\frac{s}{L}\left(1-\frac{s}{L}\right)\right] ds \tag{3.25}$$

$$\rho(V) = \rho_0 \Phi\left(V/V^{**}\right) \qquad \Phi(x) \equiv \frac{2}{\sqrt{x}} e^{-x/4} \int_0^{x/4} e^{y^2} dy \tag{3.26}$$

$\rho(V)$ is found to be a monotonically decreasing function of slip velocity V, which indicates that for higher slip velocities fewer interfacial entanglements are present. The function $\Phi(x)$, defined above, expresses information concerning the fraction of remaining interfacial entanglements. The functional form of $\Phi(x)$ is similar to a function known as the Dawson Function. The fraction of interfacial entanglements remaining at slip velocity V will be given by $\rho(V)/\rho_0 = \Phi(V/V^{**})$.

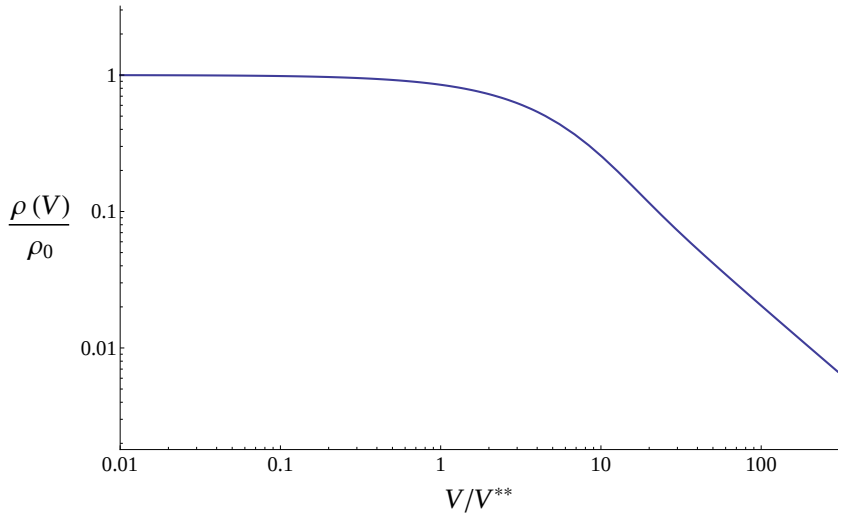

Figure 3.6: Fraction of surviving interfacial entanglements (slip-links) vs. slip velocity V. Both axes are in logarithmic scale. Slip velocity is in units of the characteristic disentanglement slip velocity $V^{**} = \frac{k_B T}{L^2 \zeta}$.

As can be seen in Figure 3.6 the fraction of interfacial entanglements remaining begins to drop significantly when the slip velocity V is above the characteristic velocity V^{**}. Thus V^{**} can be thought of as the characteristic slip velocity for the onset of interfacial entanglement destruction. When the slip velocity is above V^{**} the two polymer melts have become significantly disentangled from one another. From an intuitive point of view V^{**} is approximately equal to the total polymer length divided by the reptation time; thus if an interfacial entanglement has slipped a distance equal to the total polymer length in a time less than or equal to a reptation time (the total polymer relaxation time) then it is likely that a polymer end has retracted through (released) the entanglement without the entanglement having been repositioned along the polymer or replaced by another through diffusive polymer motion.

In the highest slip velocity asymptotic limit ($V \gg V^{**}$) the fraction of interfacial

entanglements remaining is given by:

$$\frac{\rho(V)}{\rho_0} = \frac{2V^{**}}{V} \tag{3.27}$$

3.3.2 Multiple Interfacial Slip-links Per Interfacial Polymer

In this section the possible effects of having more than one interfacial entanglement per interfacially entangled polymer are considered. It is found that the presence of multiple moving interfacial slip-links has the effect of increasing the polymer retraction velocity, and the retraction velocities induced by each interfacial slip-link are additive. This has the effect of decreasing the interfacial slip-link lifetimes. The magnitude of multiple interfacial slip-link effects is found to depend on the dimensionless quantity $\lambda_I \equiv (w_I/a)\sqrt{L/a}$, where w_I is the interfacial width. When $\lambda_I \ll 1$ the influence of multiple interfacial slip-links per polymer becomes negligible. The full analysis is given below.

Consider the case where each interfacially entangled polymer has $M+1$ interfacial entanglements (for simplicity all interfacially entangled polymers are here considered to have the same number of entanglements in equilibrium, and variations in M are ignored). This situation can be solved in the same manner as the single interfacial slip-link situation, making mechanical arguments for tension and retraction for any chosen number of interfacial slip-links translating at slip velocity V. However, upon analysis a simpler method is found to be valid; the primitive path length retraction velocity $\dot{s}$ across a given interfacial slip-link is found to be altered by the presence of other interfacial slip-links in an additive manner. That is, the retraction velocity across any given interfacial slip-link is given by:

$$\dot{s} = V\left(\frac{2s}{L} - 1\right) - 2V\sum_{i}^{M_+}\left(1 - \frac{s_i}{L}\right) + 2V\sum_{j}^{M_-}\frac{s_j}{L} \tag{3.28}$$

Here the first term in Equation 3.28 represents the self-induced retraction, caused by the motion of the interfacial entanglement being considered. The second term represents the retraction induced by the M_+ interfacial slip-links residing between the considered interfacial slip-link at location s and the higher primitive path coordinate polymer end (at $s = L$). The third term represents the retraction induced by the M_- slip-links residing between $s = 0$ and the considered interfacial slip-link at s. A positive $\dot{s}$ represents primitive path length retraction across the slip-link toward the lower primitive path coordinate direction (the sign of $\dot{s}$ is the sign of the slip-link velocity in the space of path length). All interfacial slip-links are treated as translating through space at slip velocity V. Equation 3.28 also assumes that between each interfacial slip-link there is at least one non-interfacial (like-species) entanglement.

To evaluate the total $\dot{s}$ at one interfacial slip-link first the probability of other interfacial slip-links being located at various positions along the polymer primitive path must be determined. To this end, consider the conditional probability path density $P(s'|s)$ that given one interfacial slip-link at path position s another interfacial slip-link will be found an infinitesimal path distance from path position s'. Self-consistent field theory indicates that an interface between highly immiscible polymer melts acts as a reflecting boundary [158, 159]. Considering such a highly immiscible reflecting interface makes it possible to determine an analytic expression for $P(s'|s)$. The probability density for the end-to-end distance of a polymer with one end at the interface is consequently a half Gaussian function (a "reflected" Gaussian). Using this, it can be argued that an approximate expression for $P(s'|s)$ in equilibrium without slip is given by:

$$P(s'|s)ds' = \left[w_I \left(\frac{6}{\pi |s' - s| a} \right)^{1/2} \right] \left(\frac{ds'}{a} \right) \tag{3.29}$$

The portion of Equation 3.29 in brackets is the probability that a Gaussian thread

with primitive path point s located at a reflecting interfacial plane will also have path point s' located within spatial width w_I of the interfacial plane (the return probability). w_I is a measure of the interfacial width which is taken as defined by Equation 3.29; w_I can be thought of as the distance from the interfacial plane in which interfacial entanglements are formed. a^{-1} is taken as the probability density of a section of primitive path length forming any type of entanglement (in this analysis this is equivalent to taking N_e^{-1} as the probability of a monomer forming any type of entanglement). Consequently ds'/a is the probability that small primitive path length ds' forms an entanglement in the region being considered. Using Equations 3.28 and 3.29 an approximate expression for the average retraction at an interfacial slip-link at primitive path position s on a polymer with multiple interfacial slip-links may be obtained:

$$\dot{s}(s) = V\left(\frac{2s}{L} - 1\right) + 2V\int_0^L P(s'|s)\left[\Theta(s-s')\frac{s'}{L} - \Theta(s'-s)\left(1 - \frac{s'}{L}\right)\right]ds' \quad (3.30)$$

Here the Θ represents the Heaviside step function, and the quantity in brackets can be thought of as a sort of Green function for the retraction velocity induced by other interfacial slip-links. Using Equation 3.29 and performing the integration yields:

$$\dot{s}(s) = V\left(\frac{2s}{L} - 1\right) + \frac{8}{3}\sqrt{\frac{6}{\pi}}V\frac{w_I}{a}\sqrt{\frac{L}{a}}\left(\left(\frac{s}{L}\right)^{3/2} - \left(1 - \frac{s}{L}\right)^{3/2}\right) \quad (3.31)$$

Equations 3.30 and 3.31 are approximate due to the approximate reflecting boundary treatment for strongly segregated interface, which results in the zero slip equilibrium return probability $P(s'|s)$ in Equation 3.29. Consequently these expressions are expected to be most accurate for a strongly immiscible interface, and for low slip velocities before retraction has significantly altered the slip-link path position profile.

The impact that multiple interfacial entanglements per chain have on the average

path retraction velocity is governed by the dimensionless quantity:

$$\lambda_I = \frac{w_I}{a}\sqrt{\frac{L}{a}} \tag{3.32}$$

It can be seen that as this quantity approaches zero the retraction velocity in Equation 3.31 approaches the retraction velocity in the single interfacial entanglement per polymer case given in Equation 3.19. w_I is a measure of the interfacial width expected to be proportional to the common definition of interfacial width (Equation 3.12); w_I is taken to be probabilistically defined by Equation 3.29. For narrow enough interfaces the single interfacial slip-link per polymer treatment becomes valid.

It is possible to express λ_I in terms of the number of interfacial slip-links on an interfacially entangled polymer. Choosing a polymer with at least one interfacial entanglement M is taken to be the total number of other interfacial entanglements when at equilibrium without slip (the total number of interfacial entanglements on the polymer is $(M+1)$). Using the conditional probability in Equation 3.29 this can be expressed as:

$$M = \frac{1}{L}\int_0^L ds \int_0^L ds' P(s'|s) \tag{3.33}$$

This expression makes the approximation that the primitive path location probability density for a single interfacial slip-link chosen at random is uniform along the polymer primitive path. Performing the integration gives:

$$M = \frac{8}{3}\sqrt{\frac{6}{\pi}}\frac{w_I}{a}\sqrt{\frac{L}{a}} = \frac{8}{3}\sqrt{\frac{6}{\pi}}\lambda_I \tag{3.34}$$

With this relation between λ_I and the number of other interfacial entanglements at equilibrium M Equation 3.31 can be re-expressed as:

$$\dot{s}(s) = V\left(\frac{2s}{L} - 1\right) + MV\left(\left(\frac{s}{L}\right)^{3/2} - \left(1 - \frac{s}{L}\right)^{3/2}\right) \tag{3.35}$$

A plot of the path retraction velocity $\dot{s}$ as a function of s for different values of M is shown below:

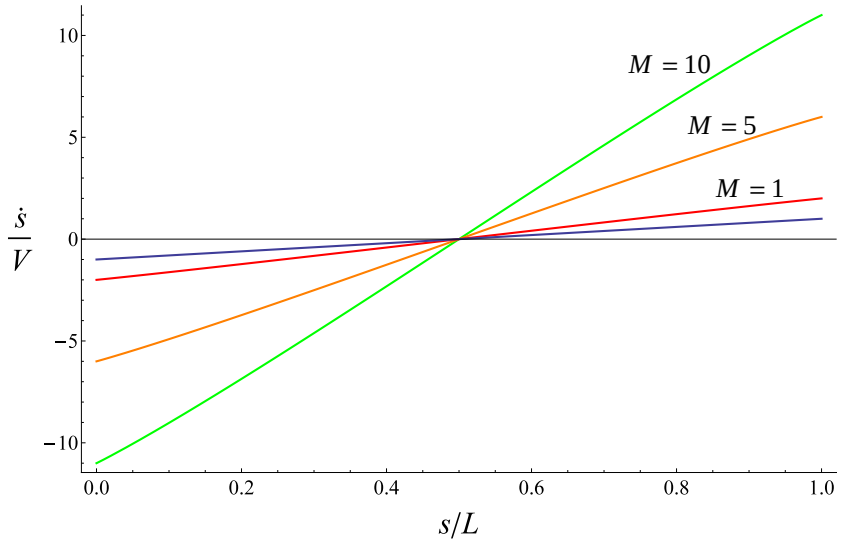

Figure 3.7: Relative primitive path retraction velocity $\dot{s}/V$ vs. interfacial slip-link primitive path position s/L. The retraction velocity $\dot{s}$ is in ratio to the interfacial slip velocity V. Solutions are shown for cases where multiple interfacial entanglements per polymer are present. Total interfacial entanglements per polymer $Z = M + 1$. More interfacial entanglements on a polymer induces a larger retraction velocity. Solutions shown for $M = 0$, $M = 1$, $M = 5$, and $M = 10$. Solutions take the interfacial slip velocity V to be positive. The line corresponding to $M = 0$ (the single interfacial slip-link case) is strictly linear, while the other lines corresponding to greater values of M have some curvature.

As can be seen in Figure 3.7 the presence of multiple interfacial entanglements increases the primitive path retraction velocity through an interfacial slip-link, driving the interfacial slip-links more quickly to the polymer ends. The effect of multiple interfacial entanglements during slip on interfacial slip-link primitive path position is consequently very similar to the effect of increased slip velocity V. The expression for $\dot{s}$ in Equation 3.35 can be used with Equation 3.20 to solve for the interfacial slip-link primitive path position probability density for some fixed V. The resulting probability density shows that the slip-links become located closer to the polymer

ends for higher values of M, similar to the way slip-links are shown to be located closer to the polymer ends at higher slip velocities in Figure 3.5.

Increased retraction due to the presence of multiple interfacial entanglements on a given polymer is fundamentally different from increased retraction due to higher slip velocity in that when interfacial slip-links are destroyed M is reduced, which lessens the impact of multiple interfacial slip-links at slip velocities high enough to begin interfacial disentanglement. For this reason, in the high slip velocity regime $V \sim V^{**}$ it is expected that the single interfacial slip-link treatment will be valid as interfacial polymers will have become disentangled or have only one surviving interfacial entanglement.

An examination of the onset of interfacial disentanglement may be performed using Equations 3.20 and 3.35 to solve for the fraction of interfacial entanglements remaining $\rho(V)/\rho_0$ in the same manner as in the single interfacial slip-link case. Such a method is a low slip velocity approximation as Equation 3.35 is obtained using the zero slip equilibrium return probability given in Equation 3.29. However, this method is used to gain a sense of the interfacial disentanglement onset in the case of multiple interfacial slip-links per interfacial polymer. Numerically solving for the fraction of interfacial entanglements remaining as a function of slip velocity V for different values of M yields the result shown in Figure 3.8.

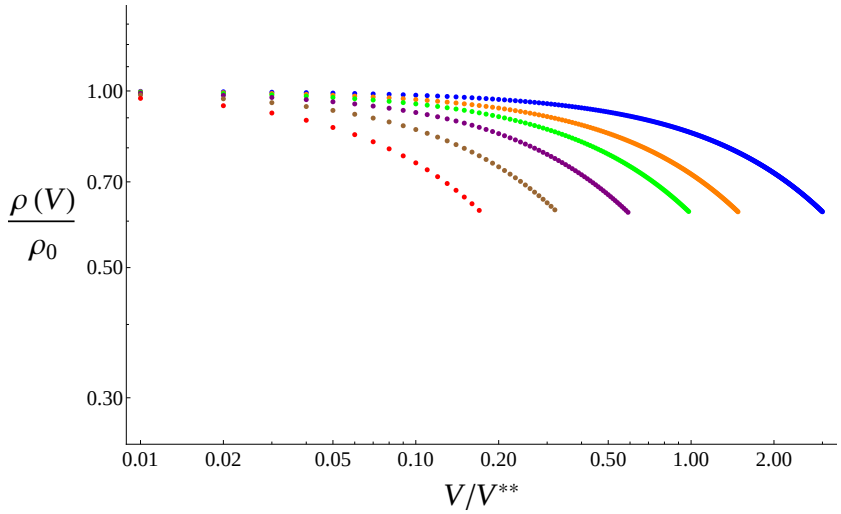

Figure 3.8: Fraction of interfacial entanglements remaining vs. slip velocity. Slip velocity in units of the characteristic velocity of interfacial entanglement destruction $V^{**} = \frac{k_B T}{L^2 \zeta}$ for the single interfacial slip-link per polymer case (Equation 3.24). Both axes are in logarithmic scale. Solutions for different numbers of interfacial entanglements per polymer are shown. More interfacial entanglements per polymer results in entanglement destruction at lower slip velocity. There are $M + 1$ interfacial entanglements per polymer when in equilibrium without slip. Numerical solutions shown for $M = 0$, $M = 1$, $M = 2$, $M = 4$, $M = 8$, and $M = 16$.

It is found that higher M values cause interfacial entanglement destruction to begin at lower slip velocities. Defining a characteristic destruction slip velocity V_M^{**} as the slip velocity giving the same fraction of entanglements remaining as would be present at slip velocity V^{**} in the single interfacial entanglement per polymer a relationship is found:

$$V_M^{**} = \frac{V^{**}}{M+1} \tag{3.36}$$

The velocity for the onset of significant interfacial disentanglement in the case of multiple interfacial slip-links per polymer is thus reduced from the single slip-link case by a factor of the total number of interfacial entanglements per polymer present in equilibrium without slip. However, it should again be restated that as the polymer

loses interfacial entanglements the retraction caused by those slipping entanglements is lost, and in the high slip velocity limit the single interfacial entanglement per entangled polymer regime is expected to be valid.

The presence of multiple interfacial entanglements on a single polymer during slip causes a larger tension increase in the polymer. An upper bound on this tension increase can be obtained. The greatest possible tension increase will occur if the translating interfacial slip-links are located symmetrically along the polymer and clustered near the polymer center (with non-interfacial slip-links between them). This will cause the polymer ends to retract quickly toward the center at velocity $V(M+1)$ (if M is taken as even). If the interfacial slip-links are clustered tightly near the polymer center this will cause the maximum tension increase as nearly all of the polymer arc will be retracting at this velocity relative to the melt background. This will cause the polymer tension increase $\Delta\tau$ to be:

$$\Delta\tau = \zeta(M+1)\frac{L}{2}V \tag{3.37}$$

This upper bound estimate for the maximum polymer tension increase is large than the single interfacial slip-link estimate in Equation 3.6 by a factor of $(M+1)$. This means that the slip velocity at which the tension increase is expected to be comparable to the thermal tension is decreased by a factor of $(M+1)$. However, in the presence of multiple interfacial slip-links per polymer the slip velocity at which interfacial entanglement destruction begins to occur is also increased by a factor of $(M+1)$. Consequently the tension increase at the entanglement destruction velocity is still given by $\Delta\tau(V_M^{**}) \sim \mathrm{k_B}T/L$ (as in Equation 3.7), and is much less than the thermal tension $3\mathrm{k_B}T/a$. As a result the drag induced tension increase is still expected to be much less than the thermal tension at slip velocities up to and exceeding the disentanglement velocity. Because the interface will be nearly disentangled before

the drag induced tension increase becomes comparable to the thermal tension, tension increase is not expected to contribute to interfacial stress even in the multiple interfacial slip-link per polymer regime.

Having multiple interfacial slip-links per polymer is not expected to alter the interfacial stress increase at low slip velocities ($V < V^*$) where the stress increase is due to polymer strand alignment. It is also not expected to affect the Rouse-like rubbing stress. Drag induced tension increase is still expected to remain a negligible contribution to interfacial stress in this case. The presence of multiple interfacial slip-links per polymer is expected to decrease the slip velocity at which interfacial entanglement begins by a factor of the number of interfacial slip-links per interfacially entangled polymer ($M + 1$). However, as the interface becomes disentangled there will be fewer interfacial slip-links per polymer, and in the high slip velocity limit ($V > V^{**}$) the fraction of entanglements remaining is expected to behave as in the single interfacial slip-link per polymer treatment. The possibility of multiple interfacial slip-links per polymer is governed by the dimensionless parameter $\lambda_I = (w_I/a)\sqrt{L/a}$. As λ_I becomes small, such as in the case of a very narrow interface, the system approaches a limit with at most one interfacial entanglement per polymer.

3.4 Interfacial Stress

During the process of interfacial slip the two polymer melts exert forces on one another across the melt interface through their mutual entanglement. Using the slip-link model of interfacial entanglement, and the results from the analysis of slip-link population dynamics during slip in section 3.3, the stress across the interface between the melts can be determined. Throughout this section a narrow interface is assumed such that each interfacial polymer has at most one interfacial entanglement as the treat-

ment in section 3.3.1, though brief comments are made as to how multiple interfacial entanglements per polymer would alter the interfacial stress behavior.

The stress across the interface induced by interfacial slip is the result of a combination of processes. Part of the interfacial stress will be due to forces transmitted by interfacial entanglements σ^e_{yx}, while part of the interfacial stress will be due to Rouse-like rubbing friction between the layers σ^R_{yx}. The general expression for the entanglement interfacial stress σ^e_{yx} was given in Equation 3.4. The entanglement interfacial stress is affected by changes in the alignments of the polymer strands attached to interfacial entanglements, changes in the strand tension magnitudes, and changes in the total number of interfacial entanglements. The Rouse-like rubbing friction is expected to be linear with respect to slip velocity. An expression for the average interfacial stress may be written using an approximation that treats the average degree of interfacial strand alignment as independent of the average strand tension:

$$\langle \sigma_{yx}(V) \rangle = 2\,\rho(V) \langle u_x \rangle \langle \tau \rangle + \alpha_R V \tag{3.38}$$

The first term in Equation 3.38 is the average stress transmitted by interfacial entanglements $\langle \sigma^e_{yx} \rangle$, and the second term is the average stress resulting from Rouse-like friction $\langle \sigma^R_{yx} \rangle$. In the first term $\rho(V)$ is again the steady state number of interfacial entanglements per area at slip velocity V, and $\langle u_x \rangle$ signifies the average component of an interfacial strand end-to-end unit vector in the direction of slip. $\langle \tau \rangle$ is the average tension per polymer strand. Both $\langle u_x \rangle$ and $\langle \tau \rangle$ are also functions of the slip velocity V. Expressing the interfacial stress due to entanglement as a product of the average strand alignment and the average strand tension ignores correlations between the two, and also makes the approximation that all strands align independently and by the same mechanism during slip. A factor of 2 is present in the first term in Equation 3.38 because each interfacial entanglement is connected to two polymer strands.

3.4.1 Interfacial Strand Tension

The average interfacial strand tension $\langle\tau\rangle$ may be evaluated using the steady state slip-link probability distribution along the polymer path length. The strand tension at a slip-link at polymer path position s and translating at slip velocity V can be determined using Equations 3.17 and 3.19:

$$\tau(V,s) = 2\zeta V s\left(1-\frac{s}{L}\right)+\tau_0 \tag{3.39}$$

$\langle\tau\rangle$ can then be found by integrating over the steady state slip-link probability distribution in s, which is equal to $\tilde{\rho}(V,s)/\rho(V)$.

$$\langle\tau\rangle = \int_0^L \tau(V,s)\frac{\tilde{\rho}(V,s)}{\rho(V)}ds \tag{3.40}$$

Using Equations 3.39 and 3.40 the average interfacial strand tension can be rewritten as:

$$\langle\tau\rangle = 2\zeta V\int_0^L s\left(1-\frac{s}{L}\right)\frac{\tilde{\rho}(V,s)}{\rho(V)}\,ds+\tau_0\int_0^L\frac{\tilde{\rho}(V,s)}{\rho(V)}\,ds \tag{3.41}$$

Performing these integrals and simplifying yields:

$$\langle\tau\rangle = \frac{k_B T}{L}\frac{\Psi(V/V^{**})}{\Phi(V/V^{**})}+\frac{3k_B T}{a} \tag{3.42}$$

$$\Psi(V/V^{**}) \equiv \frac{2V}{V^{**}}\int_0^1 \gamma(1-\gamma)\exp\left[-\frac{V}{V^{**}}\gamma(1-\gamma)\right]d\gamma \tag{3.43}$$

The left term in Equation 3.42 is due to drag-induced frictional tension, while the term on the right is the equilibrium thermal tension τ_0. Ψ is a dimensionless function defined in Equation 3.43, while Φ is a dimensionless function equal to the fraction of interfacial entanglements remaining $\rho(V)/\rho_0$, given in Equation 3.26. Equation 3.42

indicates that the average interfacial strand tension may be written as:

$$\langle \tau \rangle = \langle \tau_d \rangle + \tau_0 \qquad\qquad \langle \tau_d \rangle = \frac{k_B T}{L} \frac{\Psi(V/V^{**})}{\Phi(V/V^{**})} \tag{3.44}$$

Here $\langle \tau_d \rangle$ is the average interfacial strand tension due to viscous drag. In the expression for $\langle \tau_d \rangle$ the ratio of dimensionless functions Ψ and Φ can be evaluated numerically to show the behavior of the drag induced strand tension as a function slip velocity:

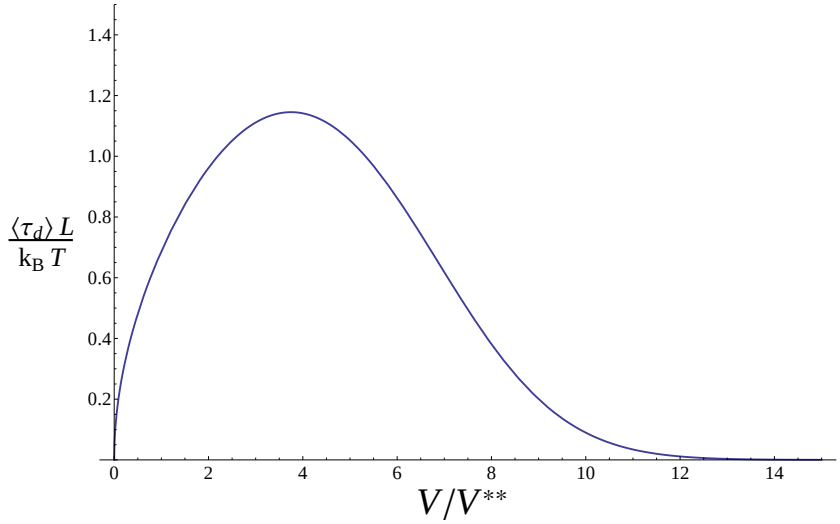

Figure 3.9: $\langle \tau_d \rangle$, the average interfacial polymer strand tension due to viscous drag, vs. slip velocity V. Strand tension is in units of the characteristic force for drag induced tension $k_B T/L$. Slip velocity is in units of the characteristic velocity for onset of slip-link destruction V^{**}. $V^{**} = \frac{k_B T}{L^2 \zeta}$.

From Figure 3.9 it can be seen that the average drag induced interfacial strand tension $\langle \tau_d \rangle$ is never more than approximately $1.2\, k_B T/L$. With this information it can be seen that for systems with the entanglement length much less than the total polymer primitive path length $a \ll L$ the average interfacial strand tension in Equation 3.42 will be dominated by the equilibrium strand tension. In such a regime the second term in Equation 3.42 will be much larger than the first, and the average

interfacial strand tension will be well approximated by the thermal equilibrium strand tension $\langle\tau\rangle \approx \tau_0 = 3\mathrm{k_B}T/a$.

The interfacial strand tension is well approximated by τ_0 for strongly entangled polymers ($a \ll L$), and this allows us to rewrite the average stress transmitted by interfacial entanglements σ^e_{yx} as:

$$\langle\sigma^e_{yx}\rangle \approx 2\rho(V)\langle u_x\rangle\tau_0 \tag{3.45}$$

Equation 3.45 indicates that the stress due to entanglement at a slipping interface between polymer melts of high entanglement is governed by the alignment of the interfacial polymer strands $\langle u_x\rangle$, and the number of interfacial entanglements per area of the interface $\rho(V)$. The average slip direction alignment of polymer strands connected to an interfacial entanglement $\langle u_x\rangle$ is a function of slip velocity; at zero slip velocity the strand orientation vectors will be isotropically distributed in the directions parallel to the interface, and this average will vanish. The value of $\langle u_x\rangle$ will increase with increasing slip velocity as the strands become aligned more quickly compared to the time it takes for them to directionally relax. Equation 3.45 predicts that stress transmitted by interfacial entanglements will result as a competition of the slip direction alignment of polymer strands with approximately thermal equilibrium tension, and the destruction of interfacial entanglements through polymer retraction.

For polymer melts with less pronounced entanglement the full tension expression in Equation 3.42 could be used to calculate the interfacial entanglement stress, resulting in:

$$\left\langle\sigma^e_{yx}(V)\right\rangle = 2\rho_0\langle u_x\rangle\left\{\frac{\mathrm{k_B}T}{L}\Psi(V/V^{**}) + \frac{3\mathrm{k_B}T}{a}\Phi\left(V/V^{**}\right)\right\} \tag{3.46}$$

As can be seen, the stress expression in Equation 3.46 contains two terms, one of order $\mathrm{k_B}T/L$ corresponding to the interfacial stress associated with drag induced

strand tension increase, and one of order $k_B T/a$ associated with the strand thermal equilibrium tension. Each term is multiplied by a previously defined dimensionless function (Ψ and Φ, defined in Equations 3.43 and 3.26). Ψ is at most approximately $1.2\,\Phi$ at any slip velocity. Φ is a measure of the fraction of equilibrium entanglements remaining and is equal to 1 at zero slip velocity, after which it decreases monotonically with increasing slip velocity. For strongly entangled polymers with $a \ll L$ the thermal tension term will dominate and Equation 3.46 will become equivalent to Equation 3.45. However, Equation 3.46 could be used to calculate slip induced interfacial stress including the small contributions due to tension change, though to be valid the polymers should be sufficiently entangled that reptation is the dominant relaxation mechanism.

If multiple interfacial entanglements per polymer were present the analysis of strand tension and interfacial stress would proceed in approximately the same way with the primary difference being that the characteristic slip velocity of polymer retraction induced entanglement destruction would instead be $V_M^{**} = V^{**}/(M+1)$, with $M+1$ being the total number of interfacial entanglements per polymer present at equilibrium without slip. Consequently, in such a case significant interfacial polymer retraction and entanglement destruction would begin at a lower slip velocity. This would tend to more strongly push slip-links toward polymer ends, more quickly reducing the interfacial strand tension and the number of interfacial entanglements, which would tend to decrease interfacial stress. However, as interfacial slip-links were destroyed the extra retraction induced by multiple interfacial slip-links per polymer would lessen. Consequently, though $\rho(V)/\rho_0$ would be expected to begin to decrease at a lower slip velocity, the high slip velocity ($V > V^{**}$) behavior would be expected to be similar to the single slip-link per polymer case.

3.4.2 Interfacial Strand Alignment

During interfacial slip polymer strands entangled with the opposite melt will continually align in the direction of slip. This alignment causes the polymer tension forces in the boundary region to be anisotropically oriented, which results in increased stress at the polymer-polymer boundary. The analysis finds that the degree of interfacial strand alignment is governed by the characteristic interfacial slip velocity $V^* = a/t_{rep}$; when the interfacial slip velocity is greater that V^* the interfacial strands are nearly aligned in the direction of slip, and further interfacial stress increase due to strand alignment is not possible. An analysis of the interfacial stress due to strand alignment is presented below.

In the previous section an expression for the interfacial stress as a function of slip velocity for highly entangled polymer melts was obtained (Equation 3.45). For slip velocities much lower than the characteristic velocity of entanglement destruction V^{**} the number of interfacial entanglements is unchanged from the zero slip equilibrium value. Consequently in the regime $V \ll V^{**}$ the interfacial stress is well approximated by:

$$\langle \sigma_{yx} \rangle \approx 2\rho_0 \frac{3\mathrm{k_B}T}{a} \langle u_x \rangle + \alpha_R V \tag{3.47}$$

For a polymer strand attached to an interfacial entanglement slipping at constant velocity V the strand end-to-end unit vector component in the slip direction is given by:

$$u_x = \frac{\vec{Q} \cdot \hat{x}}{|\vec{Q}|} \qquad\qquad u_x = \frac{Q_{x0} + \Delta t V}{\sqrt{\vec{Q}_0^2 + 2\Delta t V Q_{x0} + (\Delta t V)^2}} \tag{3.48}$$

Here Δt is the time that has elapsed since slip began deforming the polymer strand from its initial state; if slip is ongoing Δt will be the time elapsed since the interfacial

entanglement formed. $\vec{Q}_0$ is the strand end-to-end vector at the time of interfacial entanglement creation.

In order to find the average interfacial strand alignment $\langle u_x \rangle$ as a function of slip velocity, the expression for u_x in Equation 3.48 must be averaged over the values of the initial strand end-to-end vector $\vec{Q}_0$, and over time using the probability that a strand which is created at time t' will survive until time t. Let $P(\vec{Q}_0)$ be the distribution of interfacial strand end-to-end vectors at the time of interfacial entanglement formation, and let $\mu(t-t')dt'$ be the probability that an interfacial entanglement formed in an infinitesimal time region near t' will survive until time t. The expression for the average degree of interfacial strand alignment may be written as:

$$\langle u_x(V) \rangle = \int_{-\infty}^{t} dt' \mu(t-t') \int d\vec{Q}_0 P(\vec{Q}_0) \frac{Q_{x0} + (t-t')V}{\sqrt{\vec{Q}_0^2 + 2(t-t')VQ_{x0} + ((t-t')V)^2}} \tag{3.49}$$

In the case of a strongly segregated interface $P(\vec{Q}_0)$ may be analytically determined. If the strand is modeled as a flexible random walk $P(\vec{Q}_0)$ will be Gaussian in the directions parallel to the planar interface. If the interface is highly segregated (due to a large χ interaction parameter) self-consistent field theory indicates that in the direction perpendicular to the interface the interface will behave as a reflecting boundary [158,159]. For a strongly segregated interface interfacial entanglements will be located very close to the interfacial boundary and $P(\vec{Q}_0)$ can be approximated as a "reflected" Gaussian distribution:

$$P(\vec{Q}_0) = 2\left(\frac{3}{2\pi a^2}\right)^{3/2} \exp\left(-\frac{3\vec{Q}_0^2}{2a^2}\right) \Theta(-Q_{y0}) \tag{3.50}$$

$\Theta(y)$ is the Heaviside step function, and its use here expresses the strongly segregated reflecting boundary condition that prevents interfacial strands from crossing

the interfacial boundary.

For slip velocities much lower than V^{**} slip-induced retractive motion will be small and interfacial entanglement creation and destruction will be controlled by reptative diffusion of the polymer. In this limit the probability that an interfacial entanglement created at time t' will survive until time t can be determined using the Doi-Edwards reptation model ([36], Appendix A), where the interfacial entanglement survival is equated with the survival of an infinitesimal section of the constraining polymer tube. Using the Doi-Edwards reptation model (Appendix A) the interfacial entanglement survival probability $\mu(t-t')dt'$ is given by:

$$\mu(t-t')dt' = \sum_{p;odd} \frac{8}{\pi^2 t_{rep}} \exp\left(-p^2(t-t')^2/t_{rep}\right) dt' \tag{3.51}$$

The analytic expressions for $P(\vec{Q}_0)$ and $\mu(t-t')dt'$ in Equations 3.51 and 3.50 make it possible to numerically evaluate the expression for average interfacial strand alignment $\langle u_x \rangle$ in Equation 3.49. From the approximations used in obtaining these analytic expressions, the result for $\langle u_x \rangle$ will be most accurate for strongly segregated interfaces and slip velocities $V \ll V^{**}$. The solution for the degree of alignment is found to have the characteristic slip velocity:

$$V^* = \frac{a \mathrm{k_B} T}{L^3 \zeta} = \frac{a}{L} V^{**} \tag{3.52}$$

The numerical solution for $\langle u_x \rangle$ is shown below:

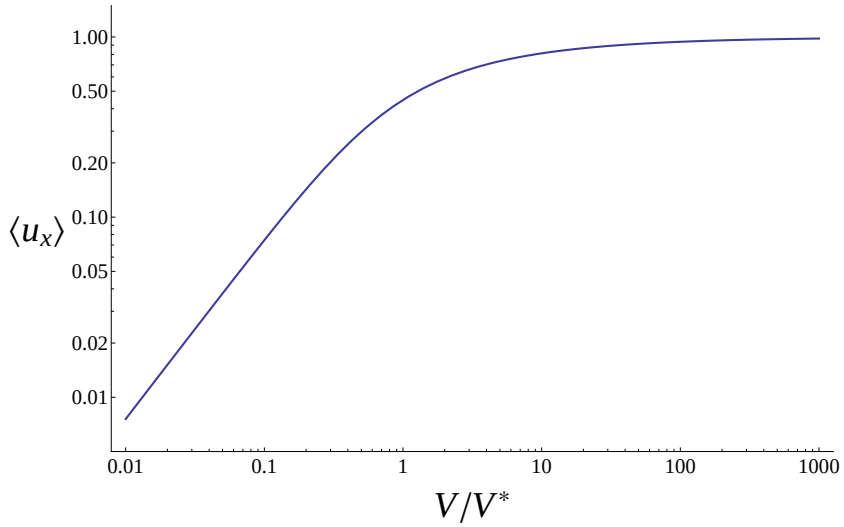

Figure 3.10: Average slip direction interfacial strand alignment vs. slip velocity. Slip velocity in units of the characteristic alignment velocity $V^* = a\mathrm{k_B}T/(L^3\zeta)$. Both axes are in logarithmic scale.

For systems with $V^* \ll V^{**}$ the total number of interfacial entanglements at slip velocities on the order of V^* will be unchanged from the zero slip equilibrium value. If the interfacial stress due to Rouse-like friction is much less than the stress due to strand alignment at slip velocity V^* (as is expected from the arguments in section 3.2.1) the interfacial stress in the regime $V \leq V^*$ will be well approximated by:

$$\langle \sigma_{yx} \rangle \approx 6\rho_0 \frac{\mathrm{k_B}T}{a} \langle u_x \rangle \tag{3.53}$$

In this situation the interfacial stress in the regime $V \leq V^*$ will change only with the degree of strand alignment and will depend on the interfacial slip velocity in the manner shown in the first part of Figure 3.10. It can be seen that the interfacial stress due to strand alignment has the characteristic scale $\sigma^*_{yx} = 6\rho_0\mathrm{k_B}T/a$ as previously given in Equation 3.10. In the lowest slip velocity limit ($V \ll V^*$) the average strand

alignment is given by:

$$\langle u_x \rangle = \frac{3}{4}\left(\frac{V}{V^*}\right) \tag{3.54}$$

Consequently, in the low slip velocity asymptotic limit ($V \ll V^*$) the interfacial stress is expected to behave as:

$$\langle \sigma_{yx} \rangle = \frac{9}{2}\rho_0 \frac{\mathrm{k_B}T}{a}\left(\frac{V}{V^*}\right) \tag{3.55}$$

The analysis of interfacial strand alignment is not much affected by the possibility of multiple interfacial slip-links per polymer so long the characteristic velocity of strand alignment V^* remains much smaller than the characteristic velocity of interfacial disentanglement. The presence of multiple interfacial slip-links per polymer increases polymer retraction and reduces the characteristic velocity of disentanglement by a factor of the number of interfacial slip-links $V_M^{**} = V^{**}/(M+1)$. So long as $V^* \ll V_M^{**}$ the presence of multiple interfacial entanglements per polymer would not alter the alignment analysis.

3.4.3 Rouse-like Stress

An expression of the stress caused by Rouse-like friction at the polymer-polymer interface can be obtained if the interface is considered to have structure as described by polymer self-consistent field theory. To begin, consider the Rouse-like friction on a translating monomer.

If the friction coefficient for interactions between the polymer species is the same as the friction coefficient for polymer self interactions, the frictional force f_A acting on one monomer of species A surrounding by species B monomers translating at velocity V is given by:

$$f_A = \xi V \tag{3.56}$$

The polymer melts are considered to be incompressible such that the total monomer density is ρ_M (monomers per volume, including polymers monomers of both species). The monomer volume fractions $\phi_A(\vec{r})$ and $\phi_B(\vec{r})$, are defined as the ratios of the local A and B monomer densities to the total monomer density. The volume fractions thus obey the relation $\phi_A(\vec{r})+\phi_B(\vec{r}) = 1$. If a species A monomer is only partly surrounded by translating species B monomers the fraction of surrounding monomers that are species B will simply be $\phi_B(\vec{r})$. Considering a perfect slip situation the frictional force on such a monomer is approximated as:

$$f_A(\vec{r}) = \phi_B(\vec{r})\xi V \tag{3.57}$$

The probability that a species A monomer will be located in a small volume $d\mathcal{V}$ about position $\vec{r}$ will be:

$$P_A(\vec{r})d\mathcal{V} = \frac{\rho_M \phi_A(\vec{r})d\mathcal{V}}{\mathcal{N}_A} \tag{3.58}$$

Here $\mathcal{N}_A$ is the total number of species A monomers. If the polymer species are strongly immiscible the density of species A monomers near the interface is approximated by the theory of Helfand and Tagami [51, 52] as $\phi_A = \alpha^2/(1+\alpha^2)$, with $\alpha \equiv \exp(y/w)$, w the interfacial width, and y the position perpendicular to the planar interface. The interfacial width is $w = b/\sqrt{6\chi}$, with χ being the inter-species interaction parameter. Helfand and Tagami derive this approximate expression for the interfacial volume fraction profile assuming a strongly immiscible interface [51,52], and it is used below to make integration over the interfacial region possible. In this description the density profiles for the two species are only functions of the distance perpendicular to the interface y.

The average Rouse-like frictional force experienced by a single species A monomer

is then given by:

$$\langle f_A \rangle = \int \xi V \frac{\rho_M}{\mathcal{N}_A} \phi_A(y) \phi_B(y) d\mathcal{V} = \xi V \frac{\rho_M A_y}{\mathcal{N}_A} \int \phi_A(y) \left(1 - \phi_A(y)\right) dy \tag{3.59}$$

The average total frictional force experienced by all species A monomers will simply be $\mathcal{N}_A \langle f_A \rangle$, and the average Rouse-like stress will just be this force divided by the interfacial area A_y. Thus the average Rouse-like stress is given by:

$$\langle \sigma_{yx}^R \rangle = \rho_M \xi V \int \phi_A(y) \left(1 - \phi_A(y)\right) dy \tag{3.60}$$

Performing this integration and assuming the thickness of the two melts is much larger than the interfacial width results in:

$$\langle \sigma_{yx}^R \rangle = \frac{\rho_M w}{2} \xi V \tag{3.61}$$

Expressing the total monomer density as the inverse monomer volume $\rho_M = 1/\nu$ the stress can be further expressed:

$$\langle \sigma_{yx}^R \rangle = \frac{w}{2\nu} \xi V = \frac{b}{2\nu\sqrt{6\chi}} \xi V \tag{3.62}$$

These expressions predict the interfacial Rouse-like stress in terms of physical quantities. In a similar manner an expression for the average number of interfacial entanglements per area at equilibrium ρ_0 may be obtained. Taking N_e^{-1} as the probability per monomer of forming an entanglement, and assuming the probabilities for the species identity of each entanglement are given by the local species density fraction, the probability that a species A monomer has become entangled with a species B chain is given by:

$$P_{AB}(\vec{r}) = \frac{\phi_B(\vec{r})}{N_e} \tag{3.63}$$

The average number of species B entanglements for any single species A monomer is then given by:

$$\langle P_{AB} \rangle = \int \frac{\rho_M}{\mathcal{N}_A} \phi_A(y) \phi_B(y) \frac{1}{N_e} d\mathcal{V} \tag{3.64}$$

The average number of interfacial (inter-species) entanglements per area is then $\rho_0 = (\mathcal{N}_A / A_y) \langle P_{AB} \rangle$. Solving for this quantity in exact analogy to the method used in finding the Rouse-like stress the result is:

$$\rho_0 = \frac{1}{N_e} \frac{w}{2\nu} = \left(\frac{b}{a} \right)^2 \frac{w}{2\nu} \tag{3.65}$$

Using these results the slip velocity V_R at which the Rouse-like stress will be equal to the characteristic alignment stress $\sigma_R \approx \sigma^*_{yx}$ (Equation 3.10) may be obtained:

$$V_R = \frac{6}{\xi} \left(\frac{b}{a} \right)^2 \frac{\mathrm{k_B} T}{a} \tag{3.66}$$

This may be compared to the characteristic slip velocity of interfacial entanglement destruction V^{**} (Equation 3.24):

$$V_R = 6 \left(\frac{L}{a} \right)^2 V^{**} \tag{3.67}$$

Consequently, for strongly confined polymers ($a \ll L$) the Rouse-like stress only becomes equal to the characteristic entanglement stress at high slip velocities ($V \gg V^{**}$) at which the interface has become disentangled.

3.4.4 Asymptotic Stress Solutions

If a system has the average spatial distance between entanglements a much less than the total polymer primitive path length L the characteristic slip velocities V^* and $V^{**} = (L/a)V^*$ will be widely separated. In such a case the interfacial stress /

slip velocity relationship can be largely constructed using the asymptotic solutions from the previous sections. For slip velocities up to the characteristic velocity of interfacial strand alignment $V \leq V^*$ the interfacial stress will be given by Equation 3.47, and the numerical solution for strand alignment $\langle u_x \rangle$ shown in Figure 3.10 may be used. In this slip velocity regime the number of entanglements is unchanged from the equilibrium value, and stress increase is due to interfacial strand alignment.

For slip velocities on the order of the characteristic velocity of interfacial entanglement destruction V^{**} the interfacial stress will be given by Equation 3.45. In this regime the interfacial polymer strands are nearly aligned in the slip direction, and further stress changes are due to slip induced entanglement destruction. At slip velocities between V^* and V^{**} an approximate stress plateau exists where the interfacial strands are nearly aligned in the slip direction, but slip induced entanglement destruction has not significantly altered the number of interfacial entanglements.

If multiple slip-links per interfacial polymer are present polymer retraction is increased and the slip velocity of interfacial disentanglement is decreased; $V_M^{**} = V^{**}/(M+1)$, with $M+1$ being the total number of interfacial entanglements per interfacial polymer. Such a situation would decrease the separation of strand alignment and interfacial disentanglement velocities, and would decrease the width of the stress plateau. The probability of multiple interfacial entanglements per polymer is governed by the dimensionless constant $\lambda_I = (w_I/a)\sqrt{L/a}$, where w_I is the interfacial width. For a very narrow interface (strongly repulsive melts with high χ parameter) with $\lambda_I \ll 1$ each interfacial polymer will tend to have at most one interfacial slip-link.

The Rouse-like friction contribution to interfacial stress is expected to be present at all slip velocities but to only become comparable to the characteristic entanglement stress σ_{yx}^* at slip velocity $V_R = 6(L/a)^2 V^{**}$. For this reason the model shows an interfacial stress decrease in the regime $V^{**} < V < V_R$, due to interfacial entanglement

loss occurring before the Rouse-like stress becomes dominant.

Below is a plot of the interfacial stress as a function of slip velocity as predicted by this model for a system with $L = 100a$ and a narrow interfacial width (the single slip-link per interfacial polymer regime).

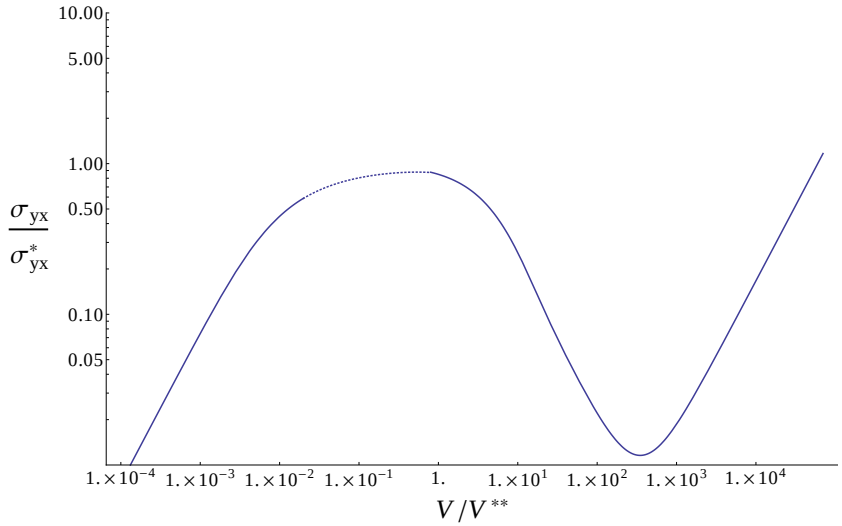

Figure 3.11: Interfacial stress vs. slip velocity asymptotic solutions. The solid lines are asymptotic solutions, the dotted line is an interpolation. Stress is in units of the characteristic stress $\sigma^*_{yx} = 6\rho_0 k_B T/a$. Slip velocity is in units of the characteristic velocity for onset of slip-link destruction $V^{**} = \frac{k_B T}{L^2\zeta}$. The plot is for a system with $L = 100a$. This gives $V^* = V^{**}/100$ and $V_R = 60000V^{**}$. The solutions use the single interfacial slip-link per interfacial polymer approximation. Both axes are in logarithmic scale.

In Figure 3.11 the dotted line is an interpolation between the asymptotic solutions. The low slip velocity asymptotic solution assumes unperturbed reptative chain relaxation, and in this regime stress increase is dominated by strand alignment. The high slip velocity asymptotic solution assumes strands are nearly aligned in the direction of slip, and that slip-induced retraction is the dominant mechanism of motion for interfacially entangled polymers.

3.5 Conclusions

The model of stress induced polymer-polymer interfacial slip here presented uses a slip-link description of interfacial entanglement, and considers a sharply defined polymer-polymer interface experiencing perfect slip. The model predicts that interfacial stress during slip will result as a competition of the slip direction alignment of polymer strands with approximately thermal equilibrium tension, and the destruction of interfacial entanglements through retractive polymer motion. Additionally, Rouse-like rubbing friction in the interfacial region contributes to the interfacial stress in an amount proportional to the slip velocity.

At slip velocities greater than $V^* \sim a/t_{rep}$ polymer strands connected to an interfacial entanglement will be primarily aligned in the direction of slip. At slip velocities greater than $V^{**} \sim L/t_{rep}$ the number of interfacial entanglements becomes significantly depleted due to slip-induced retractive polymer motion. If the polymers are strongly confined by topological interactions with their neighbors (highly entangled, $a \ll L$) the characteristic slip velocities V^* and V^{**} will be widely separated ($V^* \ll V^{**}$). In such a situation an interfacial stress plateau is expected in the slip velocity region $V^* < V < V^{**}$. At these slip velocities interfacial strands will be primarily aligned in the slip direction, but the number of interfacial entanglements will not be changed from the zero slip equilibrium value. The model predicts the value of the plateau stress will be $\sigma^*_{yx} \sim 6\rho_0 \mathrm{k_B}T/a$. This plateau stress corresponds to a zero slip equilibrium number of interfacial entanglements per area ρ_0, each connected to two polymer strands with equilibrium tension $\tau_0 = 3\mathrm{k_B}T/a$ fully aligned in the slip direction. If the polymers are strongly confined interfacial slip does not significantly change the polymer tensions from the equilibrium tension value. If $M+1$ interfacial entanglements per interfacially entangled polymer are present when in equilibrium

without slip the entanglement depletion slip velocity is expected to be reduced by a factor of $M+1$; that is, $V_M^{**} = V^{**}/(M+1)$. The probability of having multiple interfacial entanglements per polymer is governed by the dimensionless quantity $\lambda_I = (w_I/a)\sqrt{L/a}$, where w_I is the interfacial width. In the regime $\lambda_I \ll 1$ (the strongly segregated narrow interface regime) interfacial polymers will tend to have at most one interfacial entanglement.

In the case of strong polymer confinement ($a \ll L$) interfacial stress at slip velocities $V < V^*$ will be due to the slip direction alignment of polymer strands possessing equilibrium tension. For slip velocities in the region $V^* < V < V^{**}$ a stress plateau is present because interfacial polymer strands are nearly aligned in the slip direction (thus no further stress increase due to alignment is possible), and the number of interfacial entanglements remains unchanged from the equilibrium value. At larger slip velocities, $V > V^{**}$, the model predicts a stress decrease (relative to the plateau stress) due to significant destruction of interfacial entanglements through slip-induced polymer retraction.

A contribution to interfacial stress due to Rouse-like rubbing friction is always present, and this contribution increases linearly with the slip velocity. However, it is found that the stress due to Rouse-like friction only becomes comparable to the plateau stress due to strand alignment at a slip velocity $V_R \sim (L/a)^2 V^{**}$. Consequently the Rouse-like stress is not expected to become dominant until nearly all interfacial entanglements have been destroyed, and the interface is no longer entangled.

Chapter 4

Simulation of Entangled Polymers Via the Slip-link Model

A computer simulation of entangled polymers was constructed in order to further examine the phenomenon of stress induced polymer-polymer interfacial slip, and to check the predictions made by the analytic theory developed in Chapter 3. In this chapter an overview of the basic structure of the simulation is given, and the "slip-link" model of polymer entanglement is explained. The slip-link simulation is based on a model developed by Schieber et al. [145–157], which is implemented via a dynamic Monte Carlo algorithm. The discussion in this chapter focuses on the fundamental model and algorithm used to simulate entangled polymers. In subsequent chapters a generalization of the model which makes possible the simulation of polymer-polymer interfaces is explained.

4.1 Fundamental Simulation Description

A dynamic Monte Carlo polymer simulation was constructed in order to study polymer-polymer interfacial slip. The basic simulation model employed for bulk polymer melts

is taken from the work of Schieber et al. [145–157]. The model treats a polymer as a Gaussian filament, and treats entanglements between polymers as ring-like constraints called "slip-links", through which a polymer is able to diffuse. The total number of slip-links on a polymer is allowed to vary, and slip-links are created and destroyed at polymer ends according to rates satisfying a detailed balance condition. The simulation uses a Monte Carlo algorithm in which the Monte Carlo moves are designed to reproduce physically realistic dynamics. The specific axioms and assumptions of the model are outlined in detail below.

In the simulation a polymer is modeled as a Gaussian filament; by this it is meant that a polymer is treated as a non-self-interacting continuous thread capable of stretching according to a spring-like force law linear in the end-to-end distance. The spring like force law used gives the stretching force at the end of one polymer section as:

$$\vec{f} = \frac{3\mathrm{k_B}T}{N_s b^2}\vec{Q}_s \tag{4.1}$$

Here $\mathrm{k_B}$ is Boltzmann's constant, T is the absolute temperature, and $\vec{Q}_s$ is the polymer section end-to-end vector. b is a length parameter known as the statistical segment length, and N_s is a dimensionless measure of the polymer section contour length. N_s is referred to as the arc length or contour length of the polymer. The total polymer is considered to have contour length N and end-to-end vector $\vec{Q}$. The force expression in Equation 4.1 may be easily integrated to give the polymer section stretching energy $E = (3\mathrm{k_B}T/2N_s b^2)\vec{Q}_s^2$ (this may be interpreted as a free energy if the stretching force is thought of as having a partly entropic origin). When the polymer is present in a thermal bath at temperature T this makes the polymer section end-to-end length

probability density $G_0(\vec{Q}_s; N_s)$ a Gaussian function:

$$G_0(\vec{Q}_s; N_s) = \left(\frac{3}{2\pi N_s b^2}\right)^{3/2} \exp\left[-\frac{3\vec{Q}_s^2}{2N_s b^2}\right] \tag{4.2}$$

The distribution in Equation 4.2 results in the polymer section root-mean-square end-to-end vector value being $\sqrt{\langle \vec{Q}_s^2 \rangle} = \sqrt{N_s} b$. The end-to-end vector probability density and root-mean-square value are thus the same as a long random walk of N_s straight steps, each step having length b (valid mapping to a random walk requires $N_s \gg 1$). For this reason N_s is sometimes referred to as the number of statistical segment lengths present in the polymer section contour. However, it should be emphasized that the Gaussian filament is not in any way discrete. Additionally, the specification of a Gaussian filament using N_s and b is not unique, and rescaling these parameters by a constant C according to $N_s \to N_s/C$ and $b \to \sqrt{C}\, b$ gives the same polymer section statistics and behavior. Because a Gaussian filament is by nature capable of stretching, this polymer model does include contour length fluctuations. A Gaussian filament is a physically realistic model for polymers in a melt of the same polymer species in that sufficiently long polymer sections (long enough to be flexible) show Gaussian end-to-end distance correlations.

In the simulation entanglements between polymers are represented as "slip-links". In this model a slip-link is a ring-like constraint fixed in space through which a polymer is able to slide. A polymer possessing a slip-link is constrained to pass through the slip-link, but the slip-link does not constrain the polymer direction (tangent vector). In this model slip-links are created and destroyed only in regions near the polymer ends when the chain forms or releases entanglements during motion (this model does not consider constraint release [42, 43]).

This simulation treats a polymer as a Gaussian filament, and entanglements as

slip-links. Slip-links represent topological entanglements between polymers, though in simulation the polymers are treated as being independent. The slip-link model thus provides a way to simulate entangled polymers without directly simulating complicated inter-polymer interactions. In order to speed computation only slip-link space and arc positions are resolved, and the influence of the polymer between slip-links is treated using a mean field (average influence) approximation. In other words, a polymer configuration is fully specified by the slip-link space and arc positions, and sections of a polymer between slip-links are considered to equilibrate instantly. This model is coarse grained in both space and time: intra-slip-link configuration information is treated only through the mean field influence, and dynamics on time scales on the order of the intra-slip-link equilibration time or shorter are not resolved.

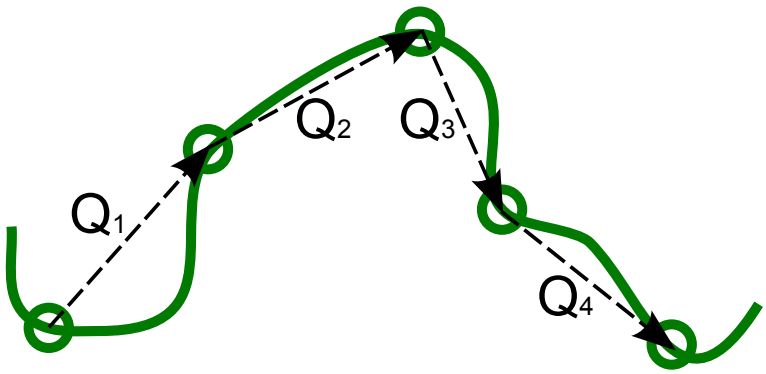

Figure 4.1: An illustration of the model used to simulate entangled polymers. Here a polymer is shown passing through ring-like slip-links, which represent entanglements with other polymers. Slip-links are fixed in space, but the polymer can slide through them. Slip-links are created and destroyed near the polymer ends. A basic polymer configuration is denoted by the number of slip-links Z, the set of strand end-to-end vectors connecting slip-links $\{\vec{Q}_i\}$ (these are shown in the diagram), and the set of strand arc-lengths $\{N_i\}$ (the strand arc-lengths must sum to the total polymer arc-length N, and a strand cannot have negative arc-length). Slip-links are labeled from 1 to Z beginning near a polymer end. The vector $\vec{Q}_i$ points from the i slip-link to the $i+1$ slip-link, and the polymer strand between these two slip-links has arc-length N_i. The two "dangling end" strands have arc lengths N_0 and N_Z respectively.

Taking Z to be the total number of slip-links present on a polymer, the slip-links divide the polymer arc-length into $Z+1$ strands. Two of these strands are end-strands, leaving $Z-1$ interior strands. In this model the configuration of a single polymer with contour length N is fully specified by the number of slip-links Z, the set of polymer strand arc-lengths $\{N_i\}$, and the set of interior strand end-to-end vectors $\{\vec{Q}_i\}$; an additional overall position vector is needed for full configuration specification in the presence of interacting polymers or an anisotropic field. In the slip-link labeling convention slip-links along the polymer contour are numbered sequentially beginning with 1, and strands along the polymer contour are number sequentially in the same

direction as the slip-links but beginning with 0. The polymer strand end-to-end vectors are given the same label as the polymer strands; $\vec{Q}_i$ connects the slip-links labeled i and $i+1$. In this convention the polymer strand labeled i has contour length N_i and end-to-end vector $\vec{Q}_i$, and is flanked by the slip-links labeled i and $i+1$. The set of polymer strand arc lengths are subject to the requirements $N_i \geq 0$ and $\sum_i N_i = N$ (no strand can have negative arc-length, and the strand arc-lengths must sum to the total polymer length). Because slip-links are central to the description of this polymer model (unentangled sections between slip-links are considered to equilibrate instantly) each simulated polymer is required to have at least one slip-link, and so Z is constrained to be a positive integer ($Z > 0$).

A physically motivated equilibrium configuration probability distribution for the model must be specified. In the model the choice is made to specify the equilibrium configuration probability distribution following the model of Schieber et al. [145–157]. The total probability of a configuration having Z slip-links in equilibrium is taken as proportional to β^{-Z}, where β is a user specified parameter (β is later shown to have a close relation to the average arc-length between slip-links). In equilibrium every possible strand arc-length configuration for a given number of slip-links is taken to be equally probable: in equilibrium the slip-links are evenly randomly distributed along the polymer backbone. Finally, consistent with the Gaussian strand model, for any strand of a specified arc-length the end-to-end vector probability density is taken to be Gaussian. Altogether these modeling choices are sufficient to define the total configuration probability density:

$$P(Z, \{N_i\}, \{\vec{Q}_i\}) = \frac{J}{\beta^Z} \prod_{i=1}^{Z-1} G_0(\vec{Q}_i; N_i) \tag{4.3}$$

$$P(Z,\{N_i\},\{\vec{Q}_i\}) = \frac{J}{\beta^Z}\prod_{i=1}^{Z-1}\left(\frac{3}{2\pi N_i b^2}\right)^{3/2}\exp\left[-\frac{3\vec{Q}_i^2}{2N_i b^2}\right] \tag{4.4}$$

G_0 is the Gaussian vector distribution as given in Equation 4.2. β^{-1} acts as the activity for slip-links in the grand canonical ensemble of slip-links present on the simulated polymer (constrained to $Z \geq 1$); β can be expressed in terms of a slip-link "chemical potential" μ_Z with $\beta^{-1} = \exp[\mu_Z/\mathrm{k_B}T]$. J is a normalization constant. Requiring that the total probability be one after integrating over all $\{\vec{Q}_i\}$, all allowed $\{N_i\}$ (subject to the requirement $\sum_i N_i = N$, with each $N_i \geq 0$), and summing over all Z (from $Z = 1$ to ∞), the value of J is found to be:

$$J = \left(\exp\left[\frac{N}{\beta}\right] - 1\right)^{-1} \tag{4.5}$$

In the long polymer case such that $N \gg \beta$ this rapidly approaches $J = e^{-N/\beta}$.

Equation 4.4 is the polymer equilibrium configuration probability density chosen for this model, and the probability of finding a polymer in an infinitesimal region in configuration space near some configuration specified by Z, $\{N_i\}$, $\{\vec{Q}_i\}$ is equal to $P(Z,\{N_i\},\{\vec{Q}_i\})d\{N_i\}d\{\vec{Q}_i\}$. Here $d\{N_i\} \equiv dN_1 dN_2 ... dN_{Z+1}$ and $d\{\vec{Q}_i\} \equiv d\vec{Q}_1 d\vec{Q}_2 ... d\vec{Q}_{Z-1}$, with $d\vec{Q} \equiv dQ_x dQ_y dQ_z$.

For notational convenience throughout the rest of this work a particular polymer configuration shall be denoted by Ω_j such that Ω_j is the set of all the quantities defining that configuration:

$$\Omega_j \equiv \{Z,\{N_i\},\{\vec{Q}_i\}\}_j \tag{4.6}$$

In this notation $P(\Omega_j)$ is just the particular value of the probability density (Equation 4.4) associated with configuration Ω_j. Similarly $d\Omega_j \equiv d\{N_i\}_j d\{\vec{Q}_i\}_j$. Altogether

this makes the probability that a polymer will be found in configuration Ω_j equal to $P(\Omega_j)d\Omega_j$.

4.1.1 Model Equilibrium Distributions

The full equilibrium configuration distribution $P(Z, \{N_i\}, \{\vec{Q}_i\})$ given in Equation 4.4 can be used to derive the equilibrium distributions of some other physical quantities. As before stated, the configuration probability density is chosen such that all possible strand arc-length configurations $\{N_i\}$ are equally probable, and the slip-links are evenly randomly distributed along the polymer contour. This can be seen from the form of Equation 4.4; integrating the configuration probability density over all end-to-end vectors $\{\vec{Q}_i\}$ gives a probability density $P(Z, \{N_i\})$ that is independent of the strand arc-length configuration $\{N_i\}$:

$$P(Z, \{N_i\}) = \int d\{\vec{Q}_i\} P(Z, \{N_i\}, \{\vec{Q}_i\}) = \left(e^{N/\beta} - 1\right)^{-1} \beta^{-Z} \tag{4.7}$$

Equation 4.7 does not depend on the strand arc-lengths N_i, and this indicates that each arc-length configuration $\{N_i\}$ is equally probable in the ensemble of configurations averaged over all strand end-to-end vectors $\vec{Q}_i$. Consequently the slip-links are evenly randomly distributed along the polymer arc-length in this ensemble.

The expected distribution for the number of slip-links Z on a simulated polymer may be obtained by integrating Equation 4.7 over all possible strand arc-lengths, subject to the constraints $\sum_i N_i = N$, and $N_i \geq 0$, giving the result:

$$P(Z) = (e^{N/\beta} - 1)^{-1} \frac{N^Z}{\beta^Z Z!} \tag{4.8}$$

Equation 4.8 indicates that equilibrium number of slip-links Z on a simulated polymer in this model follows a Poisson distribution confined to the range $Z \geq 1$.

The average number of slip-links on a single polymer in equilibrium may be obtained using the distribution in Equation 4.8:

$$\langle Z \rangle = \sum_{Z=1}^{\infty} Z P(Z) = \left(\frac{e^{N/\beta}}{e^{N/\beta} - 1} \right) \frac{N}{\beta} \tag{4.9}$$

For $N > \beta$ this rapidly approaches $\langle Z \rangle \approx N/\beta$.

Similarly, it is possible to derive the probability distribution for the arc-length in a single strand. Integrating $P(Z, \{N_i\})$ from Equation 4.7 over all possible strand arc-lengths less one gives the result:

$$P(Z, N_s) = \left(e^{N/\beta} - 1\right)^{-1} \beta^{-Z} \frac{(N - N_s)^{Z-1}}{(Z-1)!} \tag{4.10}$$

Here N_s is the arc-length of the single-strand excluded from the arc-length integration, and the result is the same regardless of the position of this strand relative to other polymer strands. The distribution in Equation 4.10 is subject to the constraints $0 \leq N_s \leq N$ and $Z > 0$.

The probability distribution for the arc-length of a single strand may be obtained by summing $P(Z, N_s)$ over all possible slip-link numbers Z. That is, $P(N_s) = \sum_{Z=1}^{\infty} P(Z, N_s)$. As can be seen from the form of Equation 4.10, this sum is identically equal to an exponential function, such that $P(N_s)$ is given by:

$$P(N_s) = \left(\frac{e^{N/\beta}}{e^{N/\beta} - 1} \right) \beta^{-1} \exp\left[-\frac{N_s}{\beta} \right] \tag{4.11}$$

Equation 4.11 indicates that the equilibrium strand arc-length probability distribution is expected to be a decaying exponential with characteristic decay arc-length β. The arc-length of a polymer strand between slip-links is constrained to be non-negative, and not larger than the total polymer arc-length ($0 \leq N_s \leq N$).

The average arc-length of a polymer strand may be obtained using the arc-length distribution in Equation 4.11:

$$\langle N_s \rangle = \int dN_s \, N_s P(N_s) = \left(\frac{e^{N/\beta}}{e^{N/\beta} - 1} \right) \left(\beta - e^{-N/\beta}(N + \beta) \right) \tag{4.12}$$

For $N > \beta$ this rapidly approaches $\langle N_s \rangle \approx \beta$.

It can be seen from the average strand arc-length expression in Equation 4.12, and the average slip-link number expression in Equation 4.9, that the parameter β serves as a measure of the equilibrium average arc-length between slip-link entanglements. For simulated polymers with $N/\beta > 7$ the value of β will be equal to the average equilibrium strand arc-length to within less than one percent.

4.2 Monte Carlo Implementation

The simulation uses two fundamental Monte Carlo moves: an arc-length shuffle move, and a slip-link create/destroy move. Each Monte Carlo move is composed of two parts, a probabilistic move proposal, and a probabilistic move acceptance determination. The move proposal and acceptance probabilities are chosen so that the model exhibits realistic physical dynamics, and so that detailed balance in the equilibrium state is satisfied such that the equilibrium polymer configuration probability density is given by Equation 4.4.

The simulation consists of the repeated application of Monte Carlo moves to polymer configurations. As the simulation progresses the identity of the next Monte Carlo move to be performed, either an arc-length shuffle move or a slip-link create/destroy move, is decided probabilistically using a user defined probability ratio for these two move types. Detailed balance is satisfied regardless of the ratio of these two move types (though a finite probability for both moves types is necessary). In simula-

tion the choice is made to perform enough slip-link create/destroy moves relative to the number of shuffle moves that the end regions of the strands in which slip-link creation/destruction is allowed are in effect always in a state of equilibrium (end slip-links are then being relatively rapidly created and destroyed in these regions). In the systems studied it has been found that when approximately 5% or more of the attempted total performed Monte Carlo moves are slip-link create/destroy moves this condition of end-strand create/destroy equilibrium is obtained. If this type of end-strand equilibrium is obtained the simulation dynamics are insensitive to further increases in relative number of create/destroy moves (a higher relative number of create/destroy moves then only makes the simulation less computationally efficient).

A polymer is not allowed to have less than one slip-link as the model treats unentangled polymer sections as equilibrating instantly, and thus the coarse graining approximations of this model make it inapplicable to unentangled polymers.

4.2.1 Monte Carlo Move: Arc-length Shuffle Move

An arc-length shuffle move moves arc-length from one polymer strand to another across a slip-link. The proposed amount of arc-length to shuffle ΔN is generated from a probability distribution chosen to represent thermal Brownian motion diffusion of polymer contour across a slip-link. The probability density for the proposed amount of arc to shuffle in one shuffle move is:

$$P(\Delta N) = \left(\frac{\zeta_s}{4\pi Z \Delta t \mathrm{k_B} T}\right)^{1/2} \exp\left[-\frac{\zeta_s \Delta N^2}{4 Z \Delta t \mathrm{k_B} T}\right] \tag{4.13}$$

Δt is the timestep associated with one shuffle move; time advancement is associated exclusively with shuffle moves in the simulation, and each shuffle move advances the time by Δt. ζ_s is a friction coefficient associated with arc motion across a slip-link.

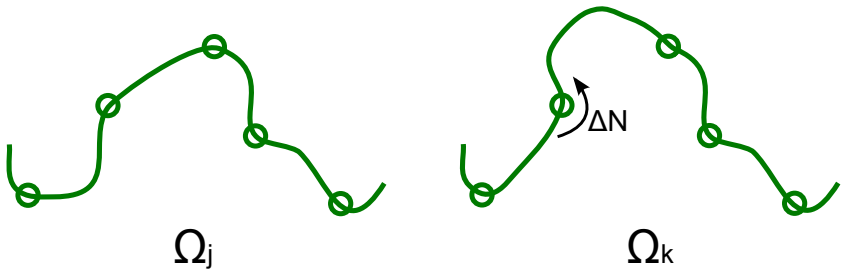

Figure 4.2: An illustration of an arc-length shuffle Monte Carlo move.

In one shuffle move a single slip-link is chosen at random from amongst all Z existing slip-links to have arc length shuffled across it; the probability that a particular slip-link is chosen during a shuffle move is Z^{-1}. The average squared amount of arc shuffled across one particular slip-link during a shuffle move is then given by:

$$\langle \Delta N^2 \rangle = Z^{-1} 2 \frac{Z \mathrm{k_B} T}{\zeta_s} \Delta t = 2 \frac{\mathrm{k_B} T}{\zeta_s} \Delta t \tag{4.14}$$

Equation 4.14 indicates that the average square amount of arc-length proposed to be shuffled across a polymer during a shuffle move obeys the standard diffusion equation form with diffusion constant $D = \mathrm{k_B} T / \zeta_s$. After proposing an amount of arc-length to shuffle a shuffle move is subject to a probabilistic acceptance rate designed to satisfy detailed balance and give the configuration probability distribution in Equation 4.4 in equilibrium. However, if the two strands involved in the shuffle move are both very long ($N_i \gg \Delta N$) the move will be very likely to be accepted, and the average single slip-link arc diffusion will obey Equation 4.14.

A shuffle move acceptance probability is required to ensure that detailed balance is satisfied in the equilibrium state. Detailed balance requires that total transition rates between states are equal in equilibrium. $P(\Omega_j) d\Omega_j$ is the probability that a polymer in equilibrium will be found in configuration Ω_j. Let $R(\Omega_j \rightarrow \Omega_k)$ represent the probability of proposing a move from Ω_j to Ω_k, and $A(\Omega_j \rightarrow \Omega_k)$ be the probability

of accepting such a move. Detailed balance requires:

$$P(\Omega_j)d\Omega_j R(\Omega_j \to \Omega_k)A(\Omega_j \to \Omega_k) = P(\Omega_k)d\Omega_k R(\Omega_k \to \Omega_j)A(\Omega_k \to \Omega_j) \quad (4.15)$$

First it must be stated that if a shuffle move proposal would result in a strand having zero or negative arc-length that proposal is rejected (such configurations are not allowed in the model, and thus have zero probability of acceptance). In the case of shuffle moves the probability $P(\Delta N)d\Delta N$ of proposing a motion of arc length ΔN across a slip-link is equal to the probability of the reverse proposal $P(-\Delta N)d\Delta N$ (Equation 4.13). Consequently for shuffle moves $R(\Omega_j \to \Omega_k) = R(\Omega_k \to \Omega_j)$ and the detailed balance criteria in Equation 4.15 can be rewritten as:

$$\frac{A(\Omega_j \to \Omega_k)}{A(\Omega_k \to \Omega_j)} = \frac{P(\Omega_k)d\Omega_k}{P(\Omega_j)d\Omega_j} \quad (4.16)$$

The probability ratio $P(\Omega_k)d\Omega_k/P(\Omega_j)d\Omega_j$ can be evaluated using the configuration probability distribution in Equation 4.4. The configurations before and after a shuffle move will be in every way identical except for a transfer of arc-length ΔN across one slip-link from one polymer strand to another. Considering a shuffle move transferring arc length ΔN between two interior strands, and taking Ω_j as the configuration before a proposed shuffle move and Ω_k as the configuration after the move (as shown in Figure 4.2), the detailed balance condition for shuffle move acceptance probabilities becomes:

$$\frac{A(\Omega_j \to \Omega_k)}{A(\Omega_k \to \Omega_j)} = \frac{G_0(\vec{Q}_m; N_m - \Delta N)G_0(\vec{Q}_{m+1}; N_{m+1} + \Delta N)}{G_0(\vec{Q}_m; N_m)G_0(\vec{Q}_{m+1}; N_{m+1})} \quad (4.17)$$

$$\frac{A(\Omega_j \to \Omega_k)}{A(\Omega_k \to \Omega_j)} = \left(\frac{N_m}{N_m - \Delta N}\right)^{3/2} \exp\left[\frac{3\vec{Q}_m^2}{2b^2}\left(\frac{1}{N_m} - \frac{1}{N_m - \Delta N}\right)\right] \cdot \left(\frac{N_{m+1}}{N_{m+1} + \Delta N}\right)^{3/2} \exp\left[\frac{3\vec{Q}_{m+1}^2}{2b^2}\left(\frac{1}{N_{m+1}} - \frac{1}{N_{m+1} + \Delta N}\right)\right] \quad (4.18)$$

Here the shuffle move is considered to be moving polymer arc-length ΔN from the number m polymer strand to the neighboring $m+1$ strand, where both of these strands are interior strands. This acceptance ratio can be efficiently implemented in simulation using the Metropolis [160] method. Denoting the value of the right side of Equation 4.18 as λ the in-simulation acceptance probability for a proposed shuffle move is:

$$A(\Omega_j \to \Omega_k) = \begin{cases} \lambda & \text{if } \lambda < 1 \\ 1 & \text{if } \lambda \geq 1 \end{cases} \quad (4.19)$$

This acceptance probability for a proposed shuffle move enforces the acceptance probability ratio between a shuffle move and the reverse shuffle move between two interior strands which is required to satisfy detailed balance in equilibrium (Equation 4.18). The form of the acceptance probability is symmetric under a reversal of which strand is losing and which is gaining the shuffled arc-length. Consequently the shuffle move acceptance probability given in Equations 4.18 and 4.19 is the proper acceptance probability for any shuffle move between interior strands so long as the strand labeled m is taken as the strand losing arc-length during the shuffle move, and the strand labeled $m+1$ is taken as the strand gaining arc-length during the shuffle move. With this move acceptance probability scheme the move acceptance probability ratio required for detailed balance (Equation 4.16) is satisfied for shuffle moves transferring arc-length between interior strands.

If instead of transferring arc-length between two interior strands a shuffle move transfers arc length between an interior strand and an end strand the same type of

analysis can be used to determine the move acceptance probability ratio. Considering a shuffle move transferring arc-length ΔN from an interior strand to an end strand, and taking Ω_j as the configuration before the move and Ω_k as the configuration after, the move acceptance probability ratio required for detailed balance is found to be:

$$\frac{A(\Omega_j \to \Omega_k)}{A(\Omega_k \to \Omega_j)} = \frac{G_0(\vec{Q}_m; N_m - \Delta N)}{G_0(\vec{Q}_m; N_m)} \tag{4.20}$$

$$\frac{A(\Omega_j \to \Omega_k)}{A(\Omega_k \to \Omega_j)} = \left(\frac{N_m}{N_m - \Delta N}\right)^{3/2} \exp\left[\frac{3\vec{Q}_m^2}{2b^2}\left(\frac{1}{N_m} - \frac{1}{N_m - \Delta N}\right)\right] \tag{4.21}$$

Denoting the right side of Equation 4.21 as λ this move acceptance probability ratio can again be enforced in simulation by taking $A(\Omega_j \to \Omega_k)$ to be as given in Equation 4.19. This move acceptance probability once again possesses symmetry such that it is the correct shuffle move acceptance probability to use for any shuffle move transferring arc-length between an interior strand and an end strand, though in this case the strand labeled m must be taken as the interior strand. If arc-length is being transferred from the end strand to the interior strand then the sign of ΔN should be negative. Such a move acceptance scheme satisfies the required acceptance probability ratio in Equation 4.21 for shuffle moves transferring arc-length between an interior stand and an end strand.

If a polymer possesses only one slip-link any proposed shuffle move will be accepted (provided the strands on either side continue to have positive arc-length) as the model configuration given in Equation 4.4 indicates that any arc-length location for a single slip-link is equally probable. In this entangled polymer model a polymer is not allowed to have zero slip-links.

It should be noted that the shuffle move acceptance transition rules can be expressed in a somewhat more common manner (as done by Schieber et al. [146–156])

by defining the free energy of end strands to be identically zero, and then consistently defining the free energy of internal strands to be:

$$\frac{F_s}{\mathrm{k_B}T} \equiv \frac{3\vec{Q}_s^2}{2N_s b^2} - \frac{3}{2}\ln\left[\frac{3}{2\pi N_s}\right] \tag{4.22}$$

If this method is used the appropriate shuffle move acceptance rates may be obtained through the most common formulation of the Metropolis rule: If the total free energy of the configuration after the move is less than the current total free energy the move should be accepted. If the total free energy of the configuration after the move is greater than the current total free energy the move should have acceptance probability $\exp\left[(F_{old} - F_{new})/\mathrm{k_B}T\right]$. I do not focus on this free energy method of expression because the later description of extending the simulation to account for an external chemical potential field is more easily explainable in terms of probabilities and statistical weights. Additionally, actually employing the free energy method in this simulation would involve unnecessary logarithms and exponentiations, and description of the slip-link create/destroy move acceptance rates in terms of free energies is somewhat more delicate. However, this free energy description shall be briefly discussed when considering the model diffusion dynamics, and the calculation of forces and stress at a polymer-polymer interface.

4.2.2 Monte Carlo Move: Slip-Link Create/Destroy Move

In addition to shuffle moves the simulation employs a slip-link create/destroy move which forms or releases new polymer entanglements. The create/destroy move creates or destroys slip-links only within user specified arc-length regions near the polymer ends (the simulation does not include constraint release [42, 43]). This localization of entanglement creation and destruction near the polymer ends is a modeling choice

made to make the model behavior similar to that of well understood tube models of polymer entanglement, in which confining tube sections (entanglements) are created and destroyed only at the polymer ends [36].

When a slip-link create/destroy move is invoked a random decision is made whether to propose a slip-link creation or destruction. When invoking a create/destroy move it is equally probably that a slip-link creation or destruction proposal will be made.

During a polymer slip-link destruction proposal one of the two slip-links nearest to the two polymer ends is chosen at random, and a proposal to remove that slip-link is made. If the slip-link is far enough from the nearest polymer end that it is outside the specified arc-length region for slip-link creation/destruction then it is not destroyed. If the slip-link is within the creation/destruction arc-length region then whether to accept the proposed slip-link destruction is decided using a destruction acceptance probability designed to satisfy detailed balance in equilibrium.

During a polymer slip-link creation proposal one of the two polymer ends is chosen at random to receive a proposed new slip-link. A probabilistic proposal is made for the arc and space locations of the proposed new slip-link. The arc position proposal is made before the space position proposal. The proposed arc position of the new slip-link is chosen using a uniform probability distribution over the arc-length available at the chosen polymer end. The amount of available arc-length is the arc-length between the polymer end and the next slip-link, or the user specified arc-length in which creation/destruction is allowed, whichever is less. After a proposal for the arc position of the new slip-link has been made a proposal for the space position is made using the end-to-end vector probability distribution for a Gaussian strand (Equation 4.2 using the arc-length between the new slip-link and the next nearest slip-link). After the proposed location of the new slip-link has been determined, whether to accept the proposed slip-link creation is decided using a creation acceptance probability designed

to satisfy detailed balance in equilibrium.

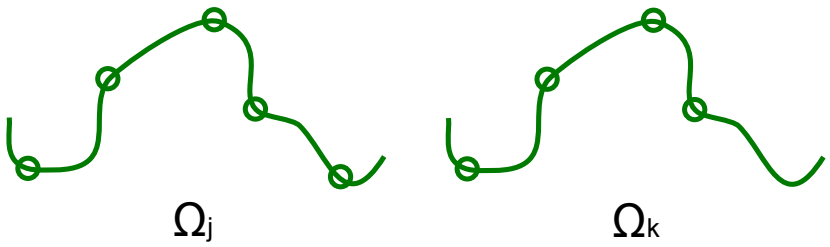

Figure 4.3: An illustration of slip-link create/destroy Monte Carlo moves.

The slip-link creation/destruction move acceptance probability ratio required to satisfy detailed balance can be determined in the same manner as used to determine shuffle move acceptance. Let Ω_j now denote a polymer configuration with Z slip-links, and let Ω_k denote a polymer configuration in every way identical to Ω_j except for the absence of one slip-link nearest to a polymer end (Ω_k has $Z-1$ slip-links, as illustrated in Figure 4.3). In equilibrium detailed balance requires the transition rates between these two states to be equal; this requirement is summarized in terms of move proposal and acceptance probabilities in Equation 4.15.

Applying Equation 4.15 to create/destroy moves $P(\Omega_j)d\Omega_j$ is the equilibrium probability that the polymer will be in the Ω_j state (here the state with Z total slip-links). $R(\Omega_j \to \Omega_k)$ is the probability that a move would propose the transition $\Omega_j \to \Omega_k$. This transition is one of slip-link destruction, and $R(\Omega_j \to \Omega_k)$ is given by:

$$R(\Omega_j \to \Omega_k) = \frac{1}{4} \tag{4.23}$$

This value for $R(\Omega_j \to \Omega_k)$ arises from the probability that a create/destroy move proposes a slip-link destruction (probability 1/2), multiplied by the probability that

the destruction proposal chooses the correct slip-link near one of the polymer ends to propose the transition $\Omega_j \rightarrow \Omega_k$ (also probability 1/2). $A(\Omega_j \rightarrow \Omega_k)$ is the probability that the proposed slip-link destruction move will be accepted.

Similarly, for create/destroy moves $P(\Omega_k)d\Omega_k$ is the equilibrium probability that the polymer will be in the Ω_k state (here the state with $Z-1$ total slip-links). $R(\Omega_k \rightarrow \Omega_j)$ is the probability that a move would propose the transition $\Omega_k \rightarrow \Omega_j$. This transition is one of slip-link creation, and in this case $R(\Omega_k \rightarrow \Omega_j)$ is given by:

$$R(\Omega_k \rightarrow \Omega_j) = \frac{1}{4}\frac{dN_Z}{N_{E*}}\left(\frac{3}{2\pi N_s b^2}\right)^{3/2} \exp\left[-\frac{3\vec{Q}_s^2}{2N_s b^2}\right] d\vec{Q}_s \tag{4.24}$$

The factor of 1/4 in Equation 4.24 once again comes from the product of the probability that a create/destroy move will propose slip-link creation (probability 1/2), and the probability that the randomly selected polymer end chosen to receive the new slip-link will be the correct one to cause the transition $\Omega_k \rightarrow \Omega_j$ (probability 1/2). The factor dN_Z/N_{E*} in Equation 4.24 arises because the arc location of the new slip-link is generated using a uniform distribution over the available arc-length near the polymer end (N_{E*}). N_{E*} is equal to the arc-length present in the dangling polymer end strand N_E, or the arc-length in which slip-link creation/destruction is allowed N_*, whichever is less.

$$N_{E*} = \begin{cases} N_E & \text{if } N_E \leq N_* \\ N_* & \text{if } N_E > N_* \end{cases} \tag{4.25}$$

The Gaussian function in Equation 4.24 arises because the proposed space location of the new slip-link is generated using a Gaussian distribution for the strand end-to-end vector between the new slip-link and its nearest neighbor.

Detailed balance requires the acceptance ratio for Monte Carlo moves be given

by:

$$\frac{A(\Omega_j \to \Omega_k)}{A(\Omega_k \to \Omega_j)} = \frac{P(\Omega_k) d\Omega_k R(\Omega_k \to \Omega_j)}{P(\Omega_j) d\Omega_j R(\Omega_j \to \Omega_k)} \tag{4.26}$$

Applying this to slip-link create/destroy moves using the move proposal probabilities in Equations 4.23 and 4.24, and the appropriate equilibrium configuration probabilities from Equation 4.4, the move acceptance ratio becomes:

$$\frac{A(\Omega_j \to \Omega_k)}{A(\Omega_k \to \Omega_j)} = \frac{\beta}{N_{E*}} \tag{4.27}$$

In simulation this acceptance probability ratio is enforced using the Metropolis criteria:

$$A(\Omega_j \to \Omega_k) = \begin{cases} \frac{\beta}{N_{E*}} & \text{if } \frac{\beta}{N_{E*}} < 1 \\ 1 & \text{if } \frac{\beta}{N_{E*}} \geq 1 \end{cases} \qquad A(\Omega_k \to \Omega_j) = \begin{cases} \frac{N_{E*}}{\beta} & \text{if } \frac{N_{E*}}{\beta} < 1 \\ 1 & \text{if } \frac{N_{E*}}{\beta} \geq 1 \end{cases} \tag{4.28}$$

Throughout most of this work the simulations have the arc-length region of slip-link creation and destruction set to be equal to twice the average entanglement length $N^* = 2N_e = 2\beta$.

The proposal and acceptance probabilities for slip-link create/destroy moves ensure detailed balance in equilibrium by enforcing the slip-link create/destroy acceptance probability condition in Equation 4.27. The proposal and acceptance probabilities for both slip-link create/destroy moves and arc-length shuffle Monte Carlo moves enforce the chosen model equilibrium configuration probability density in Equation 4.4. This can be tested through the examination of the equilibrium distributions of physical polymer properties during simulation.

4.2.3 Simulation Equilibrium Validation

To check the correctness of the simulation the distributions of some physical quantities measured on simulated polymers in equilibrium may be compared to the model equilibrium distributions derived in section 4.1.1. As previously stated, the form of this slip-link model results in all slip-links being evenly randomly distributed along the polymer contour. This may be checked with a histogram of slip-link arc-length positions obtained from simulation:

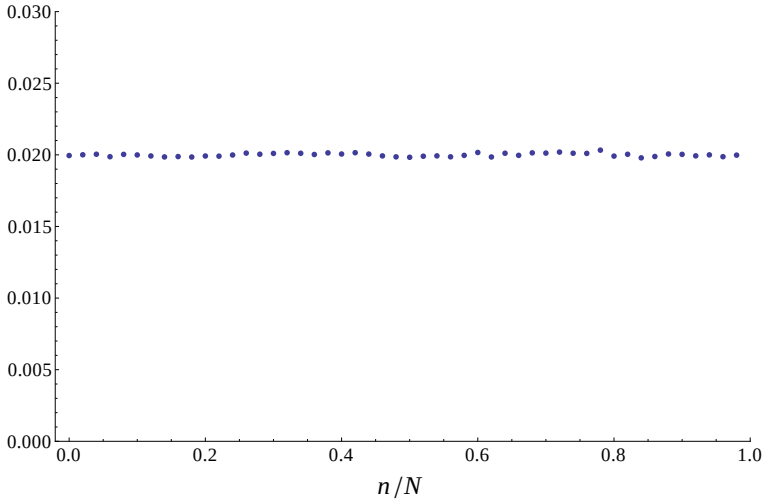

Figure 4.4: Histogram of the slip-link contour position n for simulated polymers at equilibrium. Simulations parameters: $N = 50$, $\beta = 3.125$, simulation timestep $\Delta t = 2.56(10^{-5})t_e$, $t_e \equiv N_e^2 \zeta_s / (\mathrm{k_B}T)$. The histogram is normalized such that the sum of all entries is one.

Figure 4.4 indicates that the average concentration of slip-links along the simulated polymer contour is uniform, as expected for slip-links evenly randomly distributed along the contour. In this and subsequent simulations, the arc-length region of slip-link creation and destruction is set equal to 2β.

The number of slip-links on a simulated polymer fluctuates as slip-links are created and destroyed near the polymer ends. In this model the number of slip-links Z on a polymer is expected to follow a Poisson distribution restricted to $Z \geq 1$ as derived in

Equation 4.8. This may be tested via a histogram of slip-links present on a simulated polymer:

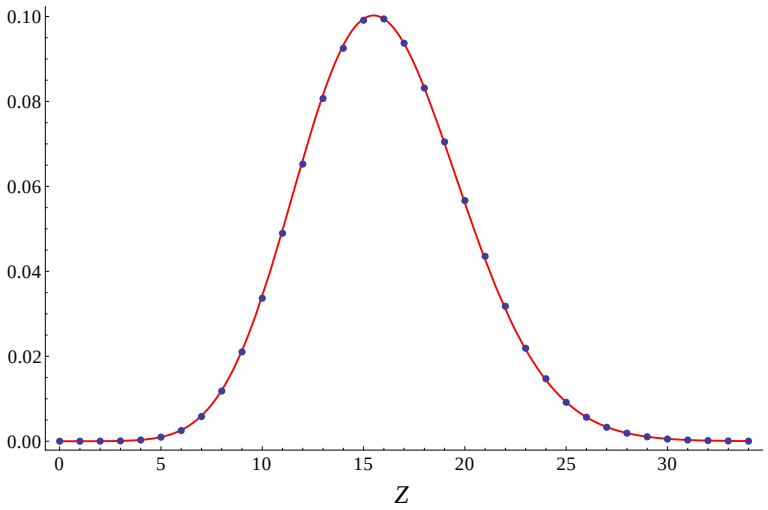

Figure 4.5: Histogram of the number of slip-links Z present on simulated polymers at equilibrium. The red line is the expected distribution function for Z of the form given in Equation 4.8. The histogram is normalized such that the sum of all entries is one. The distribution function is multiplied by a constant to fit the histogram height. Simulation parameters: $N = 50$, $\beta = 3.125$, simulation timestep $\Delta t = 2.56(10^{-5})t_e$, $t_e \equiv N_e^2\zeta_s/(\mathrm{k_B}T)$.

As can be seen in Figure 4.5, in which the red line is the predicted equilibrium total slip-link number distribution function of the form given in Equation 4.8, the expected equilibrium distribution for slip-link number is obtained in simulation.

The distribution for the arc-length between slip-links for any single polymer strand is expected to be a decaying exponential as indicated in Equation 4.11, with the decay length being the simulation parameter β. This may be checked using a histogram of arc-length present in a single strand of a simulated polymer:

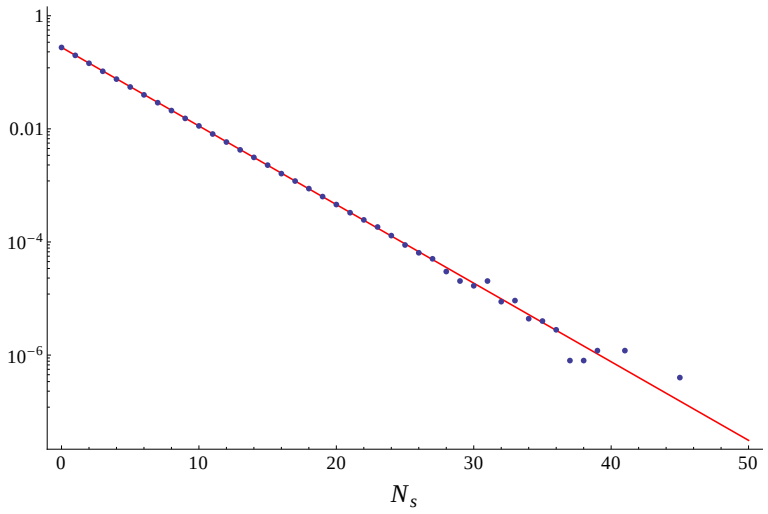

Figure 4.6: Histogram of strand arc-length N_s for simulated polymers at equilibrium. The vertical axis is in logarithmic scale. The red line is the expected exponential distribution function for N_s as given in Equation 4.11. The histogram is normalized such that the sum of all entries is one. The distribution is multiplied by a constant to fit the histogram height. Simulation parameters: $N = 50$, $\beta = 3.125$, simulation timestep $\Delta t = 2.56(10^{-5})t_e$, $t_e \equiv N_e^2 \zeta_s / (\mathrm{k_B}T)$.

As can be seen in Figure 4.6, in which the red line in the predicted equilibrium strand arc-length distribution function of the form given in Equation 4.11, the expected equilibrium strand arc-length distribution is obtained in simulation.

It can be seen that the sampled distributions for slip-link arc position, slip-link number, and strand length, agree with the expected distributions derived from the chosen model configuration density. This indicates that the Monte Carlo move transition probabilities succeed in enforcing detailed balance in equilibrium, with the resulting equilibrium configuration density being that chosen for the model in Equation 4.4.

4.3 Model Diffusion Dynamics: Pseudo-Ring Toy Simulation

In order to study the diffusion dynamics of the simulation model an analysis is made of the mean square arc-length displacement of the polymer over time. In order to do this consistently, a "pseudo-ring" polymer is simulated. A pseudo-ring polymer is a polymer simulated according to the normal model except that the number of slip-links is fixed and the polymer arc-length is treated as periodic; that is, the ends of the polymer are considered connected such that during polymer diffusion when a slip-link moves off one polymer end it moves onto the opposite polymer end. Simulating in this way allows for the analysis of the polymer arc diffusion obtained by this simulation algorithm, and how this diffusion depends on model parameters. A plot of the average square amount of arc-length diffused across a single slip-link as a function of time is shown below.

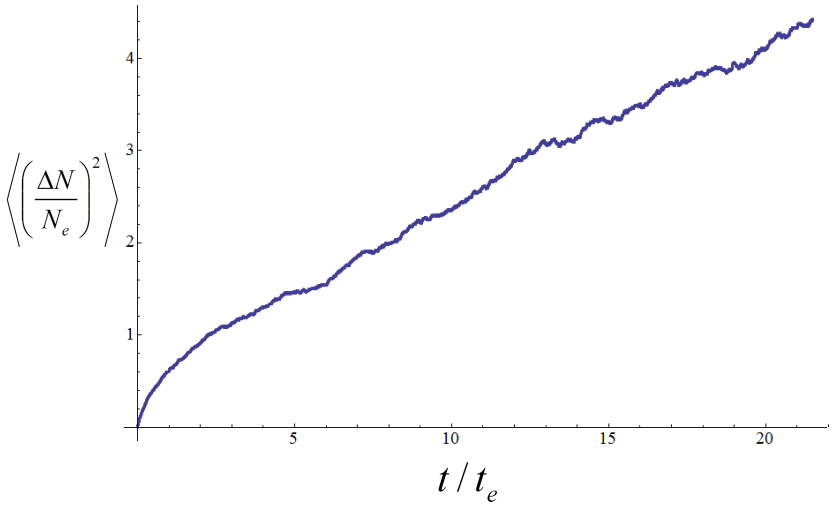

Figure 4.7: Mean square polymer diffusion across a slip-link vs. time for a pseudo-ring polymer. Number of slip-links fixed at $Z = 11$. Simulation parameters: $N = 75$, simulation timestep $\Delta t = 5.38(10^{-6})t_e$, $t_e \equiv N_e^2 \zeta_s / (\mathrm{k_B} T)$.

As can be seen from Figure 4.7 the behavior of the average square amount of arc-length diffused across a slip-link has different distinct regimes. Though the simulation represents diffusion of polymer arc-length across stationary slip-link entanglements, in the analysis of pseudo-ring diffusion it may be more easily thought of as diffusion of slip-links in the space of arc-length, with $\langle \Delta N^2 \rangle$ representing the average squared slip-link displacement in arc-length space. In this sense the diffusion is of the type of non-passing interacting particles (slip-links) around a one dimensional ring.

When analyzing model dynamics the most natural timescale is the characteristic time to diffuse an entanglement arc-length (see Equation 4.14):

$$t_e = \frac{N_e^2 \zeta_s}{\mathrm{k_B} T} \tag{4.29}$$

Here N_e is the average arc-length between slip-link entanglements. t_e is used as the

time unit when discussing the dynamics of this model, and arc-lengths are considered in ratio to the entanglement arc-length N_e. t_e is also the relevant timescale to consider for questions of simulation convergence with timestep (the dynamics are expected to converge when the simulation timestep $\Delta t \ll t_e$).

When performing pseudo-ring polymer simulations the slip-links are first randomly placed along the polymer arc-length, and then strand end-to-end vectors $\vec{Q}_s$ are generated using the Gaussian probability distribution in Equation 4.2. In the pseudo-ring simulation the number of slip-links remains constant, and the strand end-to-end vectors remain fixed after generation.

In the shortest time regime $\langle \Delta N^2 \rangle$ is linear with time, and the slope is equal to $2\mathrm{k_B}T/\zeta_s$ as expected from the shuffle move proposal probability distribution for arc-length diffusion across a single slip-link between long strands (Equation 4.14). In this time regime diffusion across slip-links occurs in an independent manner. Intuitively speaking, in the shortest time regime the slip-links have not yet moved sufficiently in arc-length space to develop any collective motion, and thus diffuse independently. This behavior can be confirmed via a pseudo-ring simulation done with relatively long strands:

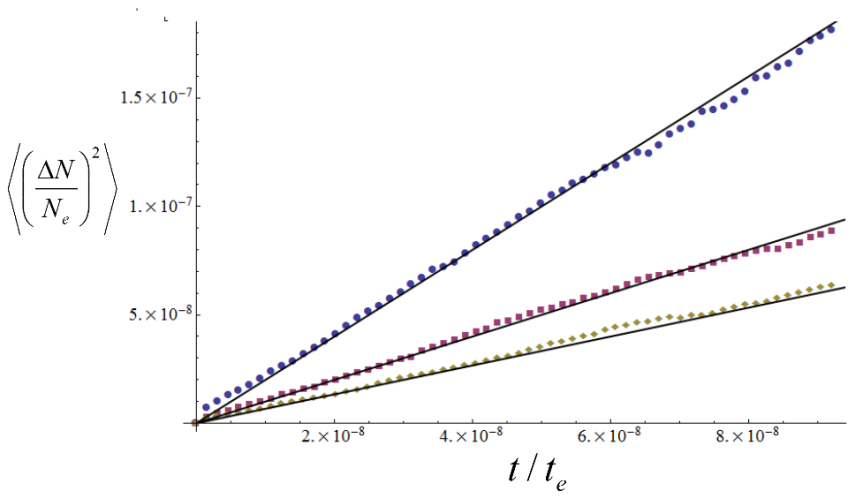

Figure 4.8: Early time mean square polymer diffusion across a slip-link vs. time for a pseudo-ring polymer using three different diffusion constants $D = \mathrm{k_B}T/\zeta_s$. The points are simulation data while the lines are the expected behavior from Equation 4.14; in this plot the predicted slopes have the value $2D\zeta_s/\mathrm{k_B}T$. Data point shape indicates the diffusion constant: Round points: $D\zeta_s/\mathrm{k_B}T = 1$, Square points: $D\zeta_s/\mathrm{k_B}T = 1/2$, Diamond points: $D\zeta_s/\mathrm{k_B}T = 1/3$. . Simulation parameters: $N = 2000$, $Z = 5$, simulation timestep $\Delta t = 1.56(10^{-9})t_e$.

The early time diffusion behavior shown in Figure 4.8 indicates that the expected short time diffusion dynamics (Equation 4.14) are obtained in simulation. Because this early time diffusion behavior depends only on the simulation diffusion constant parameter, it is independent of the total polymer length, or the number of slip-links present (the short time diffusion is purely local). This can be verified by comparing the early time diffusion behavior of pseudo-ring polymers with identical local diffusion constants $\mathrm{k_B}T/\zeta_s$ but different total lengths:

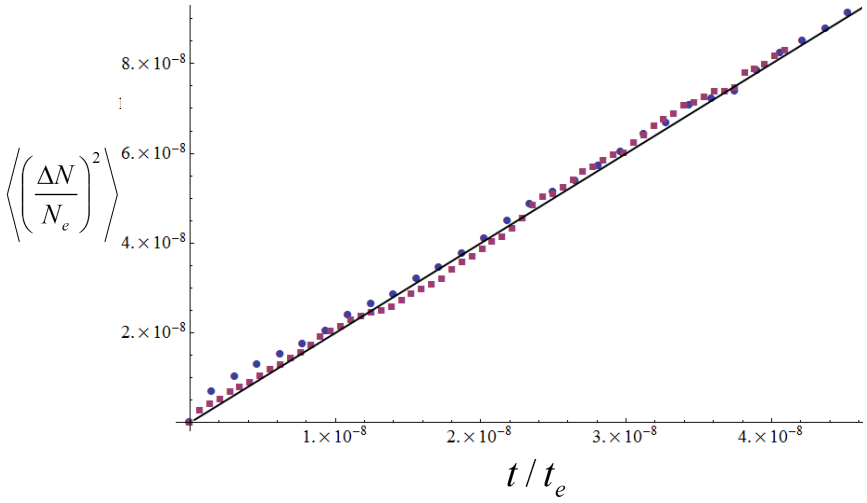

Figure 4.9: Early time mean square polymer diffusion across a slip-link vs. time for a pseudo-ring polymer for two different length polymers with the same diffusion constants $D = \mathrm{k_B}T/\zeta_s$. Data point shape indicates the total polymer contour length: Round points: $N = 2000$, Square points: $N = 3000$. The line is the expected behavior Equation 4.14 with slope $2D\zeta_s/\mathrm{k_B}T = 2$. Number of slip-links constant at $Z = 5$. Simulation timestep: Round points: $\Delta t = 1.56(10^{-9})t_e$, Square points: $\Delta t = 6.94(10^{-10})t_e$.

As can be seen in Figure 4.9 the early time arc-length diffusion is unaffected by total polymer length; short time diffusion is purely local and depends only on the local diffusion constant.

In the long time regime $\langle \Delta N^2 \rangle$ is also linear with time, and the slope is reduced from the short time diffusion case by a factor of the number of slip-links on the polymer Z. In the long time diffusion case the effective diffusion constant becomes $\mathrm{k_B}T/(Z\zeta_s)$. This diffusion is what is expected for total polymer collective diffusion across Z slip-links; a drag coefficient of ζ_s is associated with each slip-link, and thus total polymer collective diffusion has an effective drag coefficient of $Z\zeta_s$. Intuitively speaking, in the long time regime diffusion is dominated by the collective motion of

the polymer (or of the slip-links in arc-length space), and in such a case the diffusion constant depends on the total polymer drag (or the total drag of the collection of all slip-links in arc-length space).

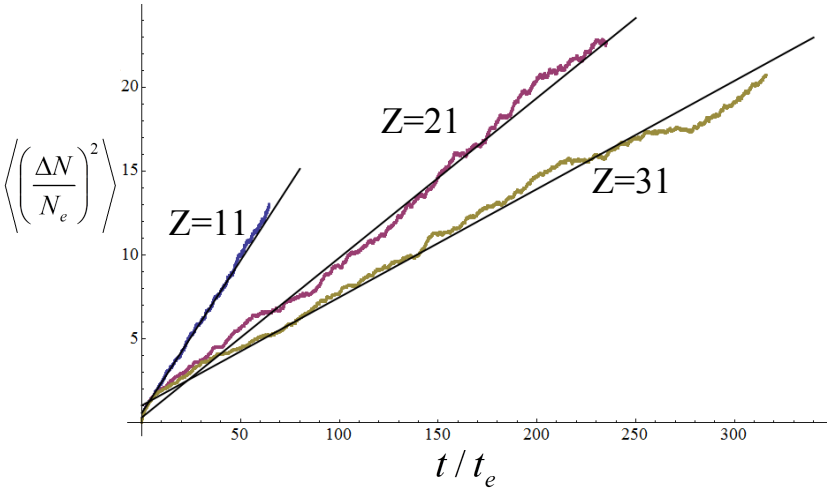

Figure 4.10: Late time mean square polymer diffusion across a slip-link vs. time for pseudo-ring polymers with different numbers of slip-links Z. Labels indicate the number of slip-links Z on the pseudo-ring polymer: $Z = 11$, $Z = 21$, and $Z = 31$. The points are simulation data while the lines show the expected behavior; in this plot the predicted slopes have the value $2/Z$. Simulation parameters: $N = 75$, simulation timesteps in order of increasing Z: $\Delta t = 5.38(10^{-6})t_e$, $\Delta t = 1.96(10^{-5})t_e$, $\Delta t = 4.27(10^{-5})t_e$.

In Figure 4.10 the agreement between the slopes of the displayed lines and diffusion data indicates that the long time arc-length diffusion on a pseudo-ring polymer has the expected effective diffusion constant of $\mathrm{k_B}T/(Z\zeta_s)$. This indicates that long time arc-length diffusion is dominated by the collective diffusion of the entire polymer, for which the effective drag constant is $Z\zeta_s$, the sum of the drag constants for all slip-links.

Between the short and long time linear diffusion regimes there exists a sub-diffusive

regime in which diffusion across each individual slip-link is no longer independent, but the total polymer collective diffusion mode is not yet completely dominant. In this regime $\langle \Delta N^2 \rangle \sim \sqrt{t}$. The presence of such a sub-diffusion regime is a characteristic of one dimensional diffusion systems, particularly so-called "single file" systems involving the one dimensional diffusion of particles that cannot pass each other [161–165]. Since the slip-links here behave as a type of non-passing particle in the space of arc-length this model maps to such a single file description.

4.3.1 Pseudo-Ring Stochastic Analysis

The arc-length diffusion in the pseudo-ring toy model can be studied via stochastic analysis. The goal of such analysis is to obtain mathematical expressions that would describe the diffusion behavior over all time regimes. In order to do so a stochastic equation designed to accurately describe the polymer arc-length diffusion modes is constructed.

In order to construct a tractable stochastic equation some approximations are required. To begin, consider a very long pseudo-ring polymer with many slip-links ($N \gg 1$ and $Z \gg 1$) in equilibrium at temperature T. Consider one strand between slip-links, with the influence of the rest of the polymer treated as a "chemical potential bath" μ_s conjugate to arc-length (ie. one polymer strand in grand canonical ensemble with respect to arc-length). It was previously mentioned that, when considering arc-length diffusion (or a fixed number of slip-links), the chosen model configuration distribution (Equation 4.4) is equivalent to taking each polymer strand as having a free energy as given by Equation 4.22. Consequently, when considering arc-length diffusion around a pseudo-ring polymer this is taken to be the fundamental strand free energy. The rest of the polymer is treated as being at chemical potential μ_s. In the manner of grand canonical ensemble the effective strand system free energy then

becomes:

$$\frac{F_s}{\mathrm{k_B}T} = \frac{3\vec{Q}_s^2}{2N_s b^2} - \frac{3}{2}\ln\left[\frac{3}{2N_s}\right] - \frac{\mu_s}{\mathrm{k_B}T}N_s \tag{4.30}$$

This can be used to calculate the average strand arc-length:

$$\langle N_s\rangle = A\int_0^N dN_s N_s \left(\frac{3}{2N_s}\right)^{3/2} \exp\left[-\frac{3\vec{Q}_s^2}{2N_s b^2} + \frac{\mu_s}{\mathrm{k_B}T}N_s\right] \tag{4.31}$$

Here A is a normalization constant. Because a very long polymer is being considered the upper limit of the integral is taken to be infinite ($N \to \infty$), which gives $A = (2\pi b^2/3\vec{Q}_s^2)\exp[\sqrt{6\mu_s/\mathrm{k_B}T}\,|\vec{Q}_s|/b]$, and gives the average strand length as:

$$\langle N_s\rangle = \frac{|\vec{Q}_s|}{b}\sqrt{\frac{3\mathrm{k_B}T}{-2\mu_s}} \tag{4.32}$$

This can be inverted for an expression of the polymer chemical potential in terms of the average strand length. Additionally, the approximation is made that the polymer strand length is sharply peaked about its average (a macroscopic "hydrodynamic" approximation) so that $\langle N_s\rangle$ can now be treated as a macroscopic variable for strand length which I shall just denote as N_s. Furthermore, the approximation is now made that $\vec{Q}_s^2$ is sharply peaked (fixed) at the polymer strand average random walk value of $\frac{N}{Z}b^2$. Altogether this then gives an approximate expression for the polymer chemical potential in terms of the strand length:

$$\mu_s = -\frac{N}{Z}\frac{3\mathrm{k_B}T}{2N_s^2} \tag{4.33}$$

Now considering fluctuations about the average chemical potential value, since N_s is considered to be sharply peaked about its average value (N/Z) it may be expanded about this average value. In this representation the polymer chemical potential may

be approximated as:

$$\mu_s = -\frac{3\mathrm{k_B}T}{2}\frac{Z}{N} + 3\mathrm{k_B}T\left(\frac{Z}{N}\right)^2\left(N_s - \frac{N}{Z}\right) \tag{4.34}$$

The polymer is composed of strands, and so now it is considered that this expression can be treated as the chemical potential of a polymer strand of arc-length N_s in the regime where polymer strands are long with length strongly peaked about the average value (a macroscopic "hydrodynamic" regime). In such a case the strand arc-length can be expressed as the difference in the arc-length coordinates of the bordering slip-links $N_s = n_{j+1} - n_j$.

Using this expression for strand chemical potential it is possible to consider the chemical potential difference $\Delta\mu_j$ across the slip-link labeled j:

$$\Delta\mu_j = 3\mathrm{k_B}T\left(\frac{Z}{N}\right)^2((n_{j+1} - n_j) - (n_j - n_{j-1})) \tag{4.35}$$

Here the chemical potential difference expression is given in terms of the slip-link arc-length coordinates. The chemical potential across the slip-link will give rise to an average flow of arc-length (arc-length per time) equal to $-(\mathrm{k_B}T/\zeta_s)\Delta\mu_j$. A flow of arc length in the negative direction could be treated as a displacement of the slip-link in the positive arc-length direction so that $dn_j = (\mathrm{k_B}T/\zeta_s)\Delta\mu_j dt$. This flow relation can be used to create a stochastic (Langevin) equation for the coordinates of the slip-links on the pseudo-ring polymer. In doing this the slip-link index j is treated as continuous to give the equation a differential form:

$$dn_j = \frac{3\mathrm{k_B}T}{\zeta_s}\left(\frac{Z}{N}\right)^2\frac{\partial^2 n_j}{\partial j^2}dt + \sqrt{\frac{2\mathrm{k_B}T}{\zeta_s}}\eta(j,t)dt \tag{4.36}$$

Where here $\eta(j,t)dt$ is a thermal stochastic force term and $\eta(j,t)dt$ is known as

the differential Wiener measure. The term involving the random force conveys the influence of thermal fluctuations. The random force term has the properties:

$$\langle \eta(j,t)\eta(j',t')\rangle = \delta(j-j')\delta(t-t') \tag{4.37}$$

$$\langle \eta(j,t)\rangle = 0 \tag{4.38}$$

Equation 4.36 may be re-expressed as:

$$\frac{\partial n(j,t)}{\partial t} = \frac{3\mathrm{k_B}T}{\zeta_s}\left(\frac{Z}{N}\right)^2 \frac{\partial^2 n(j,t)}{\partial j^2} + \sqrt{\frac{2\mathrm{k_B}T}{\zeta_s}}\eta(j,t) \tag{4.39}$$

It is possible to use this stochastic equation to derive solutions for the diffusion mode behavior of the pseudo-ring polymer. In order to find the average behavior of $n(j,t)$ over the strand index interval $0 < j < Z$ consider the complex Fourier representation:

$$n(j,t) = \sum_{p=-\infty}^{\infty} \tilde{n}(p,t)\exp\left[\frac{2\pi p i}{Z}j\right] \tag{4.40}$$

Where p is an integer and $\tilde{n}(p,t)$ is given by:

$$\tilde{n}(p,t) = \frac{1}{Z}\int_0^Z dj\, n(j,t)\exp\left[-\frac{2\pi p i}{Z}j\right] \tag{4.41}$$

Here the Fourier representation is given in a discrete spectrum over the finite range $0 < j < Z$, and as such the Fourier representation is already periodic with period N and is a suitable representation of the polymer ring. In exact analogy the random force can be represented as:

$$\eta(j,t) = \sum_{p=-\infty}^{\infty} \tilde{\eta}(p,t)\exp\left[\frac{2\pi p i}{Z}j\right] \tag{4.42}$$

The $\tilde{\eta}(p,t)$ functions are independent, and calculating the moments gives:

$$\langle \tilde{\eta}(p,t) \rangle = 0 \tag{4.43}$$

For $p = 0$:

$$\langle \tilde{\eta}(0,t)\tilde{\eta}(p',t') \rangle = \frac{1}{Z}\delta(t-t')\delta_{0,p'} \tag{4.44}$$

For $|p| \geq 1$:

$$\langle \tilde{\eta}(p,t)\tilde{\eta}(p',t') \rangle = \frac{1}{Z}\delta(t-t')\delta_{-p,p'} \tag{4.45}$$

Using Equations 4.40 and 4.42 in Equation 4.39 and comparing like Fourier terms leads to the relations:

For $p = 0$:

$$\frac{\partial \tilde{n}(0,t)}{\partial t} = \sqrt{\frac{2\mathrm{k_B}T}{\zeta_s}}\tilde{\eta}(0,t) \tag{4.46}$$

For $|p| \geq 1$:

$$\frac{\partial \tilde{n}(p,t)}{\partial t} = \frac{3\mathrm{k_B}T}{\zeta_s}\left(\frac{Z}{N}\right)^2\left(\frac{2\pi p}{Z}\right)^2\tilde{n}(p,t) + \sqrt{\frac{2\mathrm{k_B}T}{\zeta_s}}\tilde{\eta}(p,t) \tag{4.47}$$

Calculating the diffusion behavior of the $p = 0$ term:

$$\left\langle (\tilde{n}(0,t) - \tilde{n}(0,0))^2 \right\rangle = \frac{2\mathrm{k_B}T}{\zeta_s}\int_0^t dt' \int_0^t dt'' \langle \tilde{\eta}(0,t')\tilde{\eta}(0,t'') \rangle \tag{4.48}$$

$$\left\langle (\tilde{n}(0,t) - \tilde{n}(0,0))^2 \right\rangle = 2\frac{\mathrm{k_B}T}{Z\zeta_s}t \tag{4.49}$$

So the diffusion coefficient of the $p = 0$ Fourier mode is given by $D = \mathrm{k_B}T/(Z\zeta_s)$.

Calculating the average behavior of the higher modes is now possible (the method

is analogous to the analysis of the Rouse model in [36]). Defining t_p as:

$$t_p \equiv \frac{\zeta_s}{3\mathrm{k_B}T}\left(\frac{N}{2\pi p}\right)^2 \tag{4.50}$$

The time auto-correlation function for the p,$-p$ mode pair (a composite of the both existing sine and cosine modes) yields:

$$\langle \tilde{n}(p,t)\tilde{n}(-p,0)\rangle = \frac{\mathrm{k_B}Tt_p}{Z\zeta_s}\exp\left[-t/t_p\right] \tag{4.51}$$

Since the $p = 0$ mode corresponds to the average position of all slip-links the slip-link average diffusion behavior has already been calculated in Equation 4.49. The results for the Fourier mode behavior can further be used to determine the ensemble average diffusion behavior of individual slip-links in the ring system. Using the Fourier representation in Equation 4.40 the average square of slip-link displacement can be expressed as:

$$\left\langle (n(j,t)-n(j,0))^2\right\rangle = \left\langle \left(\sum_{p=-\infty}^{\infty}\tilde{n}(p,t)\exp\left[\frac{2\pi pi}{Z}j\right] - \sum_{p=-\infty}^{\infty}\tilde{n}(p,0)\exp\left[\frac{2\pi pi}{Z}j\right]\right)^2\right\rangle \tag{4.52}$$

Computing the right side of the above equation involves treating many terms of the form $\langle \tilde{n}(p,t)\tilde{n}(p',0)\rangle$. However, only the terms with $p = -p'$ will have a non-zero average. The non-zero terms will have values as shown in Equation 4.51. Expanding

the right side of the equation and keeping only the non-zero terms results in:

$$\begin{aligned}\left\langle (n(j,t)-n(j,0))^2 \right\rangle = -4\sum_{p=1}^{\infty}\langle\tilde{n}(p,t)\tilde{n}(-p,0)\rangle \\ + 2\sum_{p=1}^{\infty}\langle\tilde{n}(p,t)\tilde{n}(-p,t)\rangle + 2\sum_{p=1}^{\infty}\langle\tilde{n}(p,0)\tilde{n}(-p,0)\rangle \\ + \langle\tilde{n}(0,t)^2\rangle + \langle\tilde{n}(0,0)^2\rangle - 2\langle\tilde{n}(0,t)\tilde{n}(0,0)\rangle \end{aligned} \quad (4.53)$$

The term on the first line of Equation 4.53 can be calculated using Equation 4.51:

$$-4\sum_{p=1}^{\infty}\langle\tilde{n}(p,t)\tilde{n}(-p,0)\rangle = -4\frac{k_B T}{Z\zeta_s}\sum_{p=0}^{\infty} t_p \exp[-t/t_p] \quad (4.54)$$

The second line of Equation 4.53 can be calculated in the same manner:

$$2\sum_{p=1}^{\infty}\langle\tilde{n}(p,t)\tilde{n}(-p,t)\rangle + 2\sum_{p=1}^{\infty}\langle\tilde{n}(p,0)\tilde{n}(-p,0)\rangle = 4\frac{k_B T}{Z\zeta_s}\sum_{p=1}^{\infty} t_p \quad (4.55)$$

The last line of Equation 4.53 can be re-expressed as:

$$\langle\tilde{n}(0,t)^2\rangle + \langle\tilde{n}(0,0)^2\rangle - 2\langle\tilde{n}(0,t)\tilde{n}(0,0)\rangle = \langle(\tilde{n}(j,t)-\tilde{n}(j,0))^2\rangle \quad (4.56)$$

This last quantity corresponds to the $p = 0$ mode diffusion behavior and has already been calculated in Equation 4.49.

Collecting all terms the ensemble average squared displacement of an individual slip-link is given by:

$$\left\langle (n(j,t)-n(j,0))^2 \right\rangle = \frac{2k_B T}{Z\zeta_s}t + \frac{4k_B T}{Z\zeta_s}\sum_{p=1}^{\infty} t_p\left(1-\exp[-t/t_p]\right) \quad (4.57)$$

With the values of t_p this becomes:

$$\left\langle (n(j,t) - n(j,0))^2 \right\rangle = \frac{2\mathrm{k_B}T}{Z\zeta_s}t + \frac{N^2}{3\pi^2 Z}\sum_{p=1}^{\infty} p^{-2}\left(1 - \exp\left[-\frac{12\pi^2 \mathrm{k_B}T p^2 t}{N^2\zeta_s}\right]\right) \quad (4.58)$$

In actuality because the slip-links are discrete objects and finite in number there will not be an infinite number of Fourier modes to sum over. The shortest wavelength Fourier mode for the slip-link system will correspond to the case where one Fourier wavelength takes place across three slip-links. This makes the total number of Fourier modes equal to $\frac{Z-1}{2}$ (here assuming an odd Z).

The short time behavior is obtained by expanding Equation 4.57 about time zero and keeping only the linear terms which yields:

$$\left\langle (n(j,t) - n(j,0))^2 \right\rangle = \frac{2\mathrm{k_B}T}{Z\zeta_s}t - \frac{4\mathrm{k_B}T}{Z\zeta_s}\sum_{p=1}^{\frac{Z-1}{2}} t \quad (4.59)$$

$$\left\langle (n(j,t) - n(j,0))^2 \right\rangle = \frac{2\mathrm{k_B}T}{Z\zeta_s}t - \frac{4\mathrm{k_B}T}{Z\zeta_s}\frac{Z-1}{2}t \quad (4.60)$$

$$\left\langle (n(j,t) - n(j,0))^2 \right\rangle = \frac{2\mathrm{k_B}T}{\zeta_s}t \quad (4.61)$$

This diffusion rate for a single slip-link at early times agrees with simulation results; the diffusion constant in this time regime is $D = \mathrm{k_B}T/\zeta_s$.

At long times Equation 4.58 becomes approximately:

$$\left\langle (n(j,t) - n(j,0))^2 \right\rangle = \frac{2\mathrm{k_B}T}{Z\zeta_s}t + \frac{N^2}{3\pi^2 Z}\sum_{p=1}^{\frac{Z-1}{2}} p^{-2} \quad (4.62)$$

For large values of Z the sum in the above equation can be very well approximated by making the limit infinite (for $Z = 100$ the difference is less than two percent) so I

make this approximation to obtain the analytic result:

$$\left\langle (n(j,t) - n(j,0))^2 \right\rangle = \frac{2\mathrm{k_B}T}{Z\zeta_s}t + \frac{N^2}{18Z} \tag{4.63}$$

This result indicates that in terms of diffusion rates the diffusion constant at long times is the short time diffusion constant multiplied by a factor of Z^{-1}; at long times the diffusion constant is $D = \mathrm{k_B}T/(Z\zeta_s)$.

In order to obtain an analytic result for intermediate time diffusion behavior the sum in Equation 4.58 is replaced with an integral according to the Euler integral approximation:

$$\int_0^n dx f(x) \approx \frac{f(0)}{2} + f(1) + f(2) + ... + \frac{f(n)}{2} \tag{4.64}$$

Where here n is an integer. Since the sum in Equation 4.58 lacks the zeroth term the value of the zeroth term must be determined to make the approximation. Expanding the summation function about $p = 0$ and yields the leading term $\frac{4\mathrm{k_B}T}{Z\zeta}t$. The integral approximation takes half the value of the zeroth term, which in this case is conveniently supplied by the leading term in Equation 4.58 corresponding to average total diffusion. Thus all of Equation 4.58 can be approximated as:

$$\left\langle (n(j,t) - n(j,0))^2 \right\rangle = \frac{N^2}{3\pi^2 Z}\int_0^\infty dp\, p^{-2}\left(1 - \exp\left[-\frac{12\pi^2\mathrm{k_B}Tp^2t}{N^2\zeta_s}\right]\right) \tag{4.65}$$

Here again the large Z approximation is used to set the upper limit of the integral to infinity. Doing the integral gives:

$$\left\langle (n(j,t) - n(j,0))^2 \right\rangle = \frac{2}{\sqrt{3\pi}}\frac{N}{Z}\sqrt{\frac{\mathrm{k_B}T}{\zeta_s}}\sqrt{t} \tag{4.66}$$

So at intermediate times the mean square slip-link displacement is expected to be

proportional to $\sqrt{t}$ (subdiffusive).

The full solution for the pseudo-ring diffusion given in Equation 4.58 is shown compared to pseudo-ring diffusion data below:

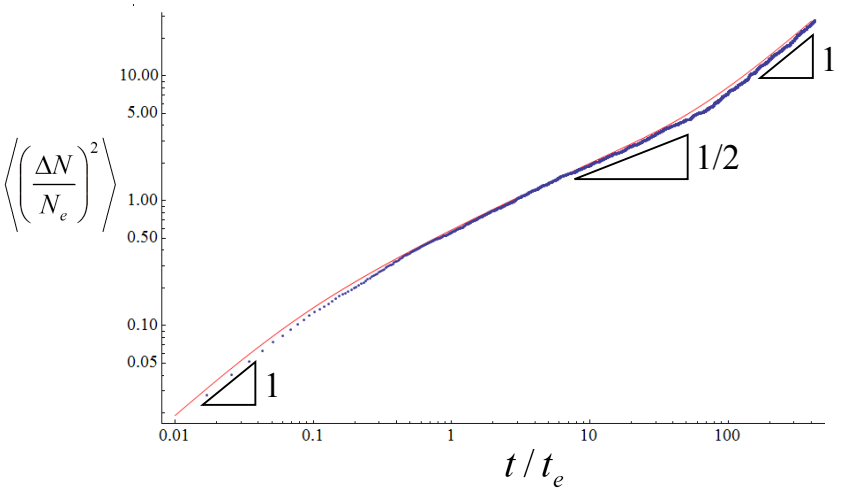

Figure 4.11: Mean square polymer diffusion across a slip-link vs. time for a pseudo-ring polymer. Both axes in logarithmic scale. Points are simulation data, line is the prediction from Equation 4.58. Number of slip-links fixed at $Z = 31$. Slopes indicating power law scaling in different regimes are indicated. Simulation parameters: $N = 75$, simulation timestep $\Delta t = 4.27(10^{-5})t_e$.

Figure 4.11 shows good agreement between the diffusion predicted from the stochastic equation, and the simulated pseudo-ring polymer diffusion. The expected power law scaling at early and late times ($\langle \Delta N^2 \rangle \propto t$) is obtained, and an approximately subdiffusive regime is found for intermediate times ($\langle \Delta N \rangle \propto t^{1/2}$). The subdiffusive time power is slightly greater than the expected value of 1/2, but this appears to be due to crossover effects caused by the early and late time regimes being not quite separated enough (with these simulation parameters) to obtain a full subdiffusive regime.

The approximations made in generating the pseudo-ring diffusion prediction equation should be expected to introduce some error between the prediction and the simulated diffusion. The prediction is expected to be more accurate in the long-time regime when the collective diffusion modes tend to dominate. As can be seen from Figure 4.11, the predicted diffusion is surprisingly close to the simulated diffusion in all sampled time regimes. Perhaps this is not especially surprising: by construction the predicted diffusion has the correct diffusion constant (slope) at very short and very long times (at short times it is diffusion across a single slip-link, while at long times collective total polymer diffusion dominates). Additionally, the constructed solution includes an intermediate time sub-diffusive regime as expected for any one-dimensional single file system. Given these constraints on the predicted diffusion solution fair agreement between the prediction and the simulated diffusion should perhaps be expected.

4.4 Model Rheology

Slip-link simulation models of entangled polymers have been successful in reproducing some realistic rheological responses [153, 154]. The basic polymer slip-link simulation described in this chapter reproduces a number of realistic rheological (stress/flow response) properties of polymer melts. For example, when subject to a small step shear strain, melts of linear entangled polymers in general exhibit a stress relaxation that is exponential at long times. A step shear strain deformation is illustrated in Figure 4.12 below.

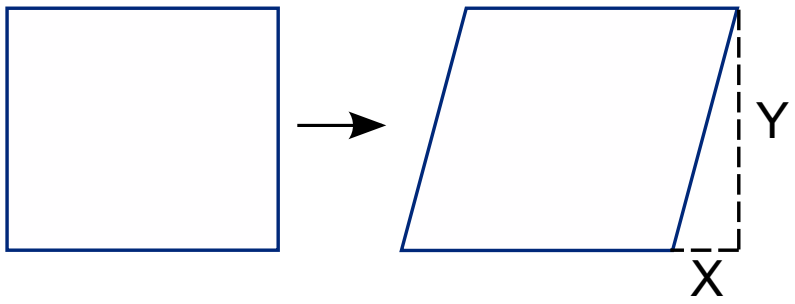

Figure 4.12: Illustration of a step shear strain deformation of a polymer melt. The value of the strain γ_{yx} is the ratio of the $\hat{x}$ direction displacement to the $\hat{y}$ direction extension; $\gamma_{yx} \equiv x/y$ (the tangent of the upper angle of the xy triangle).

In polymer melt experiments the induced stress following a small step strain ($\gamma_{yx} \ll 1$) exhibits a sudden decrease followed by an exponential decay. This stress behavior was tested for the simulation model by subjecting simulated polymers to a small step shear strain of $\gamma_{yx} = 0.1$. The simulated stress response is shown below.

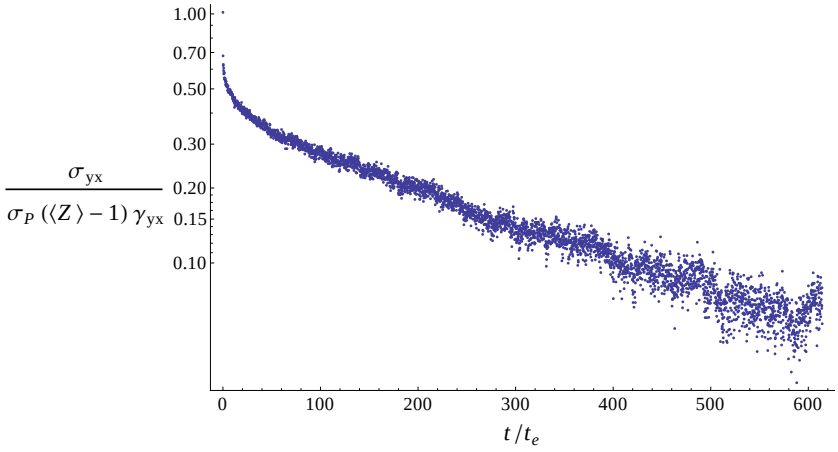

Figure 4.13: Stress relaxation vs. time following a small step shear strain of the simulated melt. Applied step strain was $\gamma_{yx} = 0.1$. Vertical axis in logarithmic scale. The stress relaxation is exponential at long times. The stress is expressed in ratio to $\sigma_P \equiv \mathrm{k_B} T \rho_P$, where ρ_P is the polymer density (polymers per volume). More densely packed polymers result in a larger stress response. Simulation parameters: $N = 110$, $\beta = 3.125$, simulation timestep $\Delta t = 2.56(10^{-5})t_e$.

The simulated stress decay is exponential at long times as expected. In addition to the exponential stress decay at long times the more rapid initial stress decay is also expected at short times, and is associated with fast "retraction" of the polymer ends following a step strain, during which some stress is quickly released as some polymer end constraints are quickly vacated.

In Figure 4.13 it can be seen that the average melt stress immediately following the step strain is equal to $\sigma_P(\langle Z\rangle - 1)\gamma_{yx}$. γ_{yx} is the value of the imposed shear strain (the ratio of displacement along the $\hat{x}$ direction relative to distance along the $\hat{y}$ direction). σ_P is the characteristic stress for a homopolymer melt simulation and is defined as $\sigma_P \equiv \mathrm{k_B}T\rho_P$, where ρ_P is the polymer density (polymers per volume). $\langle Z\rangle$ is the average number of slip-links per polymer. This initial stress value is what is expected for a polymer composed of Gaussian strands, and is predicted through the following argument.

For a single Gaussian strand between slip-links, the force on one strand end in the $\hat{x}$ direction is $f_x = \frac{\mathrm{k_B}T}{N_s b^2}Q_x$ (from Equation 4.1). Considering a rectangular polymer melt of one polymer species subject to a shear strain γ_{yx}, the stress (force per area) contribution from one single polymer strand across a plane drawn arbitrarily through the melt perpendicular to the $\hat{y}$ direction is:

$$\sigma_{yx}^{(s)} = \frac{1}{A_y}\frac{Q_y}{L_y}\frac{3\mathrm{k_B}T}{N_s b^2}Q_x = \frac{1}{\mathcal{V}_m}\frac{3\mathrm{k_B}T}{N_s b^2}Q_x Q_y \tag{4.67}$$

In Equation 4.67 A_y is the melt area perpendicular to the $\hat{y}$ direction, L_y is the length of the rectangular melt in the $\hat{y}$ direction, and $\mathcal{V}_m$ is the total melt volume $\mathcal{V}_m = A_y L_y$. In the first representation in Equation 4.67 the factor Q_y/L_y is a representation of the probability that the single strand will cross the arbitrarily drawn plane; in equilibrium in a homopolymer melt the polymer strands will be equally likely to be at any location, and so the probability that a single strand will cross any plane drawn perpendicular

to $\hat{y}$ is just the ratio of the polymer extension in the $\hat{y}$ direction $|Q_y|$ to the melt length in this direction L_y. In Equation 4.67 both Q_x and Q_y could be either positive or negative, and both are defined relative to the same strand end. The signs of Q_x and Q_y together correctly determine the sign of the stress contribution, which depends on the relative positions of the strand ends in both the $\hat{x}$ direction and the $\hat{y}$ direction (which strand end is "above" or "below" the considered plane).

The stress contribution for a single Gaussian strand given in Equation 4.67 depends on Q_x and Q_y, which are independent, and equally likely to be positive or negative when in equilibrium. Consequently the average stress contribution for a single polymer strand in equilibrium is $\langle \sigma_{yx}^{(s)} \rangle = 0$. However, following a step strain the strand configuration is perturbed and the stress contribution becomes non-zero. If a step strain γ_{yx} is applied the value of Q_x will be altered according to $Q'_x = Q_x + \gamma_{yx} Q_y$. Consequently, following a step shear strain of γ_{yx} the stress contribution from a single Gaussian polymer strand will be given by:

$$\sigma_{yx}^{(s)} = \frac{1}{\mathcal{V}_m} \frac{3 \mathrm{k_B} T}{N_s b^2} \left(Q_x Q_y + \gamma_{yx} Q_y^2 \right) \tag{4.68}$$

In equilibrium the average square end-to-end distance of a polymer strand modeled as a Gaussian filament will obey random walk statistics with $\langle \vec{Q}_s^2 \rangle = N_s b^2$. Consequently, the single squared directional component of strand end-to-end distance Q_y^2 in Equation 4.68 will average to $\langle Q_y^2 \rangle = N_s b^2 / 3$, while the term containing $Q_x Q_y$ will average to zero. This means the average stress contribution for a single Gaussian strand following a step strain deformation will be given by:

$$\langle \sigma_{yx}^{(s)} \rangle = \frac{\mathrm{k_B} T}{\mathcal{V}_m} \gamma_{yx} \tag{4.69}$$

For an instantaneous step strain the induced average melt stress will be the sum of the

average induced stress in each Gaussian strand. In this model each polymer has $\langle Z \rangle$ average slip-links, giving each $\langle Z \rangle - 1$ Gaussian strands. Consequently, the expected stress induced by an instantaneous step shear strain is given by:

$$\begin{aligned} \langle \sigma_{yx} \rangle &= \mathrm{k_B} T \rho_P (\langle Z \rangle - 1) \gamma_{yx} \\ \langle \sigma_{yx} \rangle &= \sigma_P (\langle Z \rangle - 1) \gamma_{yx} \end{aligned} \tag{4.70}$$

For simulated polymers which are highly entangled ($N \gg \beta$) the average number of slip-links is very well approximated by $\langle Z \rangle \approx N/\beta$. As can be seen from the initial stress value in Figure 4.13, the simulation exhibits this expected stress following a step strain.

In tube theories of polymer melt dynamics [36] stress relaxation after a step strain takes place as polymers vacate the particular tube-like topological constraints confining them at the time of the strain application, and re-randomize their configurations. In these tube theories it is postulated that the stress remaining (relative to the equilibrium stress) after a step strain is proportional to the fraction of total polymer arc-length still residing in same topologically confining tube as at the time of strain application. The fraction of polymer arc-length residing in the original confining tube is analogous to the number of original slip-links remaining on a polymer in the slip-link entanglement model. In this model it is found that the fraction of original slip-links remaining in equilibrium after some time decays exponentially in a manner similar to the polymer stress relaxation following a small step shear strain. Thus this slip-link model is similar to the successful tube models of entangled polymers in that stress relaxation is largely governed by how quickly a polymer vacates its constraints.

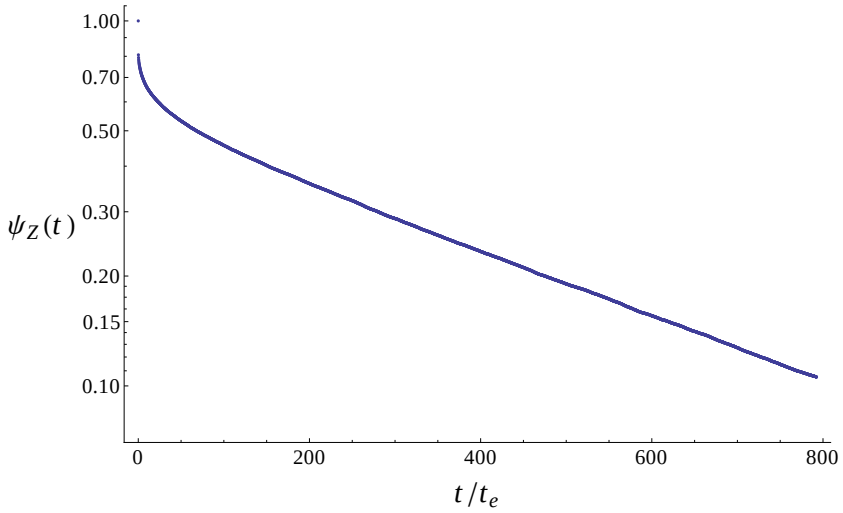

Figure 4.14: Fraction of original slip-links remaining ψ_Z vs. time, measured in equilibrium. Vertical axis in logarithmic scale. The number of original slip-links remaining decays exponentially at long times. Simulation parameters: $N = 70$, $\beta = 3.125$, simulation timestep $\Delta t = 2.56(10^{-5})t_e$.

The terminal relaxation times t_r for the stress decay following a small step shear strain, and the fraction of original slip-links remaining in equilibrium, were examined by fitting a function of the form $A\exp[-t/t_r]$ to the large time data regions for these quantities. The relaxation times t_r for different simulated polymer lengths N were found, and the scaling of t_r with respect to N is examined below.

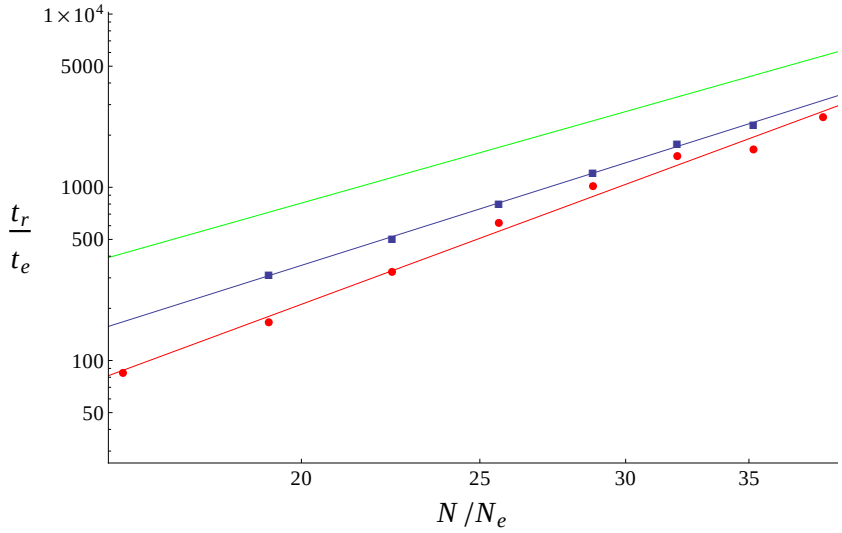

Figure 4.15: Relaxation time t_r vs. polymer length N in monomers from simulation. Both axes in logarithmic scale. The relaxation times t_r are from fitting functions of type $A\exp[-t/t_r]$ to the long time regions of stress relaxation and slip-links remaining data of the type in Figures 4.13 and 4.14. The t_r values with square markers are from fraction of slip-links remaining data; the fit gives $t_r/t_e = 1.49(10^{-2})(N/N_e)^{3.36}$. The t_r values with circular markers are from stress relaxation data following a step strain of $\gamma_{yx} = 0.1$; the fit gives $t_r/t_e = 1.61(10^{-3})(N/N_e)^{3.93}$. The upper line is the reptation time from the Doi-Edwards tube theory model [36]: $t_r/t_e = L^3/(\pi^2 a^3) = (N/N_e)^3/\pi^2 = 1.01(10^{-1})(N/N_e)^3$.

In Figure 4.15 the terminal relaxation times t_r for stress following a small step strain, and fraction of original slip-links remaining in equilibrium, are of similar magnitude and follow similar scaling laws with respect to the polymer length N. In the reptation picture of polymer relaxation, the characteristic relaxation time is the reptation time $t_{rep} \sim N^3$. If polymer melt relaxation was governed purely by the core mechanism of reptation, the relaxation times would scale like $t_r \sim N^3$. As can be seen from the power law fits to the data, for the fraction of original slip-links remaining $t_r \sim N^{3.36}$, and for the stress decay following a small step strain $t_r \sim N^{3.93}$. Consequently the data indicate that simple reptation might be a fair approximation for the polymer relaxation mechanism, but it does not capture the entirety of the relaxation process. This is in agreement with experiment, in which it has been found that

polymer melt stress following a small deformation decays exponentially at long times, with a relaxation time $t_r \sim N^{\alpha}$, with $\alpha \approx 3.4$ [40]. In some computer simulations of polymers that allow for polymer contour length fluctuations a similar relaxation time scaling has been reproduced [41]; the inclusion of contour length fluctuations has been found to increase the scaling exponent above the value of 3 obtained from the pure reptation picture. For this reason models including contour length fluctuations are thought to be more physically realistic. This simulation model includes contour length fluctuations, consequently it is a not a surprise that the relaxation times depend somewhat more strongly on the polymer length N than in the pure reptation picture.

The scaling of the relaxation times in Figure 4.15 can also be used as a check on the fractional decay hypothesis, that the fraction of induced stress remaining following a small deformation (in this case a step shear strain of $\gamma_{yx} = 0.1$) is governed by the fraction of original slip-links (entanglements) remaining over time as measured in equilibrium. For short polymer lengths the stress relaxation times are smaller than the relaxation times for the fraction of original slip-links remaining, however, the stress relaxation times increase more quickly with polymer length N (over the polymer lengths sampled stress relaxation gives $t_r/t_s \propto N^{3.93}$ while tracking the fraction of original slip-links gives $t_r/t_s \propto N^{3.36}$). For longer polymer lengths ($N \geq 90$) the stress and fractional slip-link relaxation times are close in value and appear to scale in approximately the same way. This indicates that for longer polymers the fractional decay hypothesis seems correct, while for shorter polymers (in this model those with $N < 90$) terminal stress decay appears to be somewhat faster than the terminal decay of the fractional loss of original slip-links.

In experiments performing startup shear deformations on polymer melts many polymer melts show a stress "overshoot", where the stress induced by the steady

shear peaks before settling into a steady state value. This stress overshoot peak is larger for larger applied shear rates. In polymer experiments the stress vs. strain relation during the rise to the overshoot peak has been found to have some universal characteristics [166]. A stress overshoot peak during startup shear is found in the simulation and is examined below.

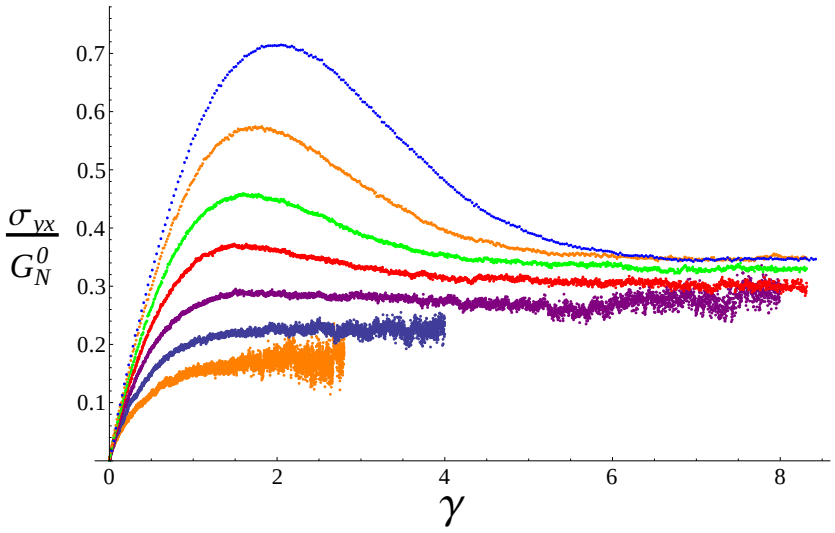

Figure 4.16: Melt stress vs. strain for a startup shear situation. Stress overshoot is larger for larger shear rates $\dot{\gamma}_{yx}$, and thus for larger Weissenberg numbers ($\mathrm{Wi} = \dot{\gamma}_{yx}\, t_{rep}$). Weissenberg numbers for applied shear rates: Wi = 0.4, Wi = 0.8, Wi = 1.6, Wi = 3.2, Wi = 6.4, Wi = 12.8, Wi = 25.6. Melt stress is expressed in ratio to the plateau modulus $G_N^0 = 4\mathrm{k_B}T/(5N_e\nu)$ [36], where ν is the monomer volume. The stress behavior shows an "overshoot". Simulation parameters: $N = 50$, $\beta = 3.125$, simulation timestep $\Delta t = 2.56(10^{-5})t_e$.

In polymer experiments the stress rise to the overshoot peak is found to be a universal function when plotted in ratio to the peak values [166]. That is, σ_{yx}/σ_{max} vs. γ/γ_{max} is found to be a universal function during the rise to the overshoot peak, where σ_{max} is the overshoot peak stress, and γ_{max} is the strain where the overshoot peak occurs. This quality is reproduced in the simulation as shown below.

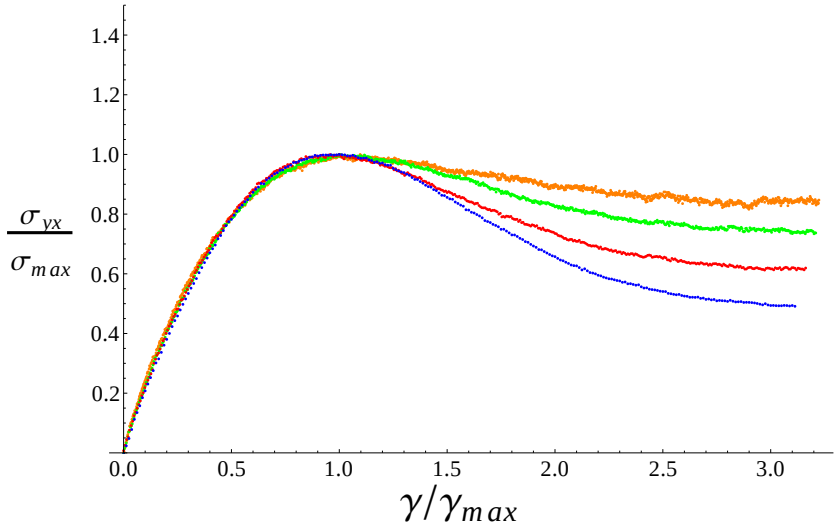

Figure 4.17: Melt stress vs. strain for a startup shear in bulk simulation. Stress and strain are plotted in ratio to the values at the overshoot peaks. Data shown for different applied shear rates corresponding to Weissenberg numbers: Wi = 3.2, Wi = 6.4, Wi = 12.8, Wi = 25.6. When plotted in this way the rise to the overshoot peak is found to be a universal function. Simulation parameters: $N = 50$, $\beta = 3.125$, simulation timestep $\Delta t = 2.56(10^{-5})t_e$.

It can be seen that the stress behavior of this simulation model exhibits some physically realistic properties, including a stress decay following a small step shear strain which is exponential at long times, physically realistic scaling of relaxation times with polymer length N, and universal stress overshoot behavior following shear startup.

4.5 Summary

This fundamental simulation model reproduces several response properties of polymer melts found to agree with experiment. For this reason slip-link models are popular tools for theoretical analysis of entangled polymers, and the simulation developed here is based on such a model in order to obtain a fast and physically realistic result.

The fundamental model treats a polymer as a Gaussian filament, and uses slip-links to describe polymer entanglements. In this model slip-links are evenly randomly distributed along the polymer contour in equilibrium. Though slip-link entanglements are meant to represent topological interactions between polymers, each simulated polymer is independent, and thus the slip-links serve as a way to simulate entangled polymers without having to consider complicated inter-polymer interactions.

The simulation consists of two Monte Carlo moves: an arc-length shuffle move which moves arc-length across a slip-link from one polymer strand to another, and a slip-link create/destroy move. The slip-link create/destroy move is restricted to creating and destroying slip-links in arc-length regions near the polymer ends. In this study the choice is made to have these arc-length regions be twice the average arc-length distance between entanglements, and such a choice means that the end slip-links are usually located in the create/destroy accessible regions. Restricting slip-link creation and destruction in this way makes the simulation model behave in a manner similar to successful tube models of polymer entanglement, in which tube segments are created and destroyed at polymer ends.

When applying a Monte Carlo move the decision of which of the two move types to use is made probabilistically using a user defined move probability ratio. Simulation convergence will occur regardless of the probability ratio (so long as both move types are used with finite relative probability), but efficient convergence and dynamics are found to occur in the simulated systems studied when the ratio of slip-link create/destroy moves to arc length shuffle moves is on the order of 5/100. This is a high enough fraction of slip-link create/destroy moves that the slip-links nearest to the polymer ends can be thought of as always being in a state of equilibrium (they are being quickly created and destroyed), and the observed dynamics at and above this fraction are insensitive to the specific value used for the move type probability

ratio.

The Monte Carlo moves are subject to acceptance probabilities that enforce detailed balance in equilibrium. These acceptance probabilities ensure that the model has the desired physically motivated equilibrium configuration probability distribution (Equation 4.4). This is verified by finding agreement between simulated physical quantities and the associated model predictions.

The simulation produces well understood and physically realistic dynamics, as verified through the pseudo-ring simulation performed to study polymer diffusion. Long time polymer diffusion is governed by the reptation process. The simulation also produces physically realistic rheology, as verified by comparing polymer stress responses in different situations to the stress responses expected from experiment or other well known polymer models. Long time polymer relaxation following a sharp deformation is exponential with time as expected. The characteristic stress relaxation times are near the reptation times predicted from polymer tube models, and follow the expected scaling for a polymer simulation which includes contour length fluctuations ($t_r \propto N^{\alpha}$, $\alpha \approx 3.4$). This slip-link polymer simulation has realistic and reliable physical properties, and is used as the basis for an extended simulation of polymer-polymer interfaces described in subsequent chapters.

Chapter 5

Simulating Polymer-Polymer Interfaces

In order to simulate polymers near a planar interface between immiscible polymer melts the polymer-polymer interface is described by a self-consistently determined chemical potential field $\omega(\vec{r})$ conjugate to polymer contour length. With this self-consistent chemical potential it is possible to calculate the modified polymer strand statistical weights, which are then used in a Monte Carlo slip-link simulation to sample configurations in a way which takes the influence of the interface into account. This chapter first describes the method of determining a self-consistent field description of a polymer-polymer interface. Discussion then moves on to describe how a self-consistently determined chemical potential can be used to calculate Gaussian polymer strand statistical weights (in this case strand Green functions). Finally, a description is given for how the strand Green functions can be used in the Monte Carlo slip-link simulation to calculate move acceptance probabilities such that the simulated polymer is brought to equilibrium in the chemical potential field describing the polymer-polymer interface.

5.1 Self-Consistent Field Interface Description

In the self-consistent field description of a polymer-polymer interface the free energy cost for having small polymer arc-length ΔN at position $\vec{r}$ is $\Delta N\omega(\vec{r})$. Here ω is a chemical potential field that represents the interaction of one polymer species with the other, and with incompressibility constraints. The chemical potential field is calculated numerically using the polymer self-consistent field theory developed by Flory and Huggins [48–50], Helfand and Tagami [51,52], and others. Because a planar interface between polymer melts is being considered, the chemical potential field is a function of only the direction perpendicular to the interfacial plane (y). The chemical potential field $\omega(\vec{r})$ used to describe the polymer-polymer interface is an expression of the average free energy interactions acting on a polymer section at a given space location, including both inter-species contact interactions and energy arising from pressure in the polymer melt (the melt is considered to be incompressible).

In the Flory-Huggins description of free energy interactions between fluids the interaction free energy cost ΔF_A for a species A polymer section of arc-length ΔN_A to be in contact with species B polymers at position $\vec{r}$ is:

$$\Delta F_A = \Delta N_A \mathrm{k_B} T \chi \, \phi_B(\vec{r}) \tag{5.1}$$

Here $\phi_B(\vec{r})$ is the volume fraction occupied by species B polymers at position $\vec{r}$; volume fraction is the local species density divided by the total density which is considered to be fixed (the melt is considered to be incompressible). ΔN_A is assumed short such that this small arc-length is located in a region about $\vec{r}$ where the species volume composition is constant. χ is an interaction strength parameter describing the degree of repulsion between the polymer species (large χ corresponds to a larger free energy penalty and larger repulsion). It can be seen from Equation 5.1 that

the chemical potential acting on a species A polymer due to interspecies repulsive interactions is $\mathrm{k_B}T\chi\,\phi_B(\vec{r})$. The parallel relation for ΔF_B also holds.

The total chemical potential acting on the polymer contour will also include a contribution from the pressure present in the polymer melt. Altogether the total chemical potential acting on species A polymers $\omega_A(\vec{r})$ and the total chemical potential on species B polymers $\omega_B(\vec{r})$ will be given by:

$$\begin{aligned} \omega_A(\vec{r}) &= \mathrm{k_B}T\chi\,\phi_B(\vec{r}) + \eta(\vec{r}) \\ \omega_B(\vec{r}) &= \mathrm{k_B}T\chi\,\phi_A(\vec{r}) + \eta(\vec{r}) \end{aligned} \tag{5.2}$$

In these equations $\eta(\vec{r})$ is the chemical potential arising from the pressure at position $\vec{r}$, which is the same for both polymers. Because the melts are considered to be incompressible the local polymer volume fractions must sum to unity:

$$\phi_A(\vec{r}) + \phi_B(\vec{r}) = 1 \tag{5.3}$$

It is possible to determine the polymer volume fraction profiles $\phi_\alpha(\vec{r})$ from a given chemical potential field using statistical weight functions calculated via a differential equation. The equations governing this process are presented below, and their derivation is discussed later in this chapter.

$$\phi_\alpha(\vec{r}) = \frac{1}{Q_\alpha(N)}\int_0^N q_\alpha(\vec{r};N_s)q_\alpha(\vec{r};N-N_s)dN_s \qquad Q_\alpha(N) = \int d\vec{r}\,q_\alpha(\vec{r};N) \tag{5.4}$$

$$\frac{\partial q_\alpha(\vec{r};N_s)}{\partial N_s} = \left(\frac{b^2}{6}\nabla^2 - \frac{\omega(\vec{r})}{\mathrm{k_B}T}\right)q_\alpha(\vec{r};N_s) \qquad\qquad q_\alpha(\vec{r};0) = 1 \tag{5.5}$$

Equations 5.4 and 5.5 arise from statistical considerations of a Gaussian filament in a chemical potential field, and are explained subsequently. Equations 5.3, 5.3, 5.4, and

5.5, together determine the volume fraction profiles $\phi_\alpha(\vec{r})$ and chemical potential fields $\omega_\alpha(\vec{r})$ (up to a constant) at a polymer-polymer interface. These equations may be solved self-consistently via an iterative numerical calculation. In brief, this chemical potential field is calculated numerically (after N, χ, and T have been specified) by making a guess as to the equilibrium volume fraction profile for each polymer species, and then iteratively adjusting these profiles until a "self-consistent" volume fraction profile is reached. The self-consistent volume fraction profile describes the average polymer spatial density at the chosen temperature for the chosen degree of polymer repulsion (χ). Calculation of the self-consistent chemical potentials used in this work was performed using a code named PSCF developed by Morse, Tyler, Ranjan, Qin, and Thiagarajan, in the Department of Chemical Engineering and Materials Science at the University of Minnesota. Further details regarding the numerical calculation of self-consistent field quantities are given in Appendix B.

Examples of a calculated self-consistent chemical potential field and volume fraction profile are shown below for a polymer melt existing between two planar interfaces with an immiscible species polymer melt:

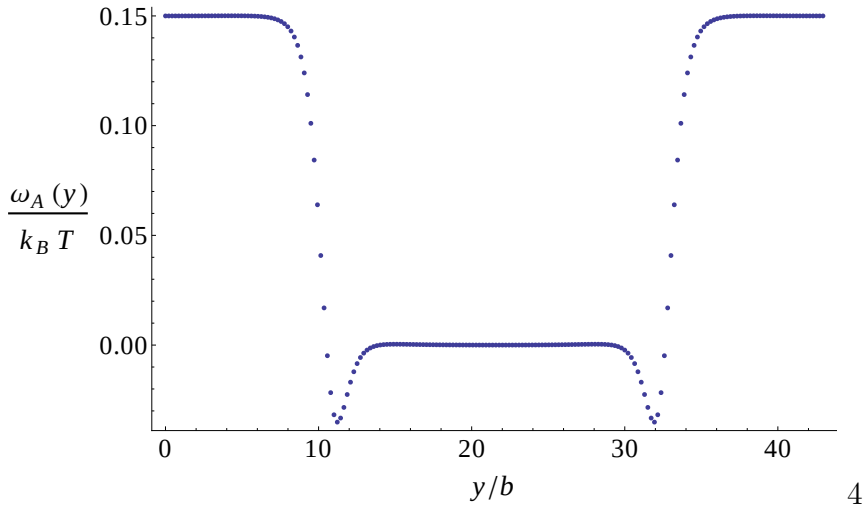

4

Figure 5.1: A chemical potential field profile determined via self-consistent field theory. This field is for a melt of species A polymers confined between two melts of species B polymers. The field confines polymers into a melt region where the field is lower. Polymers of another chemical species primarily occupy the high field region, and the field is the net result of repulsive interactions between the polymer species, and pressure interactions. The two melt species are considered symmetric (matching physical parameters) and incompressible. The calculation is done using periodic boundary conditions to simulate repeating polymer melt layers. This field was calculated for $\chi = 0.15$, $N = 80$.

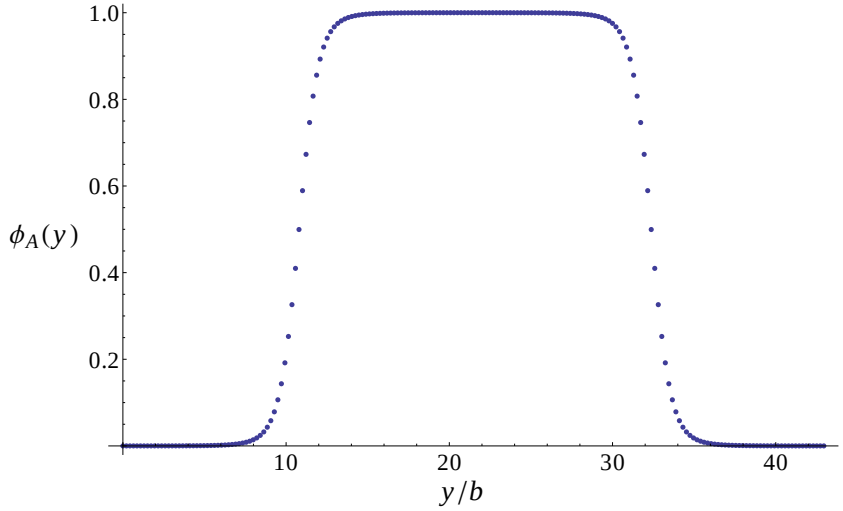

Figure 5.2: A polymer melt volume fraction profile calculated via self-consistent field theory. This volume fraction profile is for a melt of species A polymers confined between two melts of species B polymers. The density profile represents many polymers of a particular chemical species which are confined to a melt region by repulsive interactions with surrounding other-species polymers. The net confining repulsive and pressure interactions are summarized in the chemical potential field shown in Figure 5.1. In the central region the volume is nearly entirely occupied by the polymer species here shown. In the regions to the left and right where the volume fraction falls there is overlap between the two species polymer melts. This density profile is produced by the self-consistently determined chemical potential field shown in Figure 5.1 for a system with $\chi = 0.15$, $N = 80$.

5.2 Simulation In a Chemical Potential Field

The energy landscape near the polymer-polymer interface is described by a chemical potential field, and this field is used in simulation to inform the motion of the polymers. The chemical potential field alters the polymer configuration probability distribution, and consequently also alters the Monte Carlo move acceptance probabilities. Obtaining the physically correct Monte Carlo move acceptance probabilities is possible by examining the influence of the chemical potential field on polymer configuration probabilities. Specifically, the statistical weights associated with polymer

strands between slip-links may be calculated in the presence of the self-consistent chemical potential field describing the interface.

In the presence of a non-trivial chemical potential field the probability distribution for the locations of the ends of a polymer strand is no longer Gaussian as in Equation 4.2. The behavior of the polymer within a chemical potential field may be analyzed by considering an infinitesimal piece of polymer strand contour dn and the infinitesimal free energy dF that this piece of strand contour has in-field:

$$dF = \frac{3\mathrm{k_B}T}{2b^2}\left(\frac{\partial \vec{r}_n}{\partial n}\right)^2 dn + \omega(y)dn \tag{5.6}$$

The first term in Equation 5.6 corresponds to the stretching energy of the infinitesimal piece of Gaussian strand, while the second term corresponds to the free energy arising from interaction with the chemical potential field. Integration of Equation 5.6 down the total polymer contour length gives the energy of a Gaussian strand configuration in a chemical potential field. This free energy may be used to generate a statistical weight of any particular strand configuration. The statistical weight for a polymer strand of arc-length N_s and ends located at $\vec{r}$ and $\vec{r}'$, but otherwise unconstrained, is given by:

$$\Psi(\vec{r},\vec{r}';N_s) \equiv \int_{\vec{r}_0=\vec{r}}^{\vec{r}_{Ns}=\vec{r}'} \delta\vec{r}_n \exp\left[-\frac{3}{2b^2}\int_0^{N_s} dn \left(\frac{\partial \vec{r}_n}{\partial n}\right)^2 - \frac{1}{\mathrm{k_B}T}\int_0^{N_s} dn\, \omega(\vec{r}_n)\right] \tag{5.7}$$

Here the integral with respect to $\delta\vec{r}_n$ is over all possible strand configurations while keeping the strand ends fixed. The probability density $P(\vec{r},\vec{r}';N_s)$ for finding a polymer strand of contour length N_s with ends located within infinitesimal regions at $\vec{r}$ and $\vec{r}'$ is given by:

$$P(\vec{r},\vec{r}';N_s) = \frac{\Psi(\vec{r},\vec{r}';N_s)}{\int d\vec{r}\int d\vec{r}'\Psi(\vec{r},\vec{r}';N_s)} \tag{5.8}$$

The simulation is altered so that in the presence of a chemical potential field it correctly samples the configuration probabilities determined via the in-field strand statistical weights. In such a case the probability factors associated with polymer strands between slip-links are no longer simple Gaussian functions, but are instead proportional to the in-field strand statistical weights. In the simulation the Gaussian strand probability densities $P(\vec{r},\vec{r}';N_s)$ or statistical weights $\Psi(\vec{r},\vec{r}';N_s)$ are not used directly, but instead use the strand Green functions $G(\vec{r},\vec{r}';N_s)$. The Green function $G(\vec{r},\vec{r}';N_s)$ is proportional to the joint probability density $P(\vec{r},\vec{r}';N_s)$, but is differently normalized. The purpose of using the Green functions is that they may be easily calculated via a differential equation, and they may easily be used to define a new in-field polymer total configuration probability density in a consistent manner. The Green function $G(\vec{r},\vec{r}';N_s)$ is defined as:

$$G(\vec{r},\vec{r}';N_s) \equiv \frac{\Psi(\vec{r},\vec{r}';N_s)}{Q(N_s)} \tag{5.9}$$

$$Q(N_s) \equiv \int d\vec{r}' \int_{\vec{r}_0=\vec{r}}^{\vec{r}_{Ns}=\vec{r}'} \delta\vec{r}_n \exp\left[-\frac{3}{2b^2}\int_0^{N_s} dn \left(\frac{\partial\vec{r}_n}{\partial n}\right)^2\right] \tag{5.10}$$

The Green function definition involves normalization by the function $Q(N_s)$ (Equation 5.10). It should be noted that $Q(N_s)$ does not involve the chemical potential field, and is independent of spatial position (because $Q(N_s)$ does not involve the chemical potential field all spatial positions are alike).

In the presence of a chemical potential field the entangled polymer model is modified such that the equilibrium polymer configuration probability density is changed from Equation 4.4 to:

$$P(Z,\{\vec{r}_i\},\{N_i\}) = \frac{J_\omega}{\beta^{Z+1}}\left(\prod_{i=1}^{Z-1} G(\vec{r}_i,\vec{r}_{i+1};N_i)\right) q(\vec{r}_1;N_0)q(\vec{r}_Z;N_Z) \tag{5.11}$$

J_ω is a normalization constant. As can be seen, the product of simple Gaussian strand end location probability densities in Equation 4.4 has been replaced in Equation 5.11 by the product of in-field polymer strand Green functions $G(\vec{r}_i, \vec{r}_{i+1}; N_i)$. The additional factors of $q(\vec{r}_1; N_0)$ and $q(\vec{r}_Z; N_Z)$ are associated with the probability weights of the dangling end strands which are only constrained at one point. $q(\vec{r}; N_s)$ is defined by:

$$q(\vec{r}; N_s) \equiv \int d\vec{r}' G(\vec{r}, \vec{r}'; N_s) = \frac{\Psi(\vec{r}; N_s)}{Q(N_s)} \tag{5.12}$$

$$\Psi(\vec{r}; N_s) \equiv \int d\vec{r}' \Psi(\vec{r}, \vec{r}'; N_s) \tag{5.13}$$

Previous to considering an external chemical potential field the configuration probability distribution in Equation 4.4 contained no factors associated with the polymer end strands. This is because without a chemical potential field all space locations are alike and it is equally likely to find one end of an otherwise unconstrained polymer strand at any space location. This is not the case in the presence of a chemical potential field, and so the q functions become necessary in Equation 5.11.

In the configuration distribution given in Equation 5.11 the Green functions $G(\vec{r}, \vec{r}'; N_s)$ are proportional to the strand statistical weights $\Psi(\vec{r}, \vec{r}'; N_s)$ (Equation 5.7), and the q functions are proportional to the statistical weights for strands constrained at only one end $\Psi(\vec{r}; N_s)$. Thus the relative equilibrium probabilities of in-field polymer configurations are given by the ratios of the total in-field configuration statistical weights. There might arise the worry that the Green and q function definitions involve normalization by $Q(N_s)$ (Equation 5.10), and this normalization depends on the associated strand arc-length N_s. However, the Q functions have the property $Q(N_i)Q(N_j) = f(N_i + N_j)$. That is, the product of Q functions associated with polymer strands is a function depending on only the sum of the strand arc

lengths, which means the normalization of the product of the Green and q functions in Equation 5.11 depends only on the total polymer contour length and does not depend on the specific $\{N_i\}$ configuration. This property of the Q functions can be seen from the definition in Equation 5.10, which results in $Q(N_s) \sim \alpha^{N_s}$, with α being a constant.

Given the in-field configuration probability distribution in Equation 5.11 and its properties the ratio of configuration probabilities for any two configurations Ω_i and Ω_j is given by:

$$\frac{P(\Omega_i)}{P(\Omega_j)} = \beta^{Z_j - Z_i} \frac{\Psi(\Omega_i)}{\Psi(\Omega_j)} \tag{5.14}$$

Here $\Psi(\Omega)$ is the product of all statistical weights (Equation 5.7) associated with the Green and q functions (Equations 5.9 and 5.12) for a particular configuration probability in Equation 5.11.

The form of the in-field configuration distribution in Equation 5.11 preserves the property that all equilibrium polymer strand arc-length configurations $\{N_i\}$ are equally probable; that is, the slip-links are evenly randomly distributed along the polymer arc-length in equilibrium in a chemical potential field. To see this consider the following valid Green function relationships:

$$G(\vec{r}_i, \vec{r}_{i+2}; N_i + N_{i+1}) = \int d\vec{r}_{i+1} G(\vec{r}_i, \vec{r}_{i+1}; N_i) G(\vec{r}_{i+1}, \vec{r}_{i+2}; N_{i+1}) \tag{5.15}$$

$$q(\vec{r}_i; N_i + N_{i+1}) = \int d\vec{r}_{i+1} G(\vec{r}_i, \vec{r}_{i+1}; N_i) q(\vec{r}_{i+1}; N_{i+1}) \tag{5.16}$$

$$\int d\vec{r}\, q(\vec{r}; N_1) q(\vec{r}; N_2) = f(N_1 + N_2, \mathcal{V}) \tag{5.17}$$

The integral in Equation 5.15 removes a shared constraint between two doubly con-

strained strands so that one longer strand is being considered. Equation 5.16 makes an analogous statement when one of the strands involved is only singly constrained. Equation 5.17 states that integrating the product of two singly constrained strand end probability densities for strands that share a constraint gives a result that depends only on the sum of the strand contour lengths and the volume of integration $\mathcal{V}$; this integral is proportional to the probability that the polymer is found in the integrated volume, and depending on normalization may be identically unity.

The relationships in Equations 5.15, 5.16, and 5.17 can be used when integrating the full in-field configuration probability distribution (Equation 5.11) over the slip-link positions $\{\vec{r}_i\}$. It can be seen that such an integration gives an expression for $P(Z, \{N_i\})$ that does not depend on the strand arc-length configuration $\{N_i\}$. This means that in equilibrium in the chemical potential field all possible $\{N_i\}$ configurations for a given number of slip-links Z are equally probable, and the slip-links are evenly randomly distributed along the polymer contour in this model.

5.3 Green Function Calculation

The Green function may be calculated via the equations:

$$\frac{\partial G(\vec{r}, \vec{r}'; N_s)}{\partial N_s} = \frac{b^2}{6}\nabla^{2\prime} G(\vec{r}, \vec{r}'; N_s) - \frac{\omega(y)}{\mathrm{k_B}T} G(\vec{r}, \vec{r}'; N_s) \tag{5.18}$$

$$G(\vec{r}, \vec{r}'; 0) = \delta(\vec{r} - \vec{r}') \tag{5.19}$$

The explanation for how Equations 5.18 and 5.19 are valid for determining the Green function is as follows (the method of derivation follows the route given in [36]).

Consider a Gaussian polymer of arc-length N_s in a chemical potential field. The chemical potential field will influence the equilibrium conformation of the polymer;

the free energy of any small section of the polymer arc-length dn will be given by Equation 5.6, and the statistical weight for the collection of polymer configurations with ends fixed at $\vec{r}$ and $\vec{r}'$ will be as given in Equation 5.7. The polymer Green function $G(\vec{r},\vec{r}';N_s)$ is defined by Equation 5.9.

Consider the construction of a Green function for a polymer with an arc-length longer by small amount ΔN. Using the relation in Equation 5.15 this new Green function may be expressed as:

$$G(\vec{r},\vec{r}';N_s+\Delta N)=\int d\vec{r}''G(\vec{r},\vec{r}'';N_s)G(\vec{r}'',\vec{r}';\Delta N) \tag{5.20}$$

ΔN is considered very small in the sense that the free energy penalty for stretching a polymer strand with length ΔN keeps the strand end separation distance small such that the chemical potential is approximately constant over all significantly probable end separation distances. In such a case $G(\vec{r}',\vec{r}'';\Delta N)$ can be approximated by:

$$G(\vec{r}',\vec{r}';\Delta N)\approx G_0(\vec{Q};\Delta N)\exp\left[-\frac{\omega(\vec{r}')\Delta N}{\mathrm{k_B}T}\right] \tag{5.21}$$

Here G_0 is the equilibrium strand end-to-end vector distribution (Equation 4.2), with $\vec{Q}\equiv\vec{r}'-\vec{r}''$.

$G(\vec{r},\vec{r}'';N_s)$ may be expressed as $G(\vec{r},\vec{r}'-\vec{Q};N_s)$. Because ΔN is very small $G_0(\vec{Q};\Delta N)$ will be sharply peaked about $\vec{Q}=0$. This suggests $G(\vec{r},\vec{r}'-\vec{Q};N_s)$ be expanded in powers of $\vec{Q}$:

$$G(\vec{r},\vec{r}'-\vec{Q};N_s)=\left(1-\sum_i Q_i\frac{\partial}{\partial r_i'}+\frac{1}{2}\sum_{i,j}Q_iQ_j\frac{\partial^2}{\partial r_i'\partial r_j'}+...\right)G(\vec{r},\vec{r}';N_s) \tag{5.22}$$

Here the subscripts i and j indicate directional components.

Using Equations 5.21 and 5.22 the relation in Equation 5.20 can be rewritten as:

$$G(\vec{r},\vec{r}';N_s+\Delta N) = \int d\vec{Q}\, G_0(\vec{Q};\Delta N)\exp\left[-\frac{\omega(\vec{r}')\Delta N}{\mathrm{k_B}T}\right]\cdot \left(1-\sum_i Q_i\frac{\partial}{\partial r_i'}+\frac{1}{2}\sum_{i,j}Q_iQ_j\frac{\partial^2}{\partial r_i'\partial r_j'}+...\right)G(\vec{r},\vec{r}';N_s) \quad (5.23)$$

Here the integral with respect to $\vec{r}''$ has been changed to an integral with respect to $\vec{Q}$ using $d\vec{Q} = -d\vec{r}''$ ($\vec{r}'$ is taken as fixed). The sign of the total integral stays the same as the change to $d\vec{Q}$ reverses both the sign of the differential and the signs of the integral limits (taking the limits to be very large compared to probable chain end separation distances).

Because G_0 is symmetric with respect to $\vec{Q}$ (Equation 4.2) when performing the integral only the terms involving even powers of the $\vec{Q}$ components will be non-zero. Performing the integral gives:

$$G(\vec{r},\vec{r}';N_s+\Delta N) = \exp\left[-\frac{\omega(\vec{r})\Delta N}{\mathrm{k_B}T}\right]\left(\Delta N\frac{b^2}{6}\nabla^2+...\right)G(\vec{r},\vec{r}';N_s) \quad (5.24)$$

Here the prime superscripts have been dropped as the expression is symmetric with which respect to interchange of $\vec{r}$ and $\vec{r}'$ (though ω and the laplacian should be evaluated with respect to the same vector).

Expanding $G(\vec{r},\vec{r}';N_s+\Delta N)$ and the exponential in powers of ΔN and collecting terms gives:

$$\left(1+\Delta N\frac{\partial}{\partial N_s}+...\right)G(\vec{r},\vec{r}';N_s) = \left(1+\Delta N\left(\frac{b^2}{6}\nabla^2-\frac{\omega(\vec{r})}{\mathrm{k_B}T}\right)+...\right)G(\vec{r},\vec{r}';N_s) \quad (5.25)$$

For the equality in Equation 5.25 to hold the terms with equivalent powers of ΔN must be equal. Comparing the terms that are first order in ΔN results in the differential

equation:

$$\frac{\partial G(\vec{r},\vec{r}';N_s)}{\partial N_s} = \left(\frac{b^2}{6}\nabla^2 - \frac{\omega(\vec{r})}{\mathrm{k_B}T}\right) G(\vec{r},\vec{r}';N_s) \tag{5.26}$$

This differential equation for G is exact for a Gaussian strand in a chemical potential, and not just approximate. Though the derivation involved a hypothetical extension of arc-length by small amount ΔN this mechanism was just a conceptual device. An imaginary extension of arbitrarily small arc-length ΔN is a valid conceptual situation, and the derived differential equation is valid in general (for a Gaussian filament).

Equations 5.18 and 5.19 may be solved for G for a chosen set of boundary conditions. Because a chemical potential field that is only a function of the y coordinate is being considered, the solution for G in Equation 5.18 is separable:

$$G(\vec{r},\vec{r}';N_s) = G_x(x,x';N_s)G_y(y,y';N_s)G_z(z,z';N_s) \tag{5.27}$$

A differential equation of the form of Equation 5.18 may be solved for each of the dimensional components of G separately; when solving for the G_y the equation will involve the chemical potential $\omega(y)$, but when solving for G_x and G_z the chemical potential may be omitted as it is unchanging in x and z dimensions. Consequently, when solving for G_x and G_z using continuum boundary conditions it is found that both have the form of Gaussian functions of one dimension:

$$G_z(z,z';N_s) = \left(\frac{3}{2\pi N_s b^2}\right)^{1/2} \exp\left[-\frac{3(z-z')^2}{2N_s b^2}\right] \tag{5.28}$$

The expression for G_x will be the same as in Equation 5.28 substituting x for z. From Equation 5.28 it can be seen that in this specific case where the chemical potential field is not a function of the x and z coordinates G_x and G_z will be equal to simple Gaussians, and if the chemical potential field is not present or flat the entire Green function will reduce to the Gaussian probability density G_0 given in Equation 4.2.

In the same way that the Green functions may be separated into multiplicative dimensional components the q functions may be also be separated into dimensional components. For example, considering the z directional component $q_z(z; N_s) = \int dz' G_z(z, z'; N_s) = 1$; it is found that $q_z = 1$ since integrating G_z (Equation 5.28) over all z results in a value of one. Similarly, it is found that $q_x = 1$. For q_y the situation is different because the chemical potential field is non-trivial along the y direction; q_y is numerically determined from G_y using $q_y(y; N_s) = \int dy' G_y(y, y'; N_s)$.

G_y must be solved for numerically because the chemical potential field describing the polymer-polymer interface is a function of the y coordinate. A differential equation of the form of Equation 5.18 is numerically solved for G_y using periodic boundary conditions (the details of the solution method are given in Appendix B). The resulting numerically determined $G_y(y, y'; N_s)$ is kept on a three dimensional grid (the three dimensions being y, y', and N_s). Obtaining a value for G_y in simulation for a particular set of y, y', and N_s, is done by trilinear interpolation on the G_y grid. Similarly, the function $q_y(y; N_s)$ associated with the polymer end strands is obtained numerically through integration of G_y. The function q_y is stored on a two dimensional grid (the dimensions being y and N_s), and q_y values are obtained in simulation using bilinear interpolation on the q_y grid.

5.4 Configuration Sampling via Green Functions

The in-field configuration probability density involving the Green and q functions (Equation 5.11) is enforced in simulation through the Monte Carlo move acceptance probabilities. In the presence of a chemical potential field the Monte Carlo move acceptance probabilities are altered, but the choice is made to use the same Monte Carlo move proposal probabilities as in the zero chemical potential case. In the case

of the arc length shuffle moves the probability distribution for the proposed amount of arc to shuffle is the same as previously given in Equation 4.13, which once again leads to the shuffle move acceptance probability ratio expression in Equation 4.16. Evaluating this move acceptance probability ratio using the in-field configuration probability density in Equation 5.11 for a shuffle move involving two interior strands gives:

$$\frac{A(\Omega_j \to \Omega_k)}{A(\Omega_k \to \Omega_j)} = \frac{G(\vec{r}_m, \vec{r}_{m+1}; N_m - \Delta N)G(\vec{r}_{m+1}, \vec{r}_{m+2}; N_{m+1} + \Delta N)}{G(\vec{r}_m, \vec{r}_{m+1}; N_m)G(\vec{r}_{m+1}, \vec{r}_{m+2}; N_{m+1})} \tag{5.29}$$

Here G is the product of its dimensional components $G = G_x G_y G_z$; the two dimensional components G_x and G_z are evaluated analytically using Equation 5.28, while the component G_y associated with the direction along which the chemical potential field changes is evaluated numerically as previously discussed. Denoting the right side of Equation 5.29 as λ this shuffle move acceptance probability ratio is enforced in simulation through the Metropolis method by taking $A(\Omega_j \to \Omega_k)$ to be conditionally equal to λ according to the rule given by Equation 4.19. The form of the acceptance probability is symmetric under a reversal of which strand is losing and which is gaining arc-length during the shuffle move. Consequently this acceptance probability is correct for any shuffle move between interior strands taking m as the index of the strand losing the arc length and $m+1$ as the strand gaining arc-length.

If instead of involving two interior strands the shuffle move is moving arc length between an interior polymer strand and an end strand the move acceptance probability ratio is given by:

$$\frac{A(\Omega_j \to \Omega_k)}{A(\Omega_k \to \Omega_j)} = \frac{G(\vec{r}_m, \vec{r}_{m+1}; N_m - \Delta N)q(\vec{r}_{m+1}; N_{m+1} + \Delta N)}{G(\vec{r}_m, \vec{r}_{m+1}; N_m)q(\vec{r}_{m+1}; N_{m+1})} \tag{5.30}$$

Again denoting the right side of Equation 5.30 as λ this ratio is enforced by taking

$A(\Omega_j \to \Omega_k)$ as given in Equation 4.19. Because of the symmetry involved this is the correct acceptance probability for all shuffle moves involving an interior strand and an end strand, where m is taken as the index of the interior strand and $m+1$ as the index of the end strand. If the shuffle move is moving arc-length from the end strand to the interior strand the sign of ΔN in Equation 5.30 will be negative.

The acceptance probability for slip-link create/destroy moves in the presence of a chemical potential field may be determined in an analogous way. The slip-link create/destroy moves are required to satisfy detailed balance in the presence of the chemical potential field; using the detailed balance condition given in Equation 4.15 an expression for the required ratio of move acceptance probabilities may be obtained. The way slip-link creation or destruction move proposals are made in a chemical potential field is unchanged from the zero chemical potential field case; the only thing altered in a chemical potential field are the move acceptance probabilities. Again Ω_j and Ω_k denote two configurations that are in every way identical except for Ω_j possessing one more slip-link than Ω_k (Ω_j has Z slip-links while Ω_k has $Z-1$ slip-links). The probability that configuration Ω_j will experience a slip-link destruction move proposal for the transition $\Omega_j \to \Omega_k$ is again given by $R(\Omega_j \to \Omega_k)$ as shown in Equation 4.23. Similarly, the probability that configuration Ω_k will experience a slip-link creation move proposal for the transition $\Omega_k \to \Omega_j$ is given by $R(\Omega_k \to \Omega_j)$ as shown in Equation 4.24. Detailed balance requires the move acceptance probability ratio for these two Monte Carlo moves by given by the relation in Equation 4.26. Using the transition proposal probabilities, and the in-field configuration probability density give in Equation 5.11, the required move acceptance probability ratio becomes:

$$\frac{A(\Omega_j \to \Omega_k)}{A(\Omega_k \to \Omega_j)} = \frac{\beta}{N_{E*}} \frac{G_0(\vec{Q}_{Z-1}; N_{Z-1}) q(\vec{r}_{Z-1}; N_{Z-1} + N_Z)}{G(\vec{r}_{Z-1}, \vec{r}_Z; N_{Z-1}) q(\vec{r}_Z; N_E)} \tag{5.31}$$

$$G_0(\vec{Q}_s; N_s) \equiv \left(\frac{3}{2\pi N_s b^2}\right)^{3/2} \exp\left[-\frac{3\vec{Q}_s}{2N_s b^2}\right] \tag{5.32}$$

Here G_0 is the zero field analytic Green function as shown in Equation 5.32, and $\vec{Q}_{Z-1} \equiv \vec{r}_Z - \vec{r}_{Z-1}$. N_{E*} is again the available end-strand arc-length in which a newly created slip-link may be placed, and is as given in Equation 4.25. Denoting the right side of Equation 5.31 as κ, the required slip-link create/destroy move acceptance probability ratio is enforced in the simulation through the Metropolis rule by the acceptance probabilities:

$$A(\Omega_j \to \Omega_k) = \begin{cases} \kappa & \text{if } \kappa < 1 \\ 1 & \text{if } \kappa \geq 1 \end{cases} \qquad A(\Omega_k \to \Omega_j) = \begin{cases} \frac{1}{\kappa} & \text{if } \frac{1}{\kappa} < 1 \\ 1 & \text{if } \frac{1}{\kappa} \geq 1 \end{cases} \tag{5.33}$$

The move acceptance probabilities given for shuffle moves (Equations 5.29 and 5.30) and for slip-link create/destroy moves (Equations 5.31, 5.32, and 5.33) enforce detailed balance for a simulated polymer in equilibrium in the presence of a chemical potential field. To verify this a histogram of the spatial positions of slip-links may be checked. Because in this model the slip-links are expected to be evenly randomly distributed along the polymer arc-length in equilibrium as previously discussed, the slip-link space histogram profile is expected to be proportional to the arc-length volume fraction profile obtained from self-consistent field theory. The expected volume fraction profile for each polymer species may be obtained from self-consistent field theory using the relation:

$$\phi_A(\vec{r}) = \frac{1}{Q(N)} \int_0^N q_A(\vec{r}; N_s) q_A(\vec{r}; N - N_s) dN_s \tag{5.34}$$

The comparison between the slip-link locations and the self-consistent volume fraction is shown below.

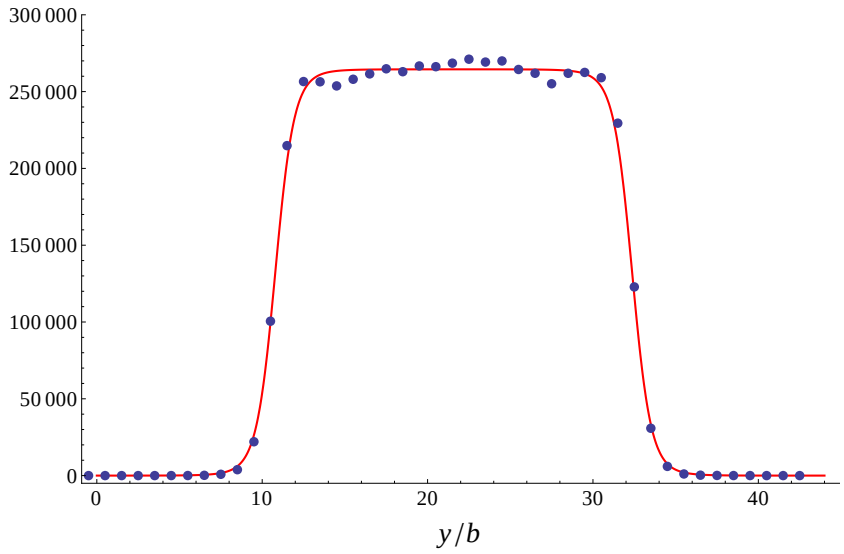

Figure 5.3: Slip-link space position histogram compared to the predicted volume fraction profile from self-consistent field theory. The dots are a histogram of slip-link positions along the direction perpendicular to the planar interfaces (y). The red line is the volume fraction profile expected from self-consistent field theory (fit to the height of the histogram). The simulation was performed with $\chi = 0.15$, $N = 110$, $\beta = 3.125$, spatial period $= 43.16\,b$, $\Delta t = 2.56(10^{-5})t_e$.

As can be seen in Figure 5.3 the histogram of slip-link locations for polymers simulated between two polymer-polymer interfaces (represented by a self-consistently determined chemical potential field) is found to track closely with the self-consistently determined volume fraction ϕ_A as expected. The generalized Monte Carlo moves employing the polymer strand Green functions correctly convey the influence of the self-consistent chemical potential field representing a polymer-polymer interface.

When simulating polymers near a planar boundary identities are assigned to slip-links such that some slip-links represent entanglements between the polymer melts. That is, when simulating a polymer of species A every slip-link either represents an entanglement of the species A polymer with another species A polymer, or an entanglement of the species A polymer with a species B polymer. The assignment

of slip-link identity is made probabilistically during slip-link creation based on the local species volume fraction at the point of slip-link creation (species density is determined from self-consistent field theory). The arc-length volume fractions of the two polymer melts are at every point subject to the incompressibility requirement $\phi_A(\vec{r})+\phi_B(\vec{r}) = 1$. When a new slip-link is placed on a simulated species A polymer at position $\vec{r}$ the probability that this slip-link will represent an interfacial entanglement (an entanglement with a species B polymer) is equal to $\phi_B(\vec{r})$ which is equivalent to $1 - \phi_A(\vec{r})$.

Because slip-link identities are assigned probabilistically in the described manner the spatial density of interfacial entanglements $\rho_{AB}(\vec{r})$ is expected to be proportional to the product of the species volume fractions $\rho_{AB}(\vec{r}) \sim \phi_A(\vec{r})\phi_B(\vec{r})$. This can be checked in simulation by comparing a histogram of the interfacial slip-link locations to the product of the self-consistently determined polymer species arc-length densities.

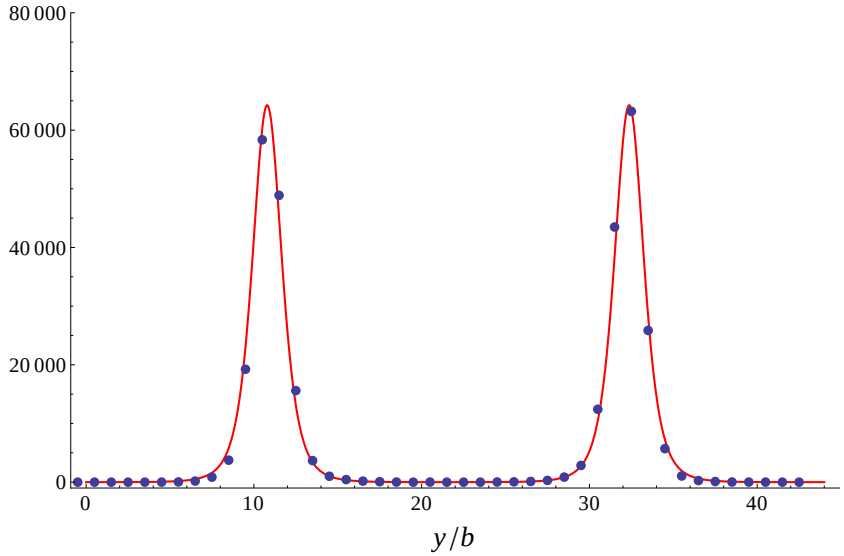

Figure 5.4: Histogram of the locations of interfacial entanglements along the direction perpendicular to the planar interface (y). Interfacial entanglements are species B slip-links present on simulated species A polymers. The line represents the self-consistent field prediction for the interspecies volume fraction overlap product $\phi_A(y)\phi_B(y)$ multiplied by a constant to fit the height of the histogram. The simulation was performed with $\chi = 0.15$, $N = 110$, $\beta = 3.125$, spatial period $= 43.16b$, $\Delta t = 2.56(10^{-5})t_e$.

As can be seen, the shape histogram of interfacial entanglement positions agrees with the shape of the product of the self-consistently determined species densities $\phi_A(y)\phi_B(y)$, giving the expected profile for inter-melt polymer entanglements.

Chapter 6

Simulation of Interfacial Slip

6.1 Slip Simulation Method

In order to simulate interfacial slip at a planar boundary between two immiscible polymer melts, polymers are first simulated in a chemical potential field designed to describe a planar interface between immiscible polymer melts. The simulation model considers two homopolymer melts of chemical species A and B, respectively, that have a repulsive interaction described by the Flory-Huggins [48–50] interaction parameter χ. The polymer melts are considered to be incompressible, and the system is of fixed uniform arc-length density. Self-consistent field theory is used to solve for the chemical potential field describing a planar interface between two such polymer melts (the details of the self-consistent field theory calculation are given in Appendix B). The polymer strand statistical weights in the chemical potential field are calculated, in the form of Green functions, which are used to consistently govern Monte Carlo move acceptance probabilities as described in the previous chapter. Slip-links are assigned a polymer species identity probabilistically based on the local species volume fraction calculated from self-consistent field theory, resulting in slip-links representing interfacial entanglements being located in the melt interfacial regions as illustrated

in Figure 5.4 of the previous chapter. Forces are transmitted by interspecies slip-link entanglements at the interface. This simulation does not include Rouse-like rubbing friction. Both melts are treated as being composed of polymers with the same arc-length N, statistical segment length b, entanglement friction coefficient ζ, and average number of entanglements Z (the same β parameter is used for both). The entire system is treated as being at the same unchanging absolute temperature T.

In order to simulate interfacial slip, interfacial slip-links are translated at a constant velocity in the $\hat{x}$ direction, parallel to the planar interface. This method of simulation treats the interfacial deformation as a "perfect slip" deformation, by which it is meant that all the polymers of one species are translating at constant velocity relative to the polymers of the other species. In this perfect slip approximation strain deformations of the polymer melts are ignored, and only the stress induced by perfect slip at the polymer-polymer interface are considered. In simulation different interfacial slip velocities are imposed, and the resulting steady state interfacial stresses σ_{yx} are observed. From this data an interfacial stress / slip velocity relationship is constructed. The simulation is used to study the interfacial stress induced by constant velocity perfect slip at a planar polymer-polymer interface.

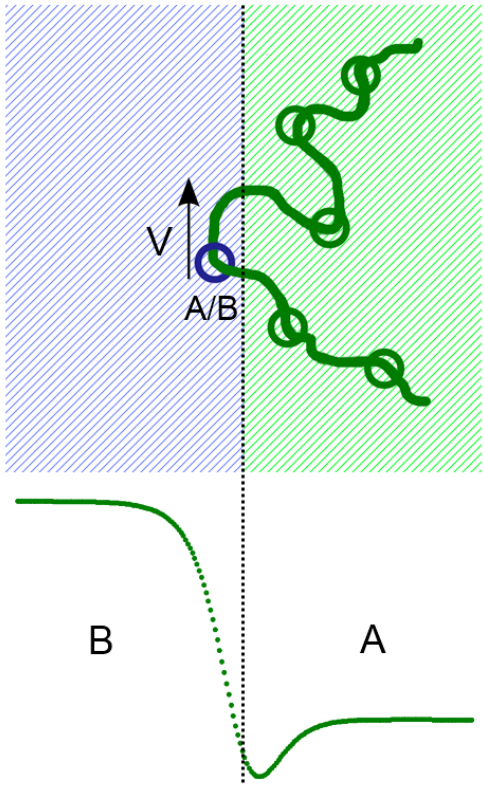

Figure 6.1: Simulated interfacial slip illustration. An A type polymer is simulated near a planar interface between the A and B type polymer melts. The two melts are immiscible with a positive χ interaction parameter. The interface is described through a self consistently determined chemical potential ω_A field which is shown in the lower half of the figure. The simulated polymer will spend most of its time in the region where the chemical potential field is low, but will occasionally wander into the B rich region. In the B rich region it may form a slip-link representing an entanglement with a B polymer. Interfacial slip is simulated by translating all B type entanglements at a constant velocity (relative to the A type entanglements) parallel to the planar interface.

6.2 Interfacial Slip Simulation Results

Simulations of interfacial slip were performed for different slip velocities, and for polymers of different overall length. From these simulations it is possible to examine the relationship between the interfacial slip velocity and the interfacial stress, as well

as the effects of interfacial slip on the population of interfacial entanglements. When the slip deformation is begun the system goes through a transition period before settling into a steady state. A sample of the interfacial stress behavior following onset of interfacial slip is shown below.

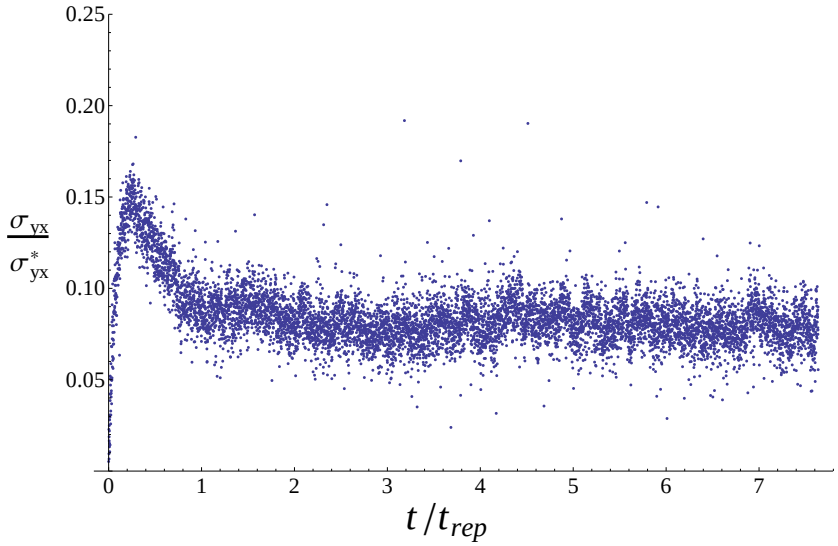

Figure 6.2: Interfacial stress at an interface vs. time during the onset of interfacial slip. The system goes through a transition period before settling into steady state behavior. Simulation parameters: $N = 50$, $\beta = 3.125$, $\chi = 0.15$, simulation timestep $\Delta t = 2.56(10^{-5})t_e$. Imposed interfacial slip velocity $V = 5.79(10^{-4})V_a$.

As can be seen in Figure 6.2, the interfacial stress goes through a transition period following the beginning of imposed interfacial slip before settling into a steady state value. This study is primarily focused on the steady state stress response to polymer-polymer interfacial slip, and the interfacial stress results presented below are all obtained from systems that have settled into steady state behavior.

For all of the simulation results presented in this chapter the system spatial period (the total $\hat{y}$ direction thickness of both polymer layers) was $43.16b$. All systems also used a Flory-Huggins interaction parameter of $\chi = 0.15$.

When reporting the results of interfacial slip simulations it is sometimes most

natural to express the interfacial slip velocity in units of $V^* = a/t_{rep}$ (the characteristic strand alignment slip velocity) or $V^{**} = L/t_{rep}$ (the characteristic disentanglement slip velocity). For each simulated melt the value of t_{rep} is determined by fitting a function of the form $A\exp[-t/t_{rep}]$ to the long-time stress decay following a small step strain as shown in Figure 4.13. In situations where both strand alignment and interfacial disentanglement are being considered, or different length polymers are being compared, the slip velocity is given in units of V_a. The velocity V_a is the entanglement length a divided by the characteristic time for the polymer to diffuse the entanglement distance t_e (Equation 4.29), and is the fundamental simulation velocity scale.

$$V_a \equiv \frac{a}{t_e} = \frac{\mathrm{k_B}Tb}{N_e^{3/2}\zeta_s} \tag{6.1}$$

The physical effects of interfacial slip in simulation are now examined. First, the influence of interfacial slip on the arc-locations of interfacial entanglements is examined via the following histogram:

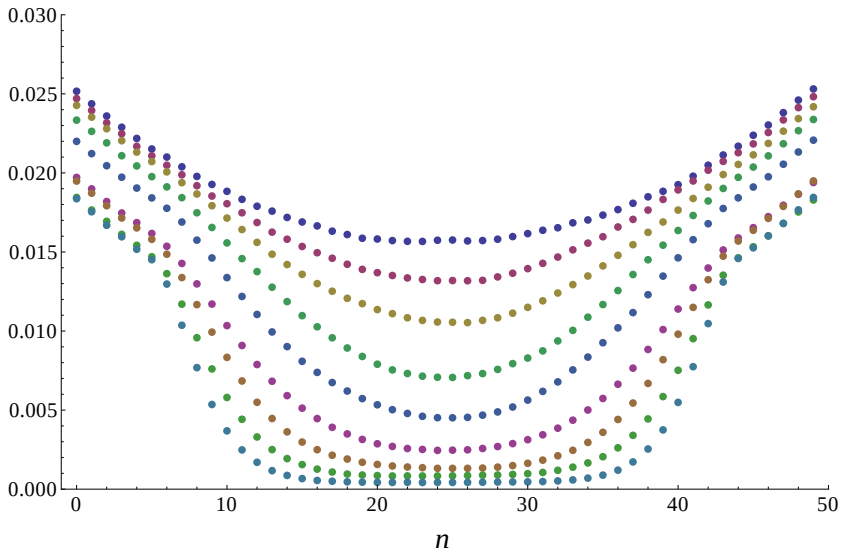

Figure 6.3: Histogram of interfacial slip-link locations along the polymer arc-length during simulated interfacial slip. Higher slip velocities result in interfacial entanglements being nearer to the polymer ends. In order from least to greatest the simulated slip velocities are: $0.046V^{**}$, $0.092V^{**}$, $0.18V^{**}$, $0.37V^{**}$, $0.73V^{**}$, $1.48V^{**}$, $2.96V^{**}$, $5.92V^{**}$, $11.8V^{**}$. Histograms are normalized such that with zero slip the entries would sum to 1. Simulation parameters: $N = 50$, $\beta = 3.125$, $\chi = 0.15$, simulation timestep $\Delta t = 2.56(10^{-5})t_e$. Slip-link creation / destruction happens in arc-length regions of length $2\beta = 6.25$ near the polymer ends.

As can be seen from Figure 6.3, interfacial slip tends to cause interfacial entanglements to be located nearer to the polymer ends where slip-link creation and destruction occurs. This effect increases with increasing slip velocity. The simulation result displayed in Figure 6.3 shows an effect in agreement with prediction of the analytical model shown in Figure 3.5. The effect of the finite arc-length region of slip-link creation and destruction in the simulation can be seen in the shape of the histogram in Figure 6.3; in the end arc-length regions where slip-link creation and destruction occurs (arc-length $2\beta = 6.25$ near the polymer ends) the histogram shows a different and more linear shape. The same value for the arc-length creation/destruction region was used in all simulations presented here.

An additional effect in the simulation can cause interfacial entanglements to cluster closer to the polymer ends. In self-consistent field theory the polymer ends tend to enter the interfacial region more than the central polymer sections. Simply put, this is due to the fact that central polymer regions entering the interface bring two trailing polymer strands, while a polymer end entering the interface brings one trailing polymer strand. Thus the energy penalty for a polymer end entering the interfacial region is smaller than for a central polymer section entering the interfacial region (the interfacial chemical potential field induces an energy penalty conjugate to polymer arc-length). Consequently, in simulation the polymer end sections are expected to spend more time in the interfacial region than the central polymer sections, and there will be some clustering of interfacial entanglements near the polymer ends even when no slip is present.

Also evident in Figure 6.3 is the fact that at higher slip velocities the total number of interfacial entanglements decreases. To analyze this effect the average number of interfacial entanglements remaining per polymer as a function of slip velocity was studied, and this simulation data is shown below.

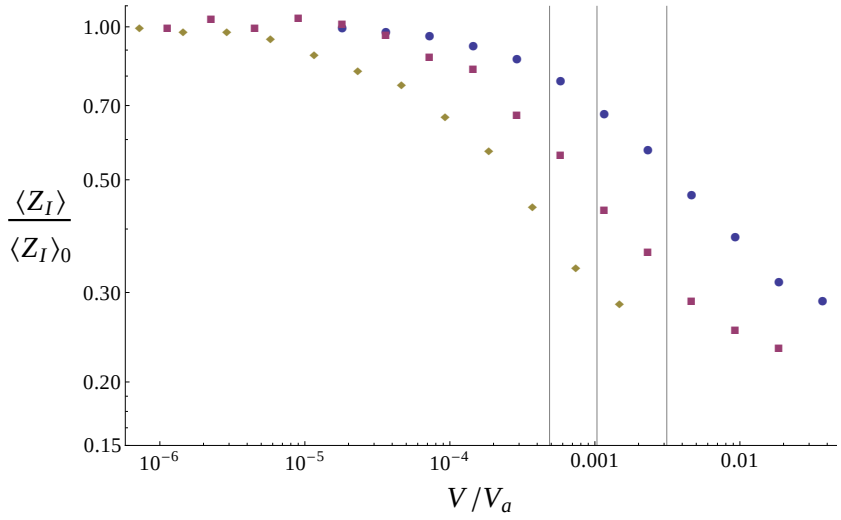

Figure 6.4: Average fraction of interfacial entanglements Z_I remaining (compared to the zero slip value) vs. slip velocity V. Both axes in logarithmic scale. Different symbols correspond to different polymer lengths, and the vertical lines indicate the expected characteristic disentanglement velocities $V^{**} \equiv L/t_{rep}$: Circle: $N = 50$, $V^{**} = 3.13(10^{-3})V_a$, Square: $N = 80$, $V^{**} = 1.04(10^{-3})V_a$, Diamond: $N = 110$, $V^{**} = 4.87(10^{-4})V_a$. Simulation parameters: $\beta = 3.125$, $\chi = 0.15$, simulation timestep $\Delta t = 2.56(10^{-5})t_e$.

In Figure 6.4 it can be seen that the fraction of interfacial entanglements remaining (relative to the zero slip equilibrium value) decreases earlier with respect to slip velocity for polymers of greater length. This is in qualitative agreement with the prediction of the analytic model for interfacial slip. The interfacial slip model predicts a characteristic disentanglement slip velocity $V^{**} \sim L/t_{rep}$; above this slip velocity the fraction of interfacial entanglements remaining is expected to be significantly reduced. The scaling of the reptation time is roughly $t_{rep} \propto L^3$, with L being the polymer primitive path length. This means V^{**} is expected to decrease with L approximately according to $V^{**} \propto L^{-2}$. The calculated values for the V^{**} associated with each simulated polymer length are shown by the vertical lines in Figure 6.4. In Figure 6.4 it can be seen that the V^{**} estimates are within a factor of 2 of the slip velocity at which the number of interfacial entanglements is reduced to half of the zero slip

equilibrium value for each polymer length. From this data it remains difficult to assess whether the scaling of the characteristic disentanglement velocity with respect to polymer length is precisely in agreement with the analytic theory, but it is correct that longer polymers have lower characteristic interfacial disentanglement velocities, and the V^{**} estimates from the analytic model appear accurate to within an order of magnitude.

In the analytic model of interfacial slip it is expected that interfacial strands will be primarily aligned in the direction of slip at slip velocities larger than the characteristic slip velocity $V^* \sim a/t_{rep}$. Here a is the entanglement distance, or the average distance between entanglements in equilibrium. Consequently the analytic model predicts that interfacial strand alignment will plateau above a slip velocity of V^*. Simulation data for interfacial strand alignment as a function of slip velocity is shown below.

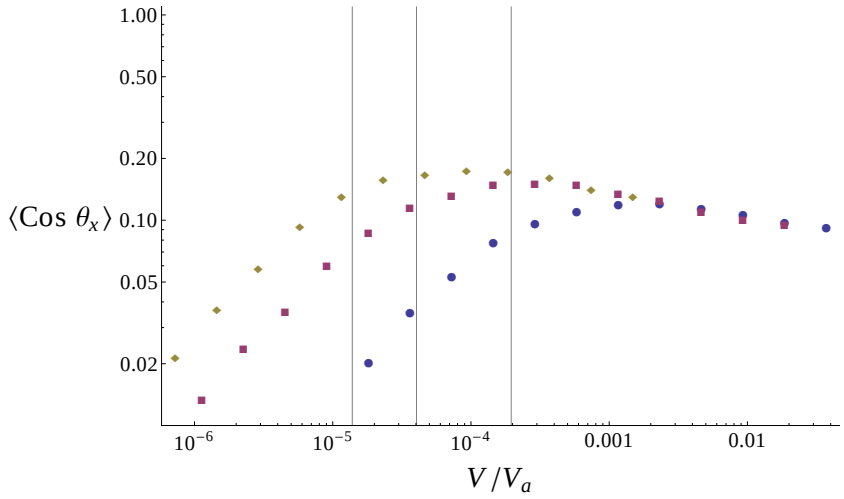

Figure 6.5: Slip direction interfacial strand alignment vs. slip velocity V. Both axes in logarithmic scale. Different symbols correspond to different polymer lengths, and the vertical lines indicate the expected characteristic alignment slip velocities $V^* = a/t_{rep}$: Circle: $N = 50$, $V^* = 1.96(10^{-4})V_a$, Square: $N = 80$, $V^* = 4.04(10^{-5})V_a$, Diamond: $N = 110$, $V^* = 1.38(10^{-5})V_a$. Simulation parameters: $\beta = 3.125$, $\chi = 0.15$, simulation timestep $\Delta t = 2.56(10^{-5})t_e$.

In Figure 6.5 the average cosine of the angle θ_x between interfacial strands and the direction of slip ($\hat{x}$) is plotted as a function of slip velocity. For strands completely aligned in the direction of slip this cosine value would be 1. The calculated values of V^* for the different polymer lengths are indicated in the figure by vertical lines. In the figure it can be seen that interfacial strand alignment does enter a plateau region for slip velocities of order V^* or greater, however, the alignment plot has some features not anticipated in the analytic theory of slip. In the previously developed theory it was predicted that at slip velocities above V^* the interfacial strands would be nearly aligned in the direction of slip. In Figure 6.5 total interfacial strand alignment would be indicated by an average cosine value of 1. Instead it is found that the $\langle \cos \theta_x \rangle$ reaches a plateau value between 0.1 to 0.2. Additionally, after the onset of the alignment plateau the alignment value actually shows a slow decrease with increasing slip velocity. Upon further examination, it appears that both of these effects are due to a significant presence of relatively newly formed slip-links, which give strands random orientation, and dilute the total alignment value. The way that the simulated polymers have their slip-links driven to the end regions of fast slip-link creation and destruction at higher slip velocities increases the number of younger slip-links present on the simulated polymers.

In the simulation the arc-length regions near the polymer ends are locations of fast slip-link creation and destruction. In the data presented here these end regions have arc-length equal to twice the average equilibrium arc length separation between slip-links. The rates of slip-link creation and destruction in these end regions were chosen to be high enough such that the simulation was insensitive to further increases in the creation and destruction rate; slip-link creation and destruction happens quickly enough that the slip-links in the polymer end regions are always in a state of equilibrium. Consequently, when slip-links representing interfacial entangle-

ments are present in these end regions the interfacial strands associated with them are randomly aligned. These randomly aligned interfacial strands tend to dilute the measurement of the alignment quantity $\langle \cos \theta_x \rangle$. For large slip velocities the effect of slip-induced polymer retraction tends to drive slip-links toward the polymer end regions as illustrated in Figure 6.3, which increases the relative magnitude of the effect.

By examining the interfacial strand alignment as a function of survived interfacial slip it is possible to see that long-lived interfacial strands are aligned in the direction of slip. By survived slip I mean the amount of slip Δx which has occurred while a strand with one interfacial slip-link has been in existence (without either of the flanking interfacial slip-links being destroyed).

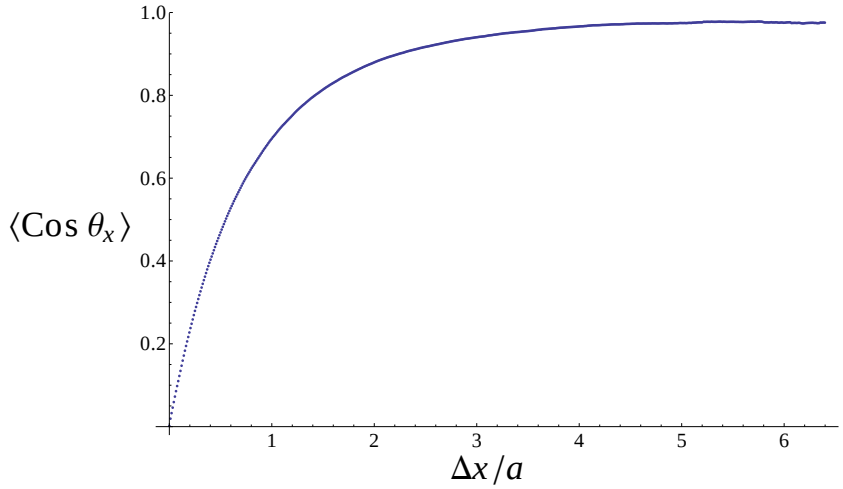

Figure 6.6: Slip direction interfacial strand alignment vs. the slip distance Δx. $\Delta x = V t_s$ where t_s is the length of time since creation of the youngest slip-link flanking an interfacially entangled strand. Simulation parameters: $V = 1.16(10^{-3})V_a$, $\beta = 3.125$, $\chi = 0.15$, simulation timestep $\Delta t = 2.56(10^{-5})t_e$.

Figure 6.6 shows strand alignment vs. survived slip $\Delta x = V t_s$ (t_s being the length of time the youngest slip-link flanking an interfacial strand has existed). It can be seen in this figure that the older strands which have survived more interfacial slip

become aligned in the direction of slip (θ_x is the angle between the polymer strand and the direction of interfacial slip). This indicates that long-lived interfacial strands do become aligned in the direction of slip, and the fact that the alignment plateau value in Figure 6.5 is less than 1 is due to enough younger polymer strands being present to dilute the plateau alignment value.

The analytic theory of stress induced interfacial slip predicts an onset of an interfacial stress plateau at interfacial slip velocity V^*. The theory predicts that slip-induced interfacial stress increase is primarily due to the alignment of interfacially entangled polymer strands, with strand tension being little altered from the thermal equilibrium tension. A stress decrease is expected for slip velocities on the order of V^{**} or greater, due to slip-induced interfacial disentanglement occurring at these larger slip velocities.

Below the interfacial stress is examined, and stress is plotted in units of the expected plateau stress $\sigma^*_{yx} = 6\rho_0 \mathrm{k_B}T/a$ (Equation 3.8). For each system the equilibrium number of interfacial entanglements per area ρ_0 is determined from a zero slip simulation.

When determining the stress component σ_{yx} the strand force in the slip direction is given by $f_x = 3\mathrm{k_B}TQ_x/(N_s b^2)$ via Equation 4.1. The chemical potential field describing the interface only varies in the direction perpendicular to the interface $\hat{y}$, and consequently the strand force components parallel to the interface retain their bulk form. More specifically, the strand free energy obeys $F_s \propto \ln[G_x G_y G_z]$, with the G factors being components of the strand Green function; the strand Green functions can be factored into separate dimensional components if the chemical potential field depends on only one of the dimensions. The components G_x and G_y retain their bulk equilibrium form, and similarly the force components $f_x = \partial F_s/\partial x$ and $f_y = \partial F_s/\partial y$ are given by the bulk expression (Equation 4.1).

A comparison of simulation interfacial stress results for polymers of different length is shown below.

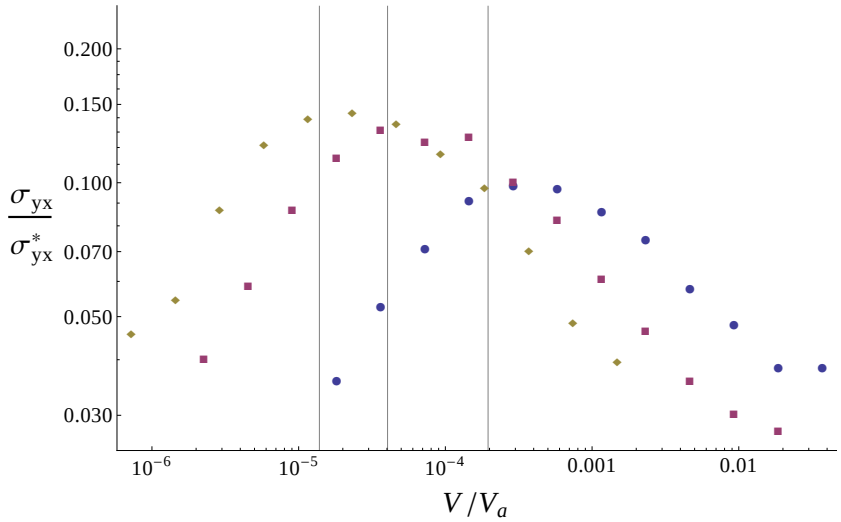

Figure 6.7: Interfacial stress σ_{yx} vs. slip velocity V for three polymer lengths. Both axes in logarithmic scale. Different symbols correspond to different polymer lengths, and the vertical lines indicate the expected characteristic strand alignment slip velocity $V^* = a/t_{rep}$, which is expected to mark the lower bound of an interfacial stress plateau with respect to slip velocity. Circle: $N = 50$, $V^* = 1.96(10^{-4})V_a$, $V^{**} = 3.13(10^{-3})V_a$, Square: $N = 80$, $V^* = 4.04(10^{-5})V_a$, $V^{**} = 1.04(10^{-3})V_a$, Diamond: $N = 110$, $V^* = 1.38(10^{-5})V_a$, $V^{**} = 4.87(10^{-4})V_a$.

As can be seen in Figure 6.7, the simulated interfacial stress does plateau over roughly the expected range of slip velocities. The vertical lines in the figure mark the values of V^* for the different simulated polymer melts; V^* is the characteristic slip velocity for the beginning of the expected interfacial stress plateau due to interfacial strand alignment. For the simulated polymer melts the stress plateaus begin very near to V^* as shown, in agreement with the theory predictions. An interfacial stress decrease occurs at slip velocities somewhat less than (but on the order of) the expected characteristic disentanglement velocity V^{**}. This stress decrease at lower than expected slip velocities seems to be due to the presence of multiple interfa-

cial entanglements per polymer, and is examined further below. The plateau stress value is 0.1 to 0.2 the value expected from analytic theory, but a reduction of such an amount is in approximate agreement with the reduction in the strand alignment plateau value in Figure 6.5, which was previously discussed. The simulation does not include Rouse-like rubbing friction, so no Rouse-stress regime is present.

In the developed theory of polymer-interfacial stress, the interfacial stress is governed primarily by alignment of interfacial strands, and the number of interfacial strands remaining. From the previous arguments the interfacial stress is expected to be proportional to the product of the interfacial strand alignment and the number of interfacial entanglements remaining (Equation 3.45), and this can be checked by comparing the simulation values for this product to the simulation stress.

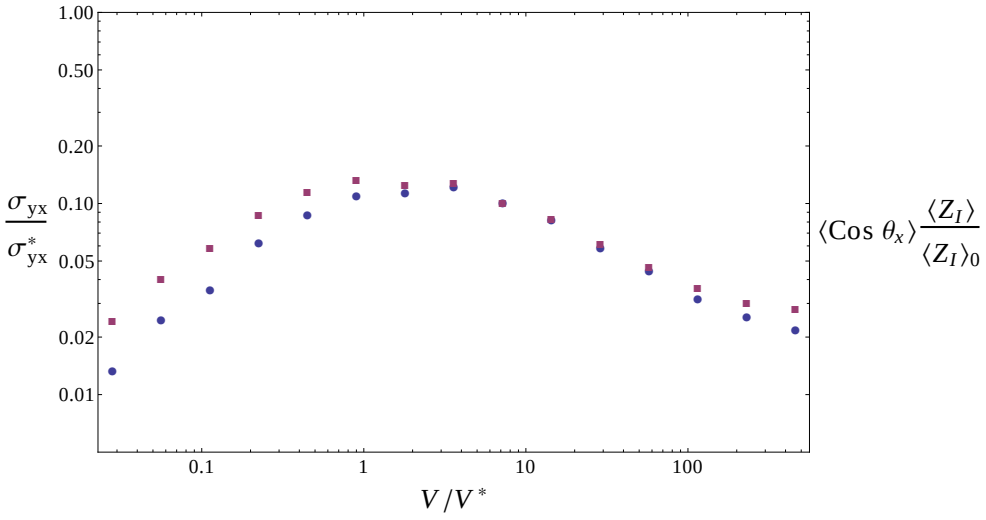

Figure 6.8: Interfacial stress σ_{yx} vs slip velocity V compared to the product of the average interfacial strand alignment and the fraction of interfacial entanglements remaining $\langle \cos\theta_x \rangle \langle Z_I \rangle / \langle Z_I \rangle_0$. Quantities were measured in simulation. Square points are stress values, round points are alignment-entanglement product values. Both axes in logarithmic scale. Simulation parameters: $\beta = 3.125$, $\chi = 0.15$, simulation timestep $\Delta t = 2.56(10^{-5})t_e$.

Figure 6.8 plots both the interfacial stress measured during simulated interfacial

slip, and the product of interfacial strand alignment and the fraction of interfacial slip-links remaining $\langle \cos\theta_x \rangle \langle Z_I \rangle / \langle Z_I \rangle_0$. In the analytic theory the stress increase due to increasing slip velocities is due to the increase in interfacial strand alignment, and the stress decrease at high slip velocities is due to retraction induced interfacial disentanglement. In all regimes the polymer strand tension is expected to be little changed from the equilibrium tension. If the analytic theory is correct then the alignment-entanglement product values in Figure 6.8 should equal the interfacial stress values of $\sigma_{yx}/\sigma^*_{yx}$ plotted in the same figure. As can been seen in Figure 6.8 the product of strand alignment and the number of interfacial entanglements does closely track with the values of the interfacial stress (though with some discrepancy at low slip velocities). This indicates that the interfacial stress is approximately proportional to the alignment-entanglement product as expected, and that the simulated interfacial stress is governed by the alignment of interfacial polymer strands, and the destruction of interfacial entanglements, with interfacial strand tension having approximately the equilibrium value.

A direct comparison between the analytic theory of interfacial stress, and the stress obtained in simulation, is presented in the combination plot below.

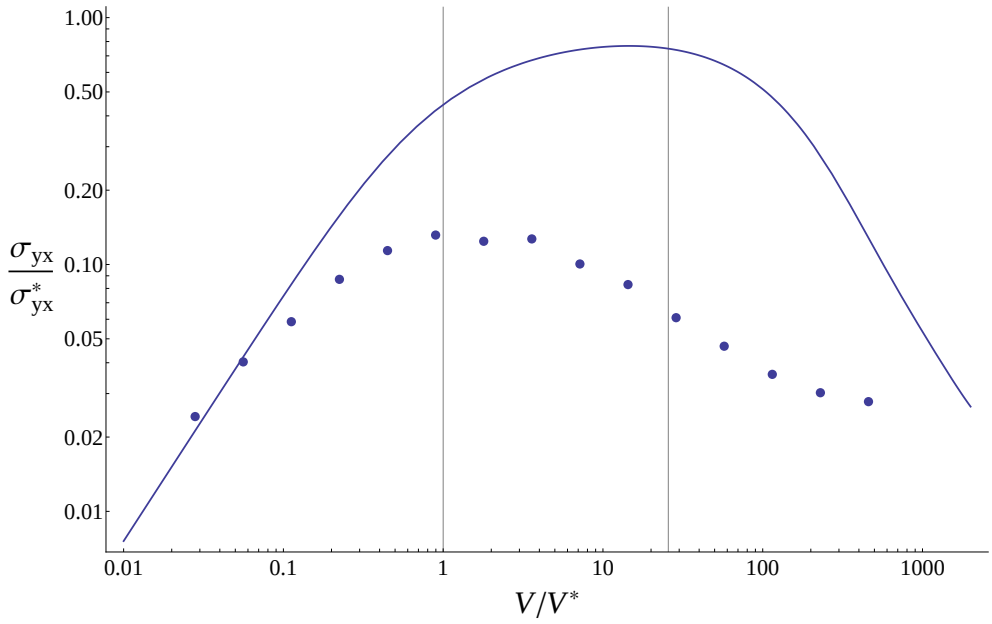

Figure 6.9: Interfacial stress vs. slip velocity, comparison of simulation data and analytic theory. The line is the analytic theory, combining asymptotic solutions and interpolation into a single line (see Figure 3.11). $V^{**} = 25.6V^*$. Simulation parameters: $N = 80$, $\beta = 3.125$, $\chi = 0.15$, simulation timestep $\Delta t = 2.56(10^{-5})t_e$.

In Figure 6.9 it can be seen that the plateau value of the interfacial stress is significantly less in simulation than in the analytic theory. This seems to be due to the low average alignment of interfacial strands in simulation (Figure 6.5), induced by a larger number of young randomly aligned strands, as previously discussed. Additionally, the onset of interfacial entanglement destruction appears to occur at a lower slip velocity than in the analytic theory. However, these predictions of the analytic theory assume that each interfacial polymer will have at most one interfacial entanglement. Upon examining the simulation presented above, it is found that interfacially entangled polymer had on average 3.6 total entanglements. Additional interfacial entanglements per polymer increase the slip induced polymer retraction, and decrease the slip velocity at which entanglement destruction begins to occur, as discussed in section 3.3.2. It is likely that the presence of multiple interfacial entan-

glements per polymer in simulation will tend to cause interfacial disentanglement to occur at a lower slip velocity than predicted by the analytic theory, as anticipated in the analysis of section 3.3.2.

More extensive data was gathered from simulation in order to determine if the interfacial stress behavior and transition velocities were as predicted for polymers of different length. A sampling of this larger data set is presented below.

6.3 Interfacial Slip Simulation Data

In this section data is presented for simulated polymer melts experiencing interfacial slip. Simulations of three polymer lengths are examined over three orders of magnitude of interfacial slip velocities. For each polymer length simulation data for interfacial stress, strand alignment, and interfacial entanglements remaining, are plotted as functions of the interfacial slip velocity. Each plot contains vertical lines marking the values of V^* and V^{**}, the expected characteristic slip velocities of interfacial strand alignment and interfacial entanglement destruction respectively.

For all systems the spatial period (the sum of the $\hat{y}$ direction thickness of both polymer melt layers) was $43.16b$. A polymer having entanglements on both interfaces (opposite interfaces, the system is periodic) was a rare event, and the fraction of timesteps that a polymer had interfacial entanglements on both interfaces was: $N = 50$: $1.9(10^{-3})$, $N = 80$: $7.8(10^{-3})$, $N = 110$: $2.6(10^{-2})$. These fractions were sampled in equilibrium.

6.3.1 Polymer Length: N=50

Polymers that were interfacially entangled had on average 2.92 interfacial entanglements in equilibrium.

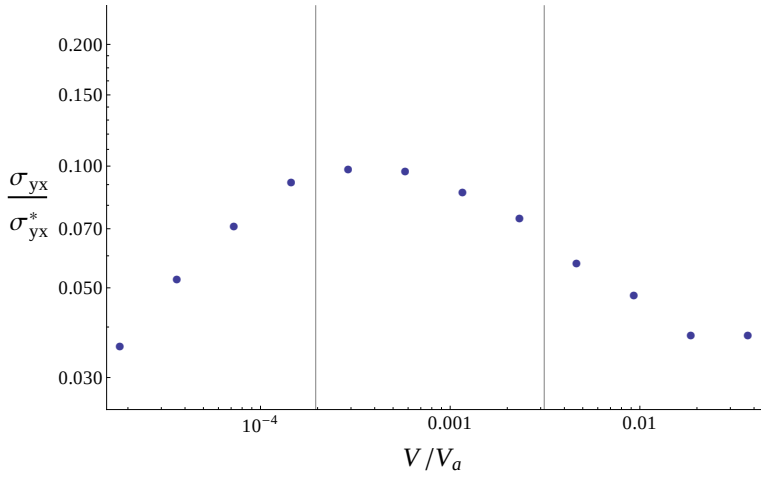

Figure 6.10: Interfacial stress σ_{yx} vs slip velocity V. $N = 50$, Vertical lines correspond to $V^* = 1.96(10^{-4})V_a$, $V^{**} = 3.13(10^{-3})V_a$. Simulation parameters: $\beta = 3.125$, $\chi = 0.15$, simulation timestep $\Delta t = 2.56(10^{-5})t_e$.

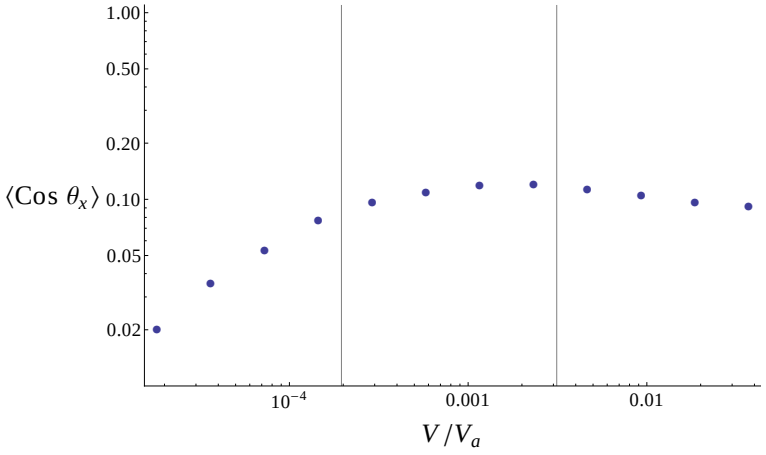

Figure 6.11: Average strand alignment $\langle \cos\theta_x \rangle$ vs slip velocity V. $N = 50$, Vertical lines correspond to $V^* = 1.96(10^{-4})V_a$, $V^{**} = 3.13(10^{-3})V_a$. Simulation parameters: $\beta = 3.125$, $\chi = 0.15$, simulation timestep $\Delta t = 2.56(10^{-5})t_e$.

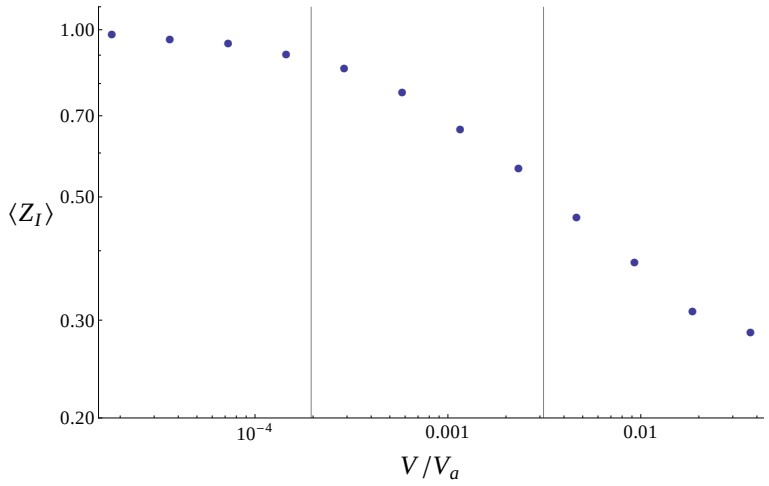

Figure 6.12: Average number of interfacial entanglements per polymer $\langle Z_I \rangle$ vs slip velocity V. $N = 50$, Vertical lines correspond to $V^* = 1.96(10^{-4})V_a$, $V^{**} = 3.13(10^{-3})V_a$. Simulation parameters: $\beta = 3.125$, $\chi = 0.15$, simulation timestep $\Delta t = 2.56(10^{-5})t_e$.

6.3.2 Polymer Length: N=80

Polymers that were interfacially entangled had on average 3.61 interfacial entanglements in equilibrium.

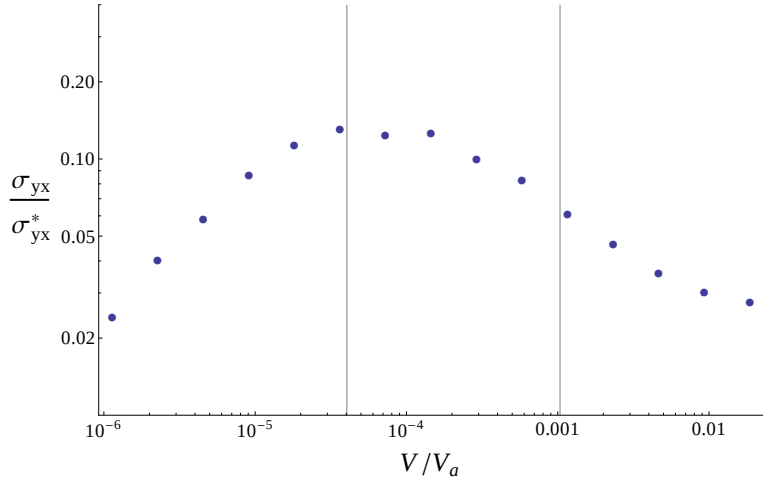

Figure 6.13: Interfacial stress σ_{yx} vs slip velocity V. $N = 80$, Vertical lines correspond to $V^* = 4.04(10^{-5})V_a$, $V^{**} = 1.04(10^{-3})V_a$. Simulation parameters: $\beta = 3.125$, $\chi = 0.15$, simulation timestep $\Delta t = 2.56(10^{-5})t_e$.

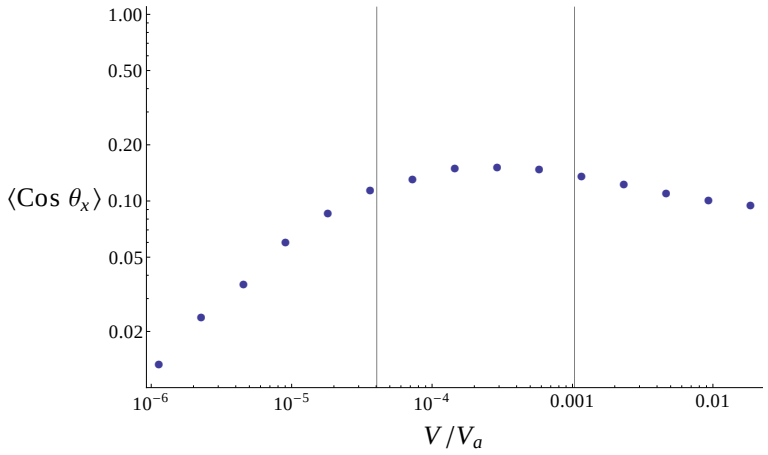

Figure 6.14: Average strand alignment $\langle \cos \theta_x \rangle$ vs slip velocity V. $N = 80$, Vertical lines correspond to $V^* = 4.04(10^{-5})V_a$, $V^{**} = 1.04(10^{-3})V_a$. Simulation parameters: $\beta = 3.125$, $\chi = 0.15$, simulation timestep $\Delta t = 2.56(10^{-5})t_e$.

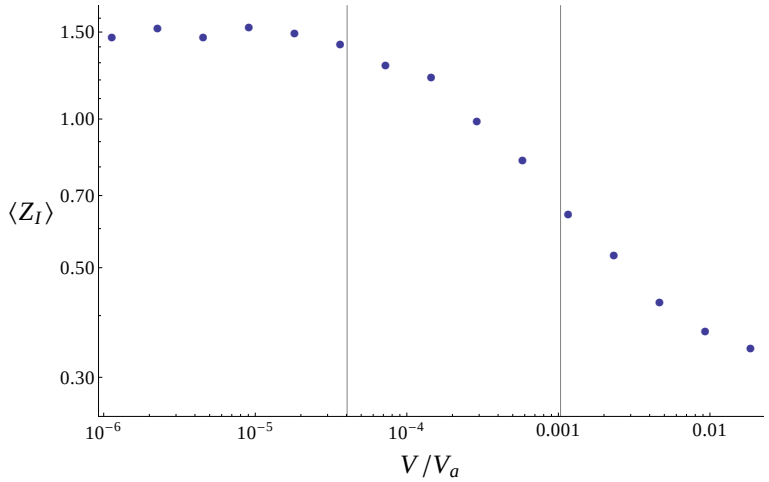

Figure 6.15: Average number of interfacial entanglements per polymer $\langle Z_I \rangle$ vs slip velocity V. $N = 80$, Vertical lines correspond to $V^* = 4.04(10^{-5})V_a$, $V^{**} = 1.04(10^{-3})V_a$. Simulation parameters: $\beta = 3.125$, $\chi = 0.15$, simulation timestep $\Delta t = 2.56(10^{-5})t_e$.

6.3.3 Polymer Length: N=110

Polymers that were interfacially entangled had on average 4.29 interfacial entanglements in equilibrium.

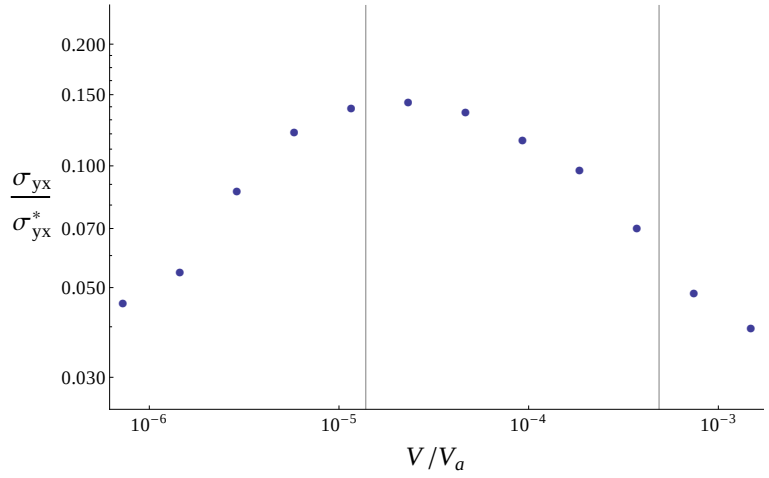

Figure 6.16: Interfacial stress σ_{yx} vs slip velocity V. $N = 110$, Vertical lines correspond to$V^* = 1.38(10^{-5})V_a$, $V^{**} = 4.87(10^{-4})V_a$. Simulation parameters: $\beta = 3.125$, $\chi = 0.15$, simulation timestep $\Delta t = 2.56(10^{-5})t_e$.

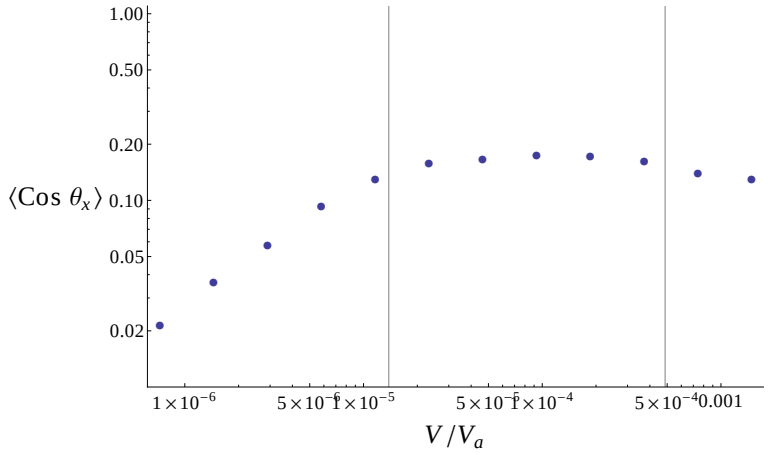

Figure 6.17: Average strand alignment $\langle \cos \theta_x \rangle$ vs slip velocity V. $N = 110$, Vertical lines correspond to$V^* = 1.38(10^{-5})V_a$, $V^{**} = 4.87(10^{-4})V_a$. Simulation parameters: $\beta = 3.125$, $\chi = 0.15$, simulation timestep $\Delta t = 2.56(10^{-5})t_e$.

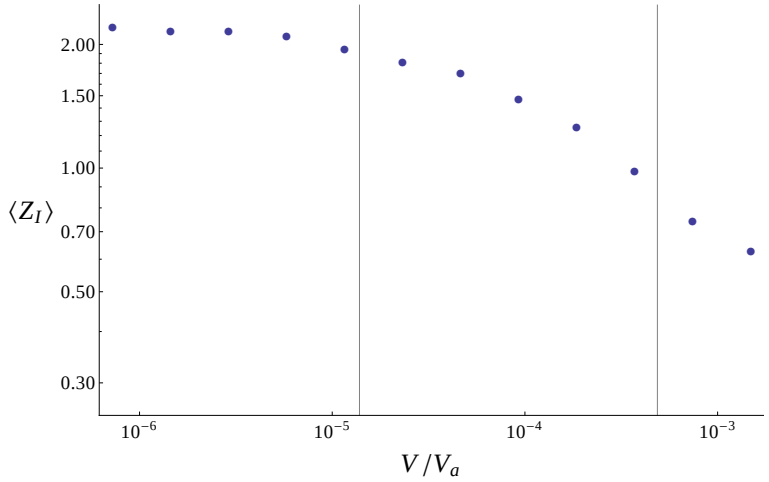

Figure 6.18: Average number of interfacial entanglements per polymer $\langle Z_I \rangle$ vs slip velocity V. $N = 110$, Vertical lines correspond to$V^* = 1.38(10^{-5})V_a$, $V^{**} = 4.87(10^{-4})V_a$. Simulation parameters: $\beta = 3.125$, $\chi = 0.15$, simulation timestep $\Delta t = 2.56(10^{-5})t_e$.

6.4 Summary

A dynamic Monte Carlo simulation of polymer-polymer interfacial slip which used a self-consistent field description of polymer-polymer interfaces was performed. The simulation results were compared to the analytic theory of interfacial slip. An interfacial stress plateau was found to occur beginning at slip velocities of approximately $V^* = a/t_{rep}$ (the characteristic velocity of interfacial strand alignment) as expected. Interfacial disentanglement was found to occur at larger slip velocities, with longer polymers having higher lower disentanglement velocities, as expected. The disentanglement slip velocities observed in simulation were somewhat reduced from the predicted disentanglement slip velocity of $V^{**} = L/t_{rep}$. This effect may be due to increased polymer retraction caused by multiple interfacial entanglements per polymer in simulation. The characteristic strand alignment and interfacial disentanglement behavior appeared to have approximately the predicted scaling dependence on polymer length, as evidenced by V^* and V^{**} retaining their predictive significance for simulated polymers of different length undergoing interfacial slip. The observed interfacial stress plateau value was approximately 0.1 to 0.2 the predicted value of σ^*_{yx}. This reduced plateau stress seems to have been primarily due to the constant presence of newly entangled polymer strands, which were randomly aligned, and diluted the overall interfacial strand alignment. The product of interfacial strand alignment and the fraction of interfacial entanglements remaining was found to track closely with interfacial stress, when plotted in units of the plateau stress σ^*_{yz}, as expected (Figure 6.8). This indicates that slip induced polymer-polymer interfacial stress between entangled polymer melts was governed by interfacial strand alignment, and interfacial entanglement destruction, with strands having approximately equilibrium tension, as predicted by the analytic model of interfacial slip.

Chapter 7

Experimental Comparison

In order to examine the phenomenon of polymer-polymer interfacial slip some experiments have been performed by different research groups. These experiments are described below, with comparison to the model theoretical predictions when applicable. A number of the experiments focused solely on verifying the presence of stress induced interfacial slip between polymer melts, while others attempted to determine a quantitative relationship between the interfacial stress and the slip velocity. Some of the interfacial slip experiments were done with the goal of using polymer-polymer interfacial slip to increase polymer melt extrusion rates (coating extrusion machine parts in a secondary polymer substance to decrease interfacial friction). Such extrusion oriented experiments tended to focus on very high slip velocities, outside the realm of application of the theory developed in this work. Currently there is little experimental data regarding the polymer-polymer interfacial slip / stress relationship in the slip velocity regimes this theory references.

Lam et al. [20] performed an experimental analysis of slip at an interface between high density polyethylene (HDPE) and polystyrene (PS). Their experiments were performed at a single applied shear strain rate to a pair of rectangular HDPE/PS

melts pressed together (planar interface). The experiments used confocal microscopy to track the motions of steel beads embedded in the melts. They found a velocity discontinuity at the interface between the melts, indicating that slip between the melts did occur. Their experiments resolved only a single interfacial slip velocity due to the use of one applied strain rate.

Similarly, Zartman et al. [22] performed a series of experiments examining polymer-polymer interfacial slip in which particles embedded in the melts were tracked. Their experiments used two pairs of immiscible polymer melts (styrene butadiene rubber and polyisoprene, and polydimethylsiloxane and polyisoprene) sharing a planar interface, and tracked the melt velocity profiles during an imposed startup shear. Their experiments found velocity discontinuities at the polymer-polymer interfaces, indicating slip. However, their experiments were primarily focused on determining polymer melt velocity profiles, including the presence of slip, and how slip developed in time during a startup shear deformation, rather than on the stress / slip velocity relationship.

Yang and White performed an experiment on extrusion speeds of polyamide 12 (PA12) in which the walls of the capillary die extruder were coated with ethylene butene copolymer (EBM) [167]. It was found that with the coating present extruder speeds could be much increased compared to the non-coated case. The faster extrusion speeds seemed to be due to easy slippage between the melts, and data was obtained for the slip velocity as a function of interfacial stress. However, the experimenters were interested in obtaining high extrusion speeds, and the slip velocities were many orders of magnitude larger than the characteristic slip velocities in the theory of entangled interfaces (theoretical characteristic velocities being generally less than 1 μ m/s, while this experiment studied slip velocities in the tens of mm/s).

Son performed an experiment in which he verified that the negative viscosity

deviation (lower than expected total viscosity) of layers of layers of polypropylene (PP) and polyamide 6 (PA6) is due to slip at the interfaces between the layers [168]. He verifies the existence of slip, but does not determine a detailed stress / slip velocity relationship.

Komuro et al. studied slip at the interfaces between polystyrene (PS) and polypropylene (PP) melts in a three layer flow experiment (one PS polymer melt being pushed through the gap between two fixed PP polymer melts, and vice versa). They verified the existence of slip between the polymer melts, and obtain interfacial stress / slip velocity relationships, but for slip velocities much higher than those referenced by the theory in this work (their experiment focused on slip velocities larger than 1 mm/s).

Recently, the Macosko group at the University of Minnesota, and collaborators, have performed some slip / stress experiments on planar layers of immiscible polymer melts. These experiments include data for the interfacial slip velocities at different applied stresses, and thus currently provide the best data for comparison to the theory developed in this work. However, the experiments are technically difficult, with different behavior being observed in different velocity regimes and for different polymer species pairs. Most of the experiments performed so far have been able to resolve only slip velocities much higher than the characteristic slip velocities predicted by the theory developed here, at which it is expected that the interfaces will not be entangled. A unifying picture of the experimental interfacial slip / stress relationship has not yet emerged.

Zhao and Macosko performed a series of slip experiments on co-extruded polymer melt layers [19]. In the experiments polymer melts composed of alternating layers of immiscible polymer species were subjected to rheological measurements in both a pressure driven slit rheometer, and a parallel plate rheometer. Pressure drop measurements in the slit rheometer, and stress measurements in the parallel plate rheometer,

were used to determine slip velocity values at the interfaces between the immiscible polymer species. In these experiments the primary polymer-polymer interface studied was between melts of polypropylene (PP) and polystyrene (PS). These melts are highly immiscible, with the interfacial width $w = 2.4$ nm being less than the average entanglement distance $a = 6.8$ nm. Consequently it is thought that the interfacial region between the melts was not strongly entangled, and for this reason this experiment might not be suitable for comparison to the theory developed in this work (the theory focuses on stress transmitted by interfacial entanglements). Nevertheless, some of the interfacial slip velocities sampled in these experiments fall within the range of the theory, and the data is reproduced below.

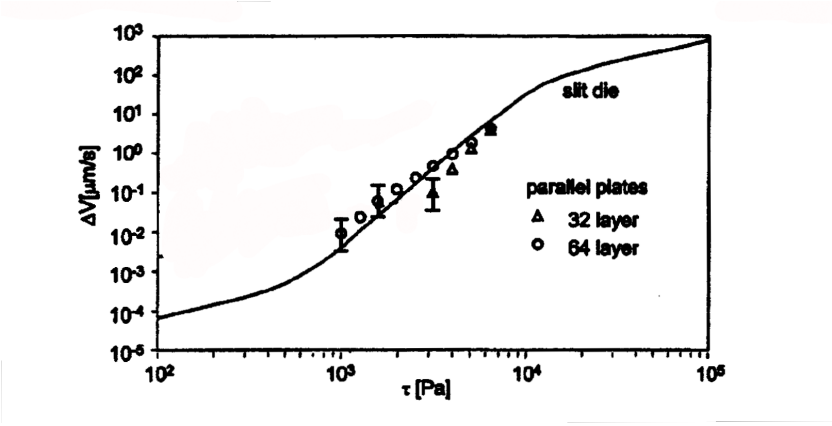

Figure 7.1: Experimental data obtained by Zhao and Macosko [19] for interfacial slip velocity (μm/s) vs. interfacial stress (Pa). Reprinted with permission from *Journal of Rheology*, 46(1):145-167, 2001. Copyright 2001, The Society of Rheology. Both axes in logarithmic scale. Solid line data obtained via pressure drop measurements, point data obtained via stress measurements on parallel plates [19]. The experiment was performed by Zhao and Macosko in the Department of Chemical Engineering and Materials Science at the University of Minnesota, using planar layers of polypropylene and polystyrene subject to a tangential stress provided by the mechanical action of a metallic plate.

Table 7.1: Polypropylene / Polystyrene Melt Parameters from Zhao and Macosko

Species	η_0(kPa s)	$G_N^{(0)}$(kPa)	a(nm)	L(nm)	t_{rep}(s)	V^*(mm/s)	V^{**}(mm/s)
PP	8.1	430	6.8	73.2	0.0229	2.97E−4	3.20E−3
PS	7.2	150	6.8	52.3	0.0584	1.17E−4	8.96E−4

The shown entanglement lengths (a) and path lengths (L) for PP and PS are from parameters given by Macosko et al. [17, 19]. The reptation times are calculated from the viscosity η_0 and plateau modulus $G_N^{(0)}$ given by Macosko et al. [17, 19] and shown above, using the relation $t_{rep} = 12\eta_0/(\pi^2 G_N^{(0)})$ [36]. The theory developed in this work predicts an interfacial stress plateau between the characteristic slip velocities V^* and V^{**}. As can be seen in the results of Zhao and Macosko, an increase in the scaling of the interfacial slip velocity with the interfacial stress is found, though the not a strict plateau. The velocity region of steep dependence is wider than the theoretical velocity region expected for a stress plateau. Because the melts are thought to be weakly entangled it is not clear if the theory for entangled polymer-polymer interfaces is applicable. One indicator that the interface is not significantly entangled in the sampled regime is the fact that the interfacial stress values fall between 1 and 10 kPa, which is orders of magnitude less than the plateau modulus values $G_N^{(0)}$ for both melts; if the interface was significantly entangled in this regime an interfacial stress closer to the plateau modulus would be expected.

In the experiments performed by Lee, Park, Morse, and Macosko [17] slip at interfaces between polypropylene (PP) and polystyrene (PS) melts, as well as between polyethylene (PE) and fluoropolymer (FP) melts, was studied. In the experiments some data indicate a regime in which the slip velocity quickly increases with interfacial stress (a somewhat plateau-like regime), however, the interfacial slip velocities studied in these experiments are multiple orders of magnitude above the characteristic slip

velocities predicted by the theory developed in this work. Lee et al. state that the methods used in these experiments cannot resolve slip velocities below 1μ m / s [17], consequently the slip behavior observed in these experiments is in an entirely different slip velocity regime than is applicable to the developed theory, and the theory would predict that at such high slip velocities the interfaces are not significantly entangled. Additionally, these systems are again highly immiscible, meaning that few interfacial entanglements would be expected even at lower slip velocities.

Park, Lee, and Macosko [18] performed a series of experiments similar to Lee, Park, Morse, and Macosko [17], but used a combination of visualization and stress reduction to determine interfacial slip, and focused exclusively on interfaces between polyethylene (PE) and fluoropolymer (FP). These experiments obtained similar results to Lee, Park, Morse, and Macosko, and were likewise focused on high slip velocity regimes (greater than 1μ m/s), outside the realm of applicability of the developed theory.

Zhang, Lodge, and Macosko, studied how interfacial slip affects adhesion between polymer layers [11]. In their experiment layers of polystyrene and poly methyl methacrylate were subjected to tangential stress forces, and then their adhesion (the force required to pry them apart) was measured. For large enough applied tangential stress forces they find a reduction in adhesion between the layers. Pressure measurements indicate slip between the layers during the application of tangential stress, and they interpret the adhesion reduction as being due to slip induced interfacial disentanglement.

Recently, some experimental data (not yet published) for the interfacial stress / slip velocity relationship partially in the regime applicable to the theory has been obtained by Heon E. Park at McGill University in collaboration with the Macosko group at the University of Minnesota. The data obtained is for slip at an interface between polybutadiene (PB) and polystyrene (PS) melts, and the experimental method used

was similar to the stress reduction method of Park, Lee, and Macosko [18] in which stress measurements in a parallel plate rheometer were used to determine interfacial slip velocities between polymer species layers. For this polymer pair the interfacial width and average entanglement distance are roughly equal $w/a \approx 1$, resulting in the possibility of larger interfacial entanglement than some of the previous polymer species pairs. Interestingly, the data indicate the presence an interfacial stress plateau over a range of interfacial slip velocities. As a stress plateau is a qualitative phenomenon expected in the theory of polymer-polymer interfacial slip, the experimental data is here more closely examined.

Below is a plot of stress vs. interfacial slip velocity data obtained through a series of experiments by Lee.

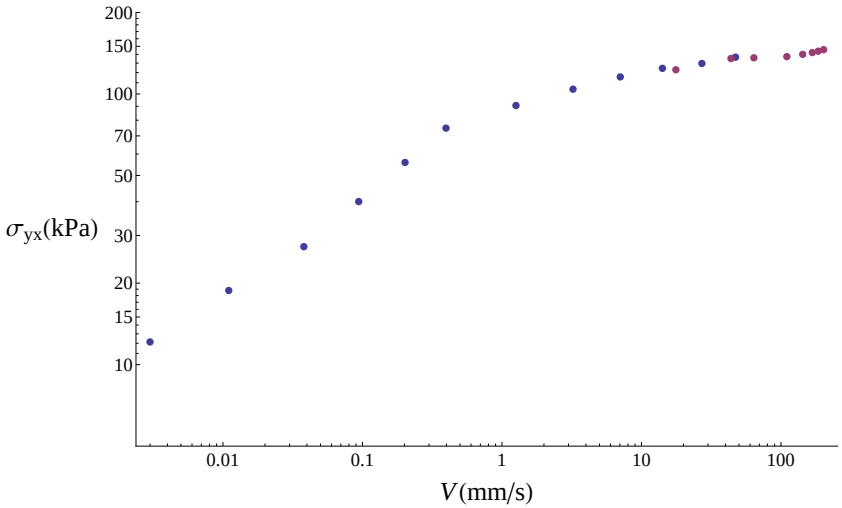

Figure 7.2: Experimental data for interfacial stress (kPa) vs. interfacial slip velocity (mm/s). Both axes in logarithmic scale. The experiment was performed by Heon E. Park at McGill University in collaboration with the Macosko group at the University of Minnesota, and the data is reproduced with their permission. The experiment used planar layers of polystyrene and polybutadiene subject to a tangential stress provided by the mechanical action of a metallic plate.

Table 7.2: Polybutadiene / Polystyrene Melt Parameters from Park

Species	η_0(kPa s)	$G_N^{(0)}$(kPa)	a(nm)	L(nm)	t_{rep}(s)	V^*(mm/s)	V^{**}(mm/s)
PB	44.19	1100	4.1	506.4	0.049	8.4E−5	1.0E−2
PS	33.25	208	8.52	50.41	0.194	4.4E−5	2.6E−4

In this table the viscosity η_0 and the plateau modulus $G_N^{(0)}$ were determined via rheological measurements, and the reptation times t_{rep} were calculated using the relation $t_{rep} = 12\eta_0/(\pi^2 G_N^{(0)})$ [36].

The stress / slip velocity data in Figure 7.2 does show the stress entering a plateau region, in qualitative agreement with what is expected in the theory of interfacial slip of entangled polymer-polymer interfaces. However, when comparing the slip velocity at which the stress plateau begins (≈ 1 mm/s) to the characteristic slip velocities V^* and V^{**} listed in the table, it is found that the stress plateau begins at a slip velocity nearly two orders of magnitude above the largest characteristic disentanglement slip velocity V^{**} ($1.0(10^{-2})$mm/s, PB). The characteristic disentanglement velocity V^{**} is the velocity at which the model would predict that the stress plateau would be ending due to interfacial entanglement depletion; the model predicts that the stress plateau would begin at the characteristic alignment velocity V^*, but in the experimental data the characteristic alignment velocities are V^* are four to five orders of magnitude smaller that the interfacial slip velocity at which the stress plateau begins.

Because of the disagreement in the velocity scale for the onset of the interfacial stress plateau, the interfacial slip model indicates that the stress plateau phenomenon observed in the experimental data is not the result of any classical entanglement phenomenon (one in which reptation is the key mechanism). The analytic model strongly indicates that at the experimentally sampled slip velocities the polymer-polymer interfaces are disentangled (in the classical sense). Perhaps the simplest

argument for this conclusion is the following dimensional argument:

Phenomena resulting from classical entanglement are governed by the characteristic timescale of the reptation time (by definition). The reptation times for these polymer melts are listed in the table above. In this physical system there are only a few characteristic length scales, including the entanglement distance a, the interfacial width w, and the polymer primitive path length L. Using these characteristic length scales in conjunction with the reptation time, the largest constructable characteristic velocity is $V^{**} \equiv L/t_{rep}$, which remains two orders of magnitude below the observed stress plateau slip velocity. The characteristic strand alignment slip velocity $V^* \equiv a/t_{rep}$ is four orders of magnitude below the stress plateau interfacial slip velocity. It is extremely difficult to impossible to see how any model based on reptation could bridge these velocity differences and predict a stress transition slip velocity at the observed value. For this reason I conclude that the interfacial stress plateau observed in experiment is not governed by polymer reptation, and at the measured slip velocities the interface is not classically entangled.

There is another possibility for the origin of the stress plateau in Park's interfacial slip / stress data. The of velocity of the onset of the interfacial stress plateau is somewhat closer to the average entanglement distance a divided by the entanglement length Rouse time $V_R^* = a/t_{aR}$ for the PS melt (which has the lower of the two V_R^* values). The entanglement length Rouse time is the time an unentangled polymer section of path length a (or monomer count N_e) would take to equilibrate, and is related to the reptation time by $t_{aR} = (a/L)^3 t_{rep}/3$ [36]. For the PS melt $V_R^* = 0.03$ mm/s. V_R^* is the characteristic slip velocity at which unentangled polymers sections of arc-length equal to the entanglement length would become significantly aligned in the direction of slip. Thus, it is possible that an orientation transition of unentangled PS polymer subsections near the interface takes place at slip velocity V_R^*, and that this

orientational transition leads to a non-linearity in the stress response. These polymer subsections would be unentangled in the classical sense, so as to directionally relax via unentangled diffusion (Rouse-like motion), though they might still have limited local topological interactions (loop-level non-passing interactions) with the surrounding polymers. This is a hypothesis that remains to be further tested. If such a process does lead to a non-linearity it would need to be determined if two such orientational transitions occurred when the two melts had different values of V_R^*, and how this would manifest in the stress response.

In total, the experimental picture of polymer-polymer interfacial slip remains rather murky. Though experiments have verified the occurrence of interfacial slip, most of the experiments performed thus far which attempted to determine a relationship between the interfacial stress and slip velocity have sampled slip velocities much larger than the characteristic slip velocities of the theory that has been developed here. The theory predicts that at such high slip velocities the interface between the polymer melts would be primarily unentangled (in the classical sense), and that the interfacial stress would be the result of Rouse-like rubbing friction, or other sub-section topological interactions. The experimental difficulty in accessing lower interfacial slip velocities for entangled polymer melts means that it is not currently possible to gain a more thorough experimental comparison of the developed theory of polymer-polymer interfacial slip.

Chapter 8

Summary and Conclusions

In this work a theoretical examination of slip at entangled interfaces between immiscible polymer melts was made. This was accomplished by developing a mathematical theory of polymer-polymer interfacial slip, and by constructing a computer simulation of interfacial slip at polymer-polymer interfaces. The mathematical theory of interfacial slip made predictions regarding the relationship between the interfacial stress and the interfacial slip velocity. The predictions of the mathematical theory were compared to the computer simulation results, as well as to experimental data.

In both the mathematical theory and the simulation the situation considered was that of "perfect" slip (constant velocity translation) at a planar interface between two immiscible polymer melts having identical physical parameters (identical polymer lengths, average distance between entanglements, etc.). The main focus of both analyses was to determine the relationship between the interfacial stress and the interfacial slip velocity, and the mechanisms affecting this relationship.

The mathematical theory of polymer-polymer interfacial slip predicts characteristic interfacial slip velocities at which the interfacial slip-stress relationship qualitatively changes. The characteristic slip velocity $V^* = a/t_{rep}$ is the slip velocity at

which it is predicted that interfacially entangled polymer strands become primarily aligned in the slip direction (here a is the average distance between entanglements, and t_{rep} is the reptation time). The characteristic slip velocity $V^{**} = L/t_{rep}$ is the slip velocity at which it is predicted the polymer-polymer interface becomes significantly disentangled (L being the total polymer primitive path length). Both of these characteristic slip velocities are governed by the reptation time $t_{rep} \sim \zeta L^3/(\mathrm{k_B}T)$, which is the time needed for an entangled polymer to equilibrate. Taking the length dependence of the reptation time into account, these characteristic slip velocities have different scaling with respect to polymer length, with $V^* \propto a/L^3$ and $V^{**} \propto 1/L^2$. For strongly entangled polymers with the average entanglement distance much less than the total polymer path length ($a \ll L$), V^* and V^{**} will be widely separated with $V^* \ll V^{**}$.

In the developed mathematical theory of interfacial slip, interfacial stress is affected by the number of interfacially entangled polymer strands, the tension in the interfacially entangled strands, and the alignment of the interfacially entangled strands. Additionally, a Rouse-like rubbing friction contribution to interfacial stress is considered to be present. By modeling interfacial entanglements as slip-links it was possible to make a stochastic / mechanical analysis of the population of interfacial entanglements, and the interfacial stress transmitted by interfacial entanglements at different slip velocity scales. The results of this analysis indicate that during slip the interfacial strand tension is never significantly perturbed from the thermal equilibrium strand tension $\tau_0 = 3\mathrm{k_B}T/a$. As a result, changes in the interfacial stress transmitted by entanglements are primarily governed by the slip-induced alignment of interfacial strands having approximately equilibrium tension, and the destruction of interfacial entanglements due to slip-induced polymer retraction.

For low slip velocities ($V < V^*$) interfacial stress is expected to increase with

increasing slip velocity as larger slip velocity causes the interfacial strands to be more aligned in the direction of slip. For slip velocities above V^* the interfacial strands are expected to be nearly aligned in the direction of slip, and thus further stress increase due to strand alignment is impossible. At slip velocities above V^{**} slip-induced polymer retraction is expected to result in significant interfacial disentanglement, and consequently a reduction in interfacial stress due to interfacial entanglement loss is expected for slip velocities larger than V^{**}. A stress plateau is expected for interfacial slip velocities between V^* and V^{**}; in this regime interfacial strands are expected to be nearly aligned in the direction of slip, but slip-induced polymer retraction is not yet expected to result in a significant reduction in the number of interfacial entanglements from the equilibrium number. The contribution of Rouse-like rubbing friction to interfacial stress is expected to become dominant only for slip velocities significantly larger than V^{**} where the interface has become disentangled. The entire interfacial slip-stress relationship as predicted by the mathematical theory is shown in Figure 3.11.

To test the predictions of the mathematical theory of interfacial slip a computational simulation of polymer-polymer interfacial slip was constructed. The simulation used a dynamic Monte Carlo algorithm, and a description of polymer entanglements as slip-links (based on the model of Schieber et al. [145–157]) to simulate entangled polymers. This simulation used physically motivated move transition probabilities, and successfully reproduced certain realistic dynamics and rheological responses as outlined in Chapter 4. To simulate polymer-polymer interfaces a self-consistent field description of the interface was used, in which the average free energy interactions near a polymer-polymer interface are expressed as a self-consistently determined chemical potential. The simulated polymers were informed of the chemical potential field through polymer strand Green functions (statistical weights) that were numerically

calculated within the chemical potential field. This is the first instance (to my knowledge) of a slip-link polymer simulation using a self-consistent field to influence polymer behavior. The simulation exhibited the slip-link spatial profiles that were expected within the chemical potential field, indicating the in-field simulation functioned as expected.

To simulate interfacial slip, slip-links were assigned species identities based on spatial position so that they represented either like-species or other-species entanglements (identities were assigned probabilistically based on the local species volume fraction at the point of slip-link creation). Other-species entanglements were more likely to be formed at the interface, and represented entanglements between the polymer melts. To simulate interfacial slip the slip-links of one species were translated parallel to the interface at constant velocity relative to the slip-links of the other species. The steady state stress response at the interface was observed as a function of slip velocity.

For low slip velocities the simulated interfacial stress increased with slip velocity, until a plateau was reached at a slip velocity of approximately V^* as expected. Simulation data for the interfacial strand alignment showed that there was an alignment transition at this slip velocity (the alignment plateaus). A stress plateau region was then observed in the simulation data, until a stress decrease begins at high slip velocities, which is caused by interfacial disentanglement (indicated by a reduction in the number of interfacial entanglements in simulation). The stress decrease in simulation happened at a slip velocity somewhat lower than, but on the order of, the predicted slip velocity of V^{**}. This decrease at lower slip velocity may be due to increased polymer retraction caused by multiple interfacial entanglements per polymer. Perhaps the best comparison between the predicted stress response and the simulated is in Figure 6.8 in Chapter 6. In this figure a comparison of the product of strand alignment

and number of slip-links remaining (multiplied by a fit constant) is compared to the interfacial stress as a function of slip velocity. The mathematical theory of interfacial slip predicts that the interfacial stress will be proportional to this product, and this prediction is born out in simulation by the agreement of the data in this figure.

A comparison to experimental data of interfacial slip stress response was additionally made. There is little experimental data for polymer-polymer interfacial slip / stress relationships in the velocity regime of this theory. The recent data obtained by Heon Park shows some indication of a stress plateau, as qualitatively expected, but the plateau occurs at an interfacial slip velocity much larger than those treated in this theory of interfacial slip. For this reason it is concluded that the experimentally observed behavior is due to another phenomenon outside the range of this theory. It is possible that the stress plateau observed by Park is due to an alignment transition of unentangled polymer subsections, but this hypothesis remains to be tested. This theory predicts that a stress plateau at lower slip velocities exists, and if these lower slip velocity ranges for entangled polymer-polymer interfaces ever become more experimentally accessible this prediction can be further tested.

In conclusion, the developed theory of interfacial slip at entangled polymer-polymer interfaces predicts that interfacially entangled strands become nearly aligned at slip velocities above V^*, and that the interface becomes disentangled at slip velocities above V^{**}. Interfacial stress is predicted to be governed primarily by interfacial strand alignment, and the number of interfacial entanglements remaining (polymer strand tension is expected to be little altered from its thermal equilibrium value). Consequently, a stress plateau is expected for interfacial slip velocities between V^* and V^{**}. The constructed simulation of interfacial slip supports these predictions, exhibiting a stress plateau over approximately the slip velocities predicted, and indicating that interfacial stress is governed primarily by interfacial strand alignment

and the number of existing interfacial entanglements. Though experiments on this topic have been performed, none have yet sampled the slip velocity regimes relevant to these predictions for entangled polymer-polymer interfaces.

Bibliography

[1] P. G. de Gennes. Reptation of a polymer chain in the presence of fixed obstacles. *Journal of Chemical Physics*, 55(2), 1971.

[2] Susan E. M. Selke. *Understanding Plastics Packaging Technology.* Hanser/Gardner Publications, Inc., 1997.

[3] Michael F. Weber, Carl A. Stover, Larry R. Gilbert, Timothy J. Nevitt, and Andrew J. Ouderkirk. Giant birefringent optics in multilayer polymer mirrors. *Science*, 287(5462):2451–2456, 2000.

[4] L. A. Utracki and M. R. Kanial. Melt rheology of polymer blends. *Polymer Engineering & Science*, 22(2):96–114, 1982.

[5] L. A. Utracki. Melt flow of polymer blends. *Polymer Engineering & Science*, 23(11):602–609, 1983.

[6] N. P. Adhikari and J. L. Goveas. Effects of slip on the viscosity of polymer melts. *Journal of Polymer Science*, 42:1888–1904, 2004.

[7] Arie Cohen and John R. Schroeder. Morphological analysis of the viscosity anomaly for pp/ps blends. *Journal of Rheology*, 34(5), 1990.

[8] Chen-Chong Lin. A mathematical model for viscosity in capillary extrusion of two-component polyblends. *Polymer Journal*, 11(3):185–192, 1979.

[9] Jan-Chan Huang, Hsiao-Fu Shen, and Ying-Ti Chu. Melt viscosity of polycarbonate-polyolefin blends. *Advances in Polymer Technology*, 13(1):49–55, 1994.

[10] K. B. Migler, C. Lavalee, M. P. Dillon, S. S. Woods, and C. L. Gettinger. Visualizing the elimination of sharkskin through fluoropolymer additives: Coating and polymer-polymer slippage. *Journal of Rheology*, 45(2), 2001.

[11] Jianbin Zhang, Timothy P. Lodge, and Christopher W. Macosko. Interfacial slip reduces polymer-polymer adhesion during coextrusion. *Journal of Rheology*, 50(1):41–57, 2006.

[12] S. A. Patlazhan and I. V. Kravchenko. Influence of interfacial slip on mechanical adhesion of immiscible polymers. *Journal of Adhesion Science and Technology*, 25(12):1425–1434, 2011.

[13] Barry A. Morris. The effect of processing variables on peel strength performance in coextrusion blown film. *Conference Proceedings: Society of Plastics Engineers, 1996*, 1:116–120, 1996.

[14] Eonseok Lee and James L. White. Basic study of the interaction of thermoplastic fluoropolymer blends with metal surfaces during extrusion. *Journal of the Society of Rheology, Japan*, 29(39):39–45, 2001.

[15] L. Levitt and C. W. Macosko. Shearing of polymer drops with interfacial modification. *Macromolecules*, 32, 1999.

[16] C. C. Park, F. Baldessari, and L. G. Leal. Study of molecular weight effects on coalescence: Interface slip layer. *Journal of Rheology*, 47:911–942, 2003.

[17] Patrick C. Lee, Hee Eon Park, David C. Morse, and Christopher W. Macosko. Polymer-polymer interfacial slip in multilayered films. *Journal of Rheology*, 53(4):893–915, 2009.

[18] Heon E. Park, Partick C. Lee, and Christopher W. Macosko. Polymer-polymer interfacial slip by direct visualization and by stress reduction. *Journal of Rheology*, 54, 2010.

[19] Rui Zhao and Christopher W. Macosko. Slip at polymer-polymer interfaces: Rheological measurements on coextruded multilayers. *Journal of Rheology*, 46(1):145–167, 2001.

[20] Y. C. Lam, L. Jiang, C. Y. Yue, K. C. Tam, and L. Li. Interfacial slip between polymer melts studied by confocal microscopy and rheological measurements. *Journal of Rheology*, 47(3):795–807, 2003.

[21] Hongbo Zeng, Yu Tian, Boxin Zhao, Matthew Tirrell, and Jacob Israelachvili. Friction at the liquid/liquid interface of two immiscible polymer films. *Langmuir*, 25(9):4954–4964, 2009.

[22] Gregory D. Zartman and Shi-Qing Wang. A particle tracking velocimetric study of interfacial slip at polymer-polymer interfaces. *Macromolecules*, 44:9814–9120, 2011.

[23] L. Jiang, Y. C. Lam, and J. Zhang. Rheological properties and interfacial slip of a multilayer structure under dynamic shear. *Journal of Polymer Science B*, 43:2683–2693, 2005.

[24] Hiroshi Furukawa. Sliding along the interface of strongly segregated polymer melts. *Physical Review A*, 40(11), 1989.

[25] P. G. de Gennes. *C. R. Acad. Sci. Ser II*, 308(1401), 1989.

[26] F. Brochard-Wyart, P. G. de Gennes, and S. Troian. *C. R. Acad. Sci.*, 310(1169), 1990.

[27] P. G. de Gennes and ed. I. C. Sanchez. *Physics of Surfaces and Interfaces*. Butterworth-Heinmann, Boston, 1992.

[28] Prince E. Rouse. A theory of the linear viscoelastic properties of dilute solutions of coiling polymers. *Journal of Chemical Physics*, 21(7), 1953.

[29] J. L. Goveas and G. H. Fredrickson. Apparent slip at a polymer-polymer interface. *European Physical Journal B*, 2(79), 1998.

[30] Sandra Barsky and Mark O. Robbins. Molecular dynamics study of slip at the interface between immiscible polymers. *Physical Review E*, 63(021801), 2001.

[31] Sandra Barsky and Mark O. Robbins. Bulk and interfacial shear thinning of immiscible polymers. *Physical Review E*, 65(021808), 2002.

[32] Dai, Minn, Satyanarayana, Sinha, and Tan. Identifying the mechanisms of polymer friction through molecular dynamics simulation. *Langmuir*, 27:14861–14867, 2011.

[33] Tak Shing Lo, Maja Mihajlovic, Yitzhak Shnidman, Wentao Li, and Dilip Gersappe. Interfacial slip in sheared polymer blends. *Physical Review E*, 72(040801), 2005.

[34] P. G. de Gennes. Molten polymers in strong flows: A nonclassical proposal. *MRS Bulletin, January*, page 20, 1991.

[35] Albert Einstein. Uber die von der molekularkinetischen theorie der warme geforderte bewegung von in ruhenden flussigkeiten suspendierten teilchen. *Annalen der Physik*, 322(8):549–560, 1905.

[36] M. Doi and S. F. Edwards. *The Theory of Polymer Dynamics*. Clarendon, Oxford, 1986.

[37] Bruno H. Zimm. Dynamics of polymer molecules in dilute solution: Viscoelasticity, flow birefringence and dielectric loss. *Journal of Chemical Physics*, 24(2):269–279, 1956.

[38] P. G. de Gennes. Dynamics of entangled polymer solutions. ii. inclusion of hydrodynamic interactions. *Macromolecules*, 9(4), 1976.

[39] G. C. Berry and T. G. Fox. The viscosity of polymers and their concentrated solutions. *Advances in Polymer Science*, 5:261–357, 1968.

[40] Masao Doi. Explanation for the 3.4-power law for viscosity of polymeric liquids on the basis of the tube model. *Journal of Polymer Science*, 21:667–684, 1983.

[41] S. T. Milner and T. C. B. McLeish. Reptation and contour-length fluctuations in melts of linear polymers. *Physical Review Letters*, 81:725–728, 1998.

[42] William W. Graessley. Entangled linear, branched and network polymer systems - molecular theories. *Advances in Polymer Science*, 47:67–117, 1982.

[43] J.P. Montfort, G. Martin, and P. Monge. Effects of constraint release on the dynamics of entangled linear polymer melts. *Macromolecules*, 17(8):1551–1560, 1984.

[44] G. Marrucci. Dynamics of entanglements: A nonlinear model consistent with the cox-merz rule. *Journal of Non-Newtonian Fluid Mechanics*, 62(2-3):279–289, 1996.

[45] G. Ianniruberto and G. Marrucci. On compatibility of the cox-merz rule with the model of doi and edwards. *Journal of Non-Newtonian Fluid Mechanics*, 65(2-3):241–246, 1996.

[46] G. Ianniruberto and G. Marrucci. Convective orientational renewal in entangled polymers. *Journal of Non-Newtonian Fluid Mechanics*, 95(2-3):363–374, 2000.

[47] S. T. Milner and A. E. Likhtman. Microscopic theory of convective constraint release. *Journal of Rheology*, 24(2), 2001.

[48] Maurice L. Huggins. Theory of solutions of high polymers. *Journal of the American Chemical Society*, 64(7):1712–1719, 1942.

[49] Paul J. Flory. Thermodynamics of high polymer solutions. *Journal of Chemical Physics*, 10(1), 1942.

[50] Paul J. Flory and William r. Krigbaum. Thermodynamics of high polymer solutions. *Annual Review of Physical Chemistry*, 2:282–402, 1951.

[51] Eugene Helfand and Yukiko Tagami. Theory of the interface between immiscible polymers. *Polymer Letters*, 9:741–746, 1971.

[52] Eugene Helfand and Yukiko Tagami. Theory of the interface between immiscible polymers. ii. *Journal of Chemical Physics*, 56(7), 1972.

[53] Eugene Helfand. Theory of inhomogenous polymers: Fundamentals of the gaussian random-walk model. *Journal of Chemical Physics*, 62(3), 1975.

[54] Ludwik Leibler. Theory of microphase separation in block copolymers. *Macromolecules*, 13(6):1602–1617, 1980.

[55] K. M. Hong and J. Noolandi. Theory of inhomogenous multicomponent polymer systems. *Macromolecules*, 14(3):727–736, 1981.

[56] M. W. Matsen. The standard gaussian model for block copolymer melts. *Journal of Physics: Condensed Matter*, 14(2), 2002.

[57] Mark W. Matsen and Michael Schick. Self-assembly of block copolymers. *Current Opinion in Colloid and Interface Science*, 1(3):329–336, 1996.

[58] V. Ganesan and G. H. Fredrickson. Field-theoretic polymer simulations. *Europhysics Letters*, 55(6), 2001.

[59] Glenn H. Fredrickson, Venkat Ganesan, and Fracois Drolet. Field-theoretic computer simulation methods for polymer and complex fluids. *Macromolecules*, 35(1):16–39, 2002.

[60] Hector D. Ceniceros and Glenn H. Fredrickson. Numerical solution of polymer self-consistent field theory. *Multiscale Modeling and Simulation*, 2(3):452–474, 2004.

[61] Philip J. Cole, Robert F. Cook, and Christopher W. Macosko. Adhesion between immiscible polymers correlated with interfacial entanglements. *Macromolecules*, 36(8):2808–2815, 2003.

[62] F. Brochard-Wyart. Deformations of one tethered chain in strong flows. *Europhysics Letters*, 23(2):105–111, 1993.

[63] F. Brochard-Wyart and A. Buguin. Polymer chains under strong flow: Stems and flowers. *MRS Bulletin, January*, pages 48–52, 1997.

[64] Armand Ajdari, Francoise Brochard-Wyart, Pierre-Gilles de Gennes, Ludwik Leibler, Jean-Louis Viovy, and Michael Rubinstein. Slippage of an entangled polymer melt on a grafted surface. *Physica A*, 204(1-4):17–39, 1994.

[65] F. Brochard-Wyart, C. Gay, and P. G. de Gennes. Slippage of polymer melts on grafted surfaces. *Macromolecules*, 29:377–382, 1996.

[66] F. Brochard and P. G. de Gennes. Shear-dependent slippage at a polymer/solid interface. *Langmuir*, 8:3033–3037, 1992.

[67] Masao Doi, Dale Pearson, Julie Kornfield, and Gerry Fuller. Effect of nematic interaction in the orientational relaxation of polymer melts. *Macromolecules*, 22:1488–1490, 1989.

[68] Kohzo Ito. Novel cross-linking concept of polymer network: synthesis, structure, and properties of slide-ring gels with freely movable junctions. *Polymer Journal*, 39(6):489–499, 2007.

[69] T. Koga and F. Tanaka. Elastic properties of polymer networks with sliding junctions. *European Physical Journal E*, 17:225–229, 2005.

[70] Akira Onuki. Elastic effects in the phase transition of polymer solutions under shear flow. *Physical Review Letters*, 62(21), 1989.

[71] Kazushi Horio and Yuichi Masubuchi. Pre-averaged sampling on the entanglement kinetics for polymer dynamics. *Macromolecular Symposia*, 242:140–145, 2006.

[72] A. D. Drozdov. Polymer networks with slip-links: 1. constitutive equations for an uncross-linked network. *Continuum Mechanics and Thermodynamics*, 18:157–170, 2006.

[73] A. D. Drozdov. Polymer networks with slip-links: 2. constitutive equations for a cross-linked network. *Continuum Mechanics and Thermodynamics*, 18:171–193, 2006.

[74] T. A. Vilgis. Entanglements in rubbers. *Progress in Colloid & Polymer Science*, 75:4–10, 1987.

[75] J. Rieger. An example of spontaneous symmetry breaking in polymer physics. *Polymer Bulletin*, 18:343–346, 1987.

[76] Jens Rieger. Constrained polymer with unusual statistics. annotations on the slip-link model. *Macromolecules*, 22:4540–4544, 1989.

[77] T. A. Vilgis. Are sliplink models dangerous? *Polymer Bulletin*, 19:615–617, 1988.

[78] Jens-Uwe Sommer. Degenerate ground states of simple slip-link systems. *Journal of Chemical Physics*, 97(8), 1992.

[79] Dirk Looman, Igor M. Sokolov, and Alexander Blumen. Bistability of polymers in pores. *Macromolecules*, 29:4777–4781, 1996.

[80] M. H. Wagner and J. Schaeffer. Nonlinear strain measures for general biaxial extension of polymer melts. *Journal of Rheology*, 36(1), 1992.

[81] Thomas A. Vilgis and Burak Erman. Comparison of the constrained junction and the slip-link models of rubber elasticity. *Macromolecules*, 26:6657–6659, 1993.

[82] M. H. Wagner and J. Schaeffer. Constitutive equations from gaussian slip-link network theories in polymer melt rheology. *Rheologica Acta*, 31:22–31, 1992.

[83] Ralf Metzler, Andreas Hanke, Paul G. Dommersnes, Yacov Kantor, and Mehran Kardar. Tightness of slip-linked polymer chains. *Physical Review E*, 65(061103), 2002.

[84] Ralf Metzler, Yacov Kantor, and Mehran Kardar. Force-extension relations for polymers with sliding links. *Physical Review E*, 66(022102), 2002.

[85] Andreas Hanke and Ralf Metzler. Towards the molecular workshop: entropy-driven designer molecules, entropy activation, and nanomechanical devices. *Chemical Physics Letters*, 359:22–26, 2002.

[86] Jorge Ramirez, Sathish K. Sukumaran, and Alexei E. Likhtman. Significance of cross correlations in the stress relaxation of polymer melts. *Journal of Chemical Physics*, 126(244904), 2007.

[87] Jorge Ramirez, Sathish K. Sukumaran, and Alexei E. Likhtman. Hierarchical modeling of entangled polymers. *Macromolecular Symposia*, 252:119–129, 2007.

[88] M. G. Brereton and P. G. Klein. Analysis of the rubber elasticity of polyethylene networks based on the slip-link model of s. f. edwards et al. *POLYMER*, 29, 1988.

[89] P. G. Higgs and R. C. Ball. Trapped entanglements in rubbers. a unification of models. *Europhysics Letters*, 8(4):357–361, 1989.

[90] P. Thirion and J. F. Tassin. Nonlinear viscoelasticity of entangled polymer chains. i. response of the slip-link model to elongation strains. *Journal of Polymer Science*, 21:2097–2107, 1983.

[91] S. F. Edwards and T. A. Vilgis. The tube model theory of rubber elasticity. *Reports on Progress in Physics*, 51:243–297, 1988.

[92] S. F. Edwards and Th. Vilgis. The stress-strain relationship in polymer glasses. *POLYMER*, 28, 1987.

[93] Jean Louis Viovy. Tube relaxation: A quantitative molecular model for the viscoelastic plateau of entangled polymeric media. *Journal of Polymer Science*, 23:2423–2442, 1985.

[94] J. L. Viovy, L. Monnerie, and J. F. Tassin. Tube relaxation: A necessary concept in the dynamics of strained polymers. *Journal of Polymer Science*, 21:2427–2444, 1983.

[95] Pierre Thirion. Revisal of the chain equilibration process in strained polymer melts. *Polymer Bulletin*, 6:541–546, 1982.

[96] S. Nechaev, G. Oshanin, and A. Blumen. Anchoring of polymer by traps randomly placed on a line. *Journal of Statistical Physics*, 98(1-2):281–303, 1999.

[97] S. Shanbhag, R. G. Larson, J. Takimoto, and M. Doi. Deviations from dynamic dilution in the terminal relaxation of star polymers. *Physical Review Letters*, 87(19), 2001.

[98] Richard S. Graham and Ronald G. Larson. Coarse-grained brownian dynamics simulations of electrophoresis of dna molecules from generalized reptation models. *Macromolecules*, 40:366–378, 2007.

[99] F. Greco. The stress tensor in entangled polymers. *Physical Review Letters*, 88(10), 2002.

[100] Francesco Greco. New strain measure tensor for entangled polymeric liquids. *Journal of Rheology*, 47(1):235–246, 2003.

[101] Julian Oberdisse, Giovanni Ianniruberto, Francesco Greco, and Giuseppe Marrucci. Mechanical properties of end-crosslinked entangled polymer networks using sliplink brownian dynamics simulations. *Rheologica Acta*, 46:95–109, 2006.

[102] J. Oberdisse, G. Ianniruberto, F. Greco, and G. Marrucci. Primitive-chain brownian simulations of entangled rubbers. *Europhysics Letters*, 58(4):530–536, 2002.

[103] R. Podgornik. Surface polymer network model and effective membrane curvature elasticity. *Physical Review E*, 51(4), 1995.

[104] Douglas Adolf. Origins of entanglement effects in rubber elasticity. *Macromolecules*, 21:228–230, 1988.

[105] Michael Rubinstein and Sergei Panyukov. Elasticity of polymer networks. *Macromolecules*, 35:6670–6686, 2002.

[106] M. Kosc. Belt-loop model of chain entanglement. *Colloid & Polymer Science*, 266:105–113, 1988.

[107] M. Kosc. Segmental orientation in entangled chains. *Colloid & Polymer Science*, 270:106–112, 1992.

[108] D. W. Mead. Development of the binary interaction theory for entangled polydisperse linear polymers. *Rheologica Acta*, 46:369–395, 2007.

[109] Ajey Dambal, Amit Kushwaha, and Eric S. G. Shaqfeh. Slip-link simulations of entangled, finitely extensible, wormlike chains in shear flow. *Macromolecules*, 42:7168–7183, 2009.

[110] Yuichi Masubuchi, Giovanni Ianniruberto, Francesco Greco, and Giuseppe Marrucci. Primitive chain network model for block copolymers. *Journal of Non-crystaline Solids*, 352:5001–5007, 2006.

[111] Kenji Furuichi, Chisato Nonomura, Yuichi Masubuchi, Hiroshi Watanabe, Giovanni Ianniruberto, Francesco Greco, and Giuseppe Marrucci. Entangled polymer orientation and stretch under large step shear deformations in primitive chain network simulations. *Rheologica Acta*, 47:591–599, 2008.

[112] Yuichi Masubuchi, Hiroshi Watanabe, Giovanni Ianniruberto, Francesco Greco, and Giuseppe Marrucci. Comparison among slip-link simulations of bidisperse linear polymer melts. *Macromolecules*, 41:8275–8280, 2008.

[113] Yuichi Masubuchi, Giovanni Ianniruberto, Francesco Greco, and Giuseppe Marrucci. Entanglement molecular weight and frequency response of slip-link networks. *Journal of Chemical Physics*, 119(13):6925–6930, 2003.

[114] Yuichi Masubuchi, Hiroshi Watanabe, Giovanni Ianniruberto, Francesco Greco, and Giuseppe Marrucci. Primitive chain network simulations of conformational relaxation for individual molecules in the entangled state. *Journal of the Society of Rheology, Japan*, 36(4):181–185, 2008.

[115] Yuichi Masubuchi, Takashi Uneyama, Hiroshi Watanabe, Giovanni Ianniruberto, Francesco Greco, and Giuseppe Marrucci. Primitive chain network simulations of conformational relaxation for individual molecules in the entangled state. ii. retraction from stretched states. *Journal of the Society of Rheology, Japan*, 37(2):65–68, 2009.

[116] Yuichi Masubuchi, Giovanni Ianniruberto, Francesco Greco, and Giuseppe Marrucci. Primitive chain network simulations for branched polymers. *Rheologica Acta*, 46:297–303, 2006.

[117] Yuichi Masubuchi, Jun-Ichi Takimoto, Kiyohito Koyama, Giovanni Ianniruberto, Giuseppe Marrucci, and Francesco Greco. Brownian simulations of a network of reptating primitive chains. *Journal of Chemical Physics*, 115(9):4387–4394, 2001.

[118] Yuichi Masubuchi, Giovanni Ianniruberto, Giuseppe Marrucci, and Francesco Greco. Biased hooking for primitive chain network simulations of block copolymers. *Korea-Australia Rheology Journal*, 18(2):99–102, 2006.

[119] Hiroyasu Tasaki, Jun ichi Takimoto, and Masao Doi. Prediction of the rheological properties of polymers using a stochastic simulation. *Computer Physics Communications*, 142:136–139, 2001.

[120] Kenji Urayama, Takanobu Kawamura, and Shinzo Kohjiya. Multiaxial deformations of end-linked poly(dimethylsiloxane) networks. 4. further assessment of the slip-link model for chain-entanglement effect on rubber elasticity. *Journal of Chemical Physics*, 118(12), 2003.

[121] Alexei E. Likhtman. Single-chain slip-link model of entangled polymers: simultaneous description of neutron spin-echo, rheology, and diffusion. *Macromolecules*, 38:6128–6139, 2005.

[122] Alexei E. Likhtman, Sathish K. Sukumaran, and Jorge Ramirez. Linear viscoelasticity from molecular dynamics simulation of entangled polymers. *Macromolecules*, 40:6748–6757, 2007.

[123] M. Zamponi, A. Wischnewski, M. Monkenbusch, L. Willner, D. Richter, A. E. Likhtman, G. Kali, and B. Farago. Molecular observation of constraint release in polymer melts. *Physical Review Letters*, 96(238302), 2006.

[124] J. Ramirez and A. E. Likhtman. Advanced single chain models for entangled polymers. *Esaform 2008 Conference Proceedings*, 2008.

[125] J. Sweeney and I. M. Ward. A constitutive law for large deformations of polymers at high temperatures. *Journal of the Mechanics and Physics of Solids*, 44(7):1033–1049, 1996.

[126] P. G. Higgs and R. J. Gaylord. Slip-links, hoops and tubes: tests of entanglement models of rubber elasticity. *POLYMER*, 31, 1990.

[127] S. F. Edwards and Th. Vilgis. The effect of entanglements in rubber elasticity. *POLYMER*, 27, 1986.

[128] R. C. Ball, M. Doi, and M. Warner. Elasticity of entangled networks. *POLYMER*, 22, 1981.

[129] P. Thirion and T. Weil. Assessment of the sliding link model of chain entanglement in polymer networks. *POLYMER*, 25, 1984.

[130] S. Shanbhag and R. G. Larson. A slip-link model of branch-point motion in entangled polymers. *Macromolecules*, 37:8160–8166, 2004.

[131] H. Janeschitz-Kriegl. Some pending problems in polymer melt rheology, as seen from the point of view of doi's slip-link model. *Rheologica Acta*, 21:388–393, 1982.

[132] S. Bensason, E. V. Stepanov, S. Chum, A. Hiltner, and E. Baer. Deformation of elastomeric ethylene-octene copolymers. *Macromolecules*, 30:2436–2444, 1997.

[133] Bohumil Meissner and Libnor Matejka. Analysis of the biaxial stress-strain behavior of poly(dimethylsiloxane) networks from the viewpoint of the slip-link model of rubber elasticity. *Journal of Polymer Science*, 42:2318–2328, 2004.

[134] Bohumil Meissner and Libnor Matejka. Comparison of recent rubber-elasticity theories with biaxial stress-strain data: the slip-link theory of edwards and vilgis. *POLYMER*, 43:3803–3809, 2002.

[135] Yuichi Masubuchi, Giovanni Ianniruberto, Francesco Greco, and Giuseppe Marrucci. Quantitative comparison of primitive chain network simulations with literature data of linear viscoelasticity for polymer melts. *Journal of Non-Newtonian Fluid Mechanics*, 149:87–92, 2008.

[136] Kenji Furuichi, Chisato Nonomura, Yuichi Masubuchi, Giovanni Ianniruberto, Francesco Greco, and Giuseppe Marrucci. Primitive chain network simulations of damping functions for shear, uniaxial, biaxial and planar deformations. *Journal of the Society of Rheology, Japan*, 35(2):73–77, 2007.

[137] Yuichi Masubuchi, Kenji Furuichi, Kazushi Horio, Takashi Uneyama, Hiroshi Watanabe, Giovanni Ianniruberto, Francesco Greco, and Giuseppe Marrucci. Primitive chain network simulations for entangled dna solutions. *Journal of Chemical Physics*, 131, 2009.

[138] Takatoshi Yaoita, Takeharu Isaki, Yuichi Masubuchi, Hiroshi Watanabe, Giovanni Ianniruberto, Francesco Greco, and Giuseppe Marrucci. Statics, linear, and nonlinear dynamics of entangled polystyrene melts simulated through the primitive chain network model. *Journal of Chemical Physics*, 128, 2008.

[139] Masao Doi and Jun ichi Takimoto. Molecular modeling of entanglement. *Philosophical Transactions of the Royal Society of London A*, 361:641–652, 2003.

[140] Marcus Muller and Kostas Ch. Daoulas. Single-chain dynamics in a homogenous melt and a lamellar microphase: A comparison between smart monte carlo dynamics, slithering-snake dynamics, and slip-link dynamics. *Journal of Chemical Physics*, 129(164906), 2008.

[141] J. Sweeney. A comparison of three polymer network models in current use. *Computational and Theoretical Polymer Science*, 9:27–33, 1999.

[142] William W. Graessley. Entangled linear, branched and network polymer systems - molecular theories. *Advances in Polymer Science*, 47:67–117, 1982.

[143] Sachin Shanbhag, Seung Joon Park, Qiang Zhou, and Ronald G. Larson. Implications of microscopic simulations of polymer melts for mean-field tube theories. *Molecular Physics*, 105(2-3):249–260, 2007.

[144] Ronald G. Larson. Advances in modeling of polymer melt rheology. *AIChE Journal*, 53(3), 2007.

[145] Jay D. Schieber. Fluctuations in entanglements in polymer liquids. *Journal of Chemical Physics*, 118(11):5162–5166, 2003.

[146] Marat Andreev, Renat N. Khaliullin, Rudi J. A. Steenbakkers, and Jay D. Schieber. Approximations of the discrete slip-link model and their effect on nonlinear rheology predictions. *Journal of Rheology*, 57(2):535–557, 2013.

[147] Ekaterina Pilyugina, Marat Andreev, and Jay D. Schieber. Dielectric relaxation as an independent examination of relaxation mechanisms in entangled polymers using the discrete slip-link model. *Macromolecules*, 45(14):5728–5743, 2012.

[148] Rudi J. A. Steenbakkers and Jay D. Schieber. Derivation of free energy expressions for tube models from coarse-grained slip-link models. *Journal of Chemical Physics*, 137(3), 2012.

[149] Mette Krog Jensen, Renat Khaliullin, and Jay D. Schieber. Self-consistent modeling of entangled network strands and linear dangling structures in a single-strand mean-field slip-link model. *Rheologica Acta*, 51(1):21–35, 2012.

[150] Renat N. Khaliullin and Jay D. Schieber. Application of the slip-link model to bidisperse systems. *Macromolecules*, 43(14):6202–6212, 2010.

[151] Jay D. Schieber and Kazushi Horio. Fluctuation in entanglement positions via elastic slip-links. *Journal of Chemical Physics*, 132(7), 2010.

[152] Renat N. Khaliullin and Jay D. Schieber. Self-consistent modeling of constraint release in single-chain mean-field -slip-link model. *Macromolecules*, 42(19):7504–7517, 2009.

[153] Jay D. Schieber, Deepa M. Nair, and Thidaporn Kitkrailard. Comprehensive comparisons with nonlinear flow data of a consistently unconstrained brownian slip-link model. *Journal of Rheology*, 51(6):1111–1141, 2007.

[154] Deepak M. Nair and Jay D. Schieber. Linear viscoelastic predictions of a consistently unconstrained brownian slip-link model. *Macromolecules*, 39(9):3386–3397, 2006.

[155] Jay D. Schieber. Generic compliance of a temporary network model with sliplinks, chain-length fluctuations, segment-connectivity and constraint release. *Journal of Non-equilibrium Thermodynamics*, 28(2):179–188, 2003.

[156] Jay D. Schieber, Jesper Neergaard, and Sachin Gupta. A full-chain, temporary network model with slip-links, chain-length fluctuations, chain connectivity and chain stretching. *Journal of Rheology*, 47(1):213–233, 2003.

[157] Renat N. Khaliullin and Jay D. Schieber. Analytic expressions for the statistics of the primitive-path length in entangled polymers. *Physical Review Letters*, 100, 2008.

[158] David T. Wu, Glenn H. Fredrickson, Jean-Pierre Carton, Armand Ajdari, and Ludwik Leibler. Distribution of chain ends at the surface of a polymer melt: Compensation effects and surface tension. *Journal of Polymer Science Part B: Polymer Physics*, 33(17):2373–2389, 1995.

[159] David T. Wu, Glenn H. Fredrickson, and Jean-Pierre Carton. Surface segregation in conformationally asymmetric polymer blends: Incompressibility and boundary conditions. *Journal of Chemical Physics*, 104(16):6387–6397, 1996.

[160] Nicholas Metropolis, Arianna W. Rosenbluth, Marshall N. Rosenbluth, Augusta H. Teller, and Edward Teller. Equation of state calculations by fast computing machines. *Journal of Chemical Physics*, 21(6), 1953.

[161] Markus Kollman. Single-file diffusion of atomic and colloidal systems: asymptotic laws. *Physical Review Letters*, 90(18), 2003.

[162] Christoph Lutz, Markus Kollman, and Clemens Bechinger. Single-file diffusion of colloids in one-dimensional channels. *Physical Review Letters*, 93(2), 2004.

[163] Binhua Lin, Mati Meron, Bianxiao Cui, Stuart A. Rice, and Haim Diamant. From random walk to single-file diffusion. *Physical Review Letters*, 94(21), 2005.

[164] Alessandro Taloni and Fabio Marchesoni. Single-file diffusion on a periodic substrate. *Physical Review Letters*, 96(2), 2006.

[165] L. Lizana and T. Ambjornsson. Single-file diffusion in a box. *Physical Review Letters*, 100(20), 2008.

[166] Pouyan E. Boukany, Shi-Qing Wang, and Xiaorong Wang. Universal scaling behavior in startup shear of entangled linear polymer melts. *Journal of Rheology*, 53(3):617–629, 2009.

[167] Jinhai Yang and James L. White. Interface slippage study between polyamide 12 and ethylene butene copolymer melt in capillary extrusion. *Journal of Rheology*, 53(5):1121–1132, 2009.

[168] Younggon Son. Investigation of interfacial slip in immiscible polymer blends. *Journal of Polymer Research*, 18:2087–2092, 2011.

[169] Jian Qin. Studies of block copolymer melts by field theory and molecular simulation. *Ph.D. thesis, University of Minnesota*, 2009.

Appendix A

Doi-Edwards Polymer Tube Theory

In this section the tube theory of polymer dynamics developed by Doi and Edwards is briefly outlined with emphasis on the portions relevant to this work. The derivations given below follow those in [36].

A polymer residing in a melt has its motion restricted by the surrounding polymers such that motion along its length is possible but transverse motion is nearly impossible. The polymer can be considered to reside in a tube. As the polymer diffuses it will vacate portions of the tube, after which the vacated portions are considered to randomize their orientation. Considering the tube from some chosen beginning time denoted as $t = 0$, the fraction of the "original" tube remaining as time progresses can be analyzed.

The total length of the original tube is the polymer primitive path length L. Let $\Psi(\alpha, t; s)$ be the probability that the polymer chain has diffused distance α in time t while the chain ends have not yet reached segment s of the original tube (the "original" tube is a tube running along the entire polymer length at time $t = 0$). This

probability satisfies the one dimensional diffusion equation:

$$\frac{\partial \Psi}{\partial t} = D\frac{\partial^2 \Psi}{\partial \alpha^2} \tag{A.1}$$

Here D is the diffusion coefficient for total polymer diffusion along its length (reptation). The polymer is subject to friction proportional to its primitive path length, and the Einstein diffusion relation [35] gives the diffusion coefficient as:

$$D = \frac{\mathrm{k_B}T}{\zeta L} \tag{A.2}$$

Here T is the absolute temperature, $\mathrm{k_B}$ is Boltzmann's constant, and ζ is the friction coefficient conjugate to primitive path length L.

By construction at $t = 0$ all of the original tube will be in existence, and so Ψ is subject to the initial condition:

$$\Psi(\alpha, 0; s) = \delta(\alpha) \tag{A.3}$$

When the diffused distance α is s or $s - L$ then one end of the chain has reached the tube segment at s. Consequently Ψ is subject to the boundary conditions:

$$\Psi(s, t; s) = 0 \qquad\qquad \Psi(s - L, t; s) = 0 \tag{A.4}$$

With these initial and boundary conditions it is possible to solve for Ψ giving the result:

$$\Psi(\alpha, t; s) = \sum_{p=1}^{\infty} \frac{2}{L} \sin\left(\frac{p\pi s}{L}\right) \sin\left(\frac{p\pi(s-\alpha)}{L}\right) \exp\left[-p^2 t/t_d\right] \tag{A.5}$$

$$t_d = \frac{L^2}{D\pi^2} = \frac{L^3\zeta}{\pi^2 \mathrm{k_B}T} \tag{A.6}$$

It can be seen that Ψ in this model has the form of a series sine terms in the space

of polymer length, each multiplied by an exponential which decays with time. The most slowly decaying term has characteristic decay time t_d as shown in equation A.6. Consequently t_d is the characteristic time for the polymer to have vacated all of its original tube constraints, and is thus the reptation time for this model. As expected from the fundamental reptation description given in Chapter 1 the reptation time is proportional to $L^3\zeta/(\mathrm{k_B}T)$. The factor of π^{-2} in the reptation time for this model is the result of the specific way the tube-like constraints have been mathematically described, and different models will have different numerical prefactors depending on the specific modeling choices made.

From the result obtained for Ψ it is possible to consider the probability that the tube segment at position s will still remain (will not have been reached by one of the polymer ends and had its orientation randomized) at time t. Denoting the probability that the tube segment at position s will remain at time t by $\psi(s,t)$, it is given by:

$$\psi(s,t) = \int_{s-L}^{s} d\alpha\, \Psi(\alpha, t; s) \tag{A.7}$$

$$\psi(s,t) = \sum_{p;\, odd} \frac{4}{p\pi} \sin\left(\frac{p\pi s}{L}\right) \exp\left[-p^2 t/t_d\right] \tag{A.8}$$

Now considering the total fraction of the original tube remaining at time t, and denoting this as $\psi(t)$, this is found to be:

$$\psi(t) = \frac{1}{L}\int_0^L ds\, \psi(s,t) = \sum_{p;\, odd} \frac{8}{p^2\pi^2} \exp\left[-p^2 t/t_d\right] \tag{A.9}$$

Small sudden deformations of a polymer melt induce small amounts of stress; in such a case a "proportional decay" physical prediction / approximation is made that the induced stress will decay in a manner proportional to the decay of the original

tube remaining from the time of the induced stress.

$$\sigma_{ij}(t) = \sigma_{ij}(0)\psi(t) \tag{A.10}$$

Here $\sigma_{ij}(0)$ is the stress induced by a small sudden (instantaneous) deformation at time $t = 0$, and $\psi(t)$ is the fraction of the original tube (from time $t = 0$) which remains at time t (the fractional tube survival probability from Equation A.9). This physical prediction states that the fraction of polymer melt stress remaining following a small sudden deformation is equal to the average fraction of the original polymer tube constraints remaining from the time of deformation. The melt is considered to be composed of many polymers so that the total melt stress will be a macroscopic average of all the individual polymer stress contributions. Physical motivation for the proportional decay prediction is sometimes made by arguing that it is physically realistic that each small section of the deformed polymer tube makes an independent additive stress contribution that is on average the same as every other small polymer tube section, and which persists until lost when the tube section is first vacated by the diffusing polymer (after which the tube section orientation is randomized so that it makes no net stress contribution). Furthermore, for the expression in Equation A.10 to be accurate the deformation must be small in the sense that reptative diffusion will continue to progress as in equilibrium because $\psi(t)$ was derived for the equilibrium case. The stress expression in equation A.10 has shown fair agreement with experiment for small rapid polymer melt deformations [36].

It is possible to use this model to make melt stress predictions for more complex deformations and induced stress histories, such as situations in which a stress inducing deformation is extended in time. In order to do this a few physical approximations must be made. First, it is considered that a polymer tube section contributes to the melt stress during a deformation until the tube section is vacated by the diffusing

polymer. Second, an "independent contribution" approximation is made, in which stresses induced in each small polymer tube section are considered to be independent, and to add. In this approximation the stress contribution and survival probability of each polymer tube section are independent from other polymer tube sections. These assumptions can be used to generate the following stress equation for a melt undergoing an extended stress inducing deformation:

$$\sigma_{ij}(t) = \int_{-\infty}^{t} dt' \, \mu(t-t')\sigma_{ij}^{(I)}(t-t') \tag{A.11}$$

Here $\mu(t-t')dt'$ is the probability that a small polymer tube section which was created in an infinitesimal time interval dt' around time t' will continue to exist at time t (it will not have been vacated by the diffusing polymer). $\sigma_{ij}^{(I)}(t-t')$ is the total stress induced in all small polymer sections at time t by some deformation history if the deformation history acted on continuously existing polymer tube sections that began with random orientation at time t'.

The tube section survival probability $\mu(t-t')dt'$ can be related to the fractional tube survival probability $\psi(t-t_0)$ through the following argument. The survival probability of all tube segments created before time $t = t_0$ must be proportional to the fractional tube survival probability from that time (all portions of the tube came into existence at some previous time, and the fractional tube survival probability is averaged over the possible polymer histories).

$$\int_{-\infty}^{t_0} \mu(t-t')dt' \propto \psi(t-t_0) \tag{A.12}$$

This suggests that $\mu(t-t') = -A\frac{\partial\psi}{\partial t'}(t-t')$, with A being a constant. Considering the boundary conditions of ψ, where $\psi(0) = 1$ and $\psi(\infty) = 0$ (the polymer will eventually diffuse out of the entire original tube), it is found that $A = 1$; $-A\int_{-\infty}^{0} dt' \, \frac{\partial\psi}{\partial t'}(0-t') =$

$\psi(0) - \psi(\infty)$ if $A = 1$. Consequently the tube section survival probability $\mu(t-t')dt'$ is given by:

$$\mu(t-t')dt' = -\frac{\partial \psi}{\partial t'}(t-t')dt' \tag{A.13}$$

This probability argument for the relation between the sectional and fractional tube survival probabilities (μ and ψ respectively) is general and includes the Doi-Edwards model as a specific case. Using the expression for ψ which was obtained in Equation A.9 this results in μ being equal to the expression given in Equation 3.51 of Chapter 3.

The melt stress expression in Equation A.11 is sometimes altered so that the induced stress $\sigma_{ij}^{(I)}(t-t')$ is expressed as the product of a constant stress factor and a dimensionless deformation function. The deformation function is sometimes argued to be a type of measure of the polymer section tube alignment. In such a case the independent contribution approximation for polymer tube sections is referred to as the independent alignment approximation. (Such an approximation can be motivated by an argument analogous to the one given in Chapter 3 in which it is argued that polymer stretching during interfacial slip does not significantly increase tension above the equilibrium value, and so interfacial tension is governed by strand alignment.) In this form Equation A.11 becomes:

$$\sigma_{ij}(t) = \sigma_0 \int_{-\infty}^{t} dt' \left(-\frac{\partial \psi}{\partial t'}(t-t')dt' \right) \chi_{ij}(t-t') \tag{A.14}$$

Here $\chi_{ij}(t-t')$ is the polymer tube section deformation or alignment measure, and σ_0 is the stress constant (the negative sign within the integral is sometimes absorbed in the alignment measure definition). This strategy of calculating polymer melt stress as a function of deformation has produced fair agreement with experiment in some cases [36]. A similar strategy is used in this work during the analysis of the interfacial

stress due to slip induced polymer strand alignment in Chapter 3.

Appendix B

Numerically Solving for Polymer Strand Green Functions and Self-Consistent Fields

In Chapter 5 a method of simulating polymers in a chemical potential field representing a polymer-polymer interface was described. This was done through calculating polymer strand Green functions (statistical weights) in the chemical potential field, and employing these in the move acceptance probabilities of the Monte Carlo slip-link polymer simulation in order to obtain the correct configuration probability distribution. The chemical potential field was determined self-consistently by a numerical calculation, and the polymer strand Green functions were then numerically calculated in the chemical potential field. The fundamental equations governing these calculations were given in Chapter 5; in this appendix the method of numerical calculation of the fields and Green functions is described.

Equations 5.3, 5.3, 5.4, and 5.5, determine a chemical potential field (up to an additive constant) representing a polymer-polymer interface, and are here re-written

for easier reference:

$$\begin{aligned} \omega_A(\vec{r}) &= \mathrm{k_B}T\chi\,\phi_B(\vec{r}) + \eta(\vec{r}) \\ \omega_B(\vec{r}) &= \mathrm{k_B}T\chi\,\phi_A(\vec{r}) + \eta(\vec{r}) \end{aligned} \tag{B.1}$$

$$\phi_A(\vec{r}) + \phi_B(\vec{r}) = 1 \tag{B.2}$$

$$\phi_\alpha(\vec{r}) = \frac{1}{Q_\alpha(N)} \int_0^N q_\alpha(\vec{r}; N_s) q_\alpha(\vec{r}; N - N_s) dN_s \qquad Q_\alpha(N) = \int d\vec{r}\, q_\alpha(\vec{r}; N) \tag{B.3}$$

$$\frac{\partial q_\alpha(\vec{r}; N_s)}{\partial N_s} = \left(\frac{b^2}{6}\nabla^2 - \frac{\omega(\vec{r})}{\mathrm{k_B}T} \right) q_\alpha(\vec{r}; N_s) \qquad\qquad q_\alpha(\vec{r}; 0) = 1 \tag{B.4}$$

Briefly restating the meaning of these equations: The ω functions are chemical potential fields describing a polymer-polymer interface (the subscript indicating the chemical species the field acts on), and the ϕ functions represent the local volume fractions occupied by each polymer species. Equation B.2 is the Flory-Huggins [48–50] expression for the chemical potential dependence on the volume fractions; χ is a repulsion parameter and η is a local pressure. Equation B.2 conveys the melt incompressibility constraint. Equations B.3 and B.4 give the relationship between the chemical potentials ω and the volume fractions ϕ assuming that the polymers behave as Gaussian filaments (in these equations α indicates either one of the species subscripts, A or B). The derivation of Equation B.3 from the Gaussian filament model was given in Chapter 5. The q functions are statistical weights for a singly constrained polymer strand, and are related to the strand Green functions through $q_\alpha(\vec{r}; N_s) = \int d\vec{r}'\, G_\alpha(\vec{r}, \vec{r}'; N_s)$.

Equations 5.3, 5.3, 5.4, and 5.5, together determine the chemical potential fields $\omega_A(\vec{r})$ and $\omega_B(\vec{r})$ up to an additive constant, and this constant may be fixed by

choice (only energy differences between locations have physical effect). The chemical potential fields are solved for using a program named PSCF developed by Morse, Tyler, Ranjan, Qin, and Thiagarajan, in the Department of Chemical Engineering and Materials Science at the University of Minnesota. The descriptions given here of the workings of PSCF follow the Ph.D. thesis of Jian Qin from 2009 [169]. PSCF solves the equations using an iterative Newton-Raphson algorithm. The solution is performed for a cell using periodic boundary conditions. In the program the following quantities are defined as "residuals" to be minimized:

$$\begin{aligned} R_{I1} &= \phi_A(\vec{r}) + \phi_B(\vec{r}) - 1 \\ R_{I2} &= \omega_\alpha(\vec{r}) - \chi\phi_\beta(\vec{r}) - \zeta(\vec{r}) \\ R_{II} &= \frac{dF}{dy_{cell}} \end{aligned} \tag{B.5}$$

The solution to the field equations should result in residuals R_{I1} and R_{I2} having value zero. Additionally, residual R_{II} represents the rate of change of system free energy with respect to the periodic cell length, which is also minimized. The program works through an iterative process by which it attempts to minimize all of the residuals. It first begins from some approximate chemical potential profile (a guess) which is then perturbed by a small amount. The perturbations are of the chemical potential field and the cell length; these quantities shall collectively be referred to as X_β (corresponding to particular components of the chemical potential, or the cell length), and perturbations shall be denoted as δX_β. The program then determines the change in the residuals δR_α as a result of the perturbation, as stores the ratio in a "Jacobian" matrix $J_{\alpha\beta} \equiv \delta R_\alpha / \delta X_\beta$. The program then alters the X_α parameters according to the Newton-Raphson method, attempting to minimize the residuals:

$$X_\alpha^{(n+1)} = X_\alpha^{(n)} - {J^{(n)}}^{-1}_{\alpha\beta} R_\beta^{(n)} \tag{B.6}$$

Here the n superscripts are labeling iterations of the algorithm. After each update of the X_α parameters (the chemical potential field) the "Jacobian" matrix $J_{\alpha\beta}$ is recalculated, and the process is repeated. The iterations continue until all of the residuals are zero within some specified tolerance. Because the chemical potential is only uniquely determined by these equations up to a constant, this constant must be chosen, often the most common choice being that the chemical potential average is zero. When the algorithm has converged a self-consistent chemical potential field for a polymer-polymer interface has been obtained.

More detail will now be given for the numerical method of solving the differential equations for the Green and q functions. The differential equation defining the polymer strand Green functions is Equation 5.26 which is here reproduced for easier reference:

$$\frac{\partial G(\vec{r},\vec{r}';N_s)}{\partial N_s} = \frac{b^2}{6}\nabla^{2\prime} G(\vec{r},\vec{r}';N_s) - \frac{\omega(y)}{\mathrm{k_B}T} G(\vec{r},\vec{r}';N_s) \tag{B.7}$$
$$G(\vec{r},\vec{r}';0) = \delta(\vec{r}-\vec{r}')$$

Equation B.7 can be used to numerically solve for the Green functions in a chemical potential field. In the simulation of a planar polymer-polymer boundary the chemical potential is only a function of one dimension, and the Green function is therefore separable (Equation 5.27). Taking y as the coordinate along which the chemical potential field changes (the coordinate perpendicular to the planar boundary) G_y will obey:

$$\frac{\partial G_y(y,y';N_s)}{\partial N_s} = \left(\frac{b^2}{6}\frac{\partial^2}{\partial y^2} - \frac{\omega(y)}{\mathrm{k_B}T}\right) G_y(y,y';N_s) \tag{B.8}$$

Equation B.8 can be solved for G_y, while G_x and G_z will be given by functions of the form given in Equation 5.28. Equation B.8 is solved numerically using periodic boundary conditions via the pseudo-spectral method [60].

To explain the pseudo-spectral method first considered is an operator known as the Green function arc-length propagator. The function $G_y(y, y'; N_s + \Delta N)$ is related to the function $G_y(y, y'; N_s)$ through the series expansion:

$$G_y(y, y'; N_s + \Delta N) = \left(\sum_{j=0}^{\infty} \frac{\Delta N^j}{j!} \frac{\partial^j}{\partial N_s^j} \right) G_y(y, y'; N_s) \tag{B.9}$$

This can be expressed in operator notation by:

$$G_y(y, y'; N_s + \Delta N) = \exp\left[\Delta N \frac{\partial}{\partial N_s} \right] G_y(y, y'; N_s) \tag{B.10}$$

Here $\exp\left[\Delta N \frac{\partial}{\partial N_s}\right]$ is defined by its series expansion in ΔN, and may be called the arc-length propagator. For simplicity in further discussion a change in notation is made by defining operators:

$$\hat{A} \equiv \frac{\partial}{\partial N_s} \qquad \hat{B} \equiv \frac{b^2}{6} \frac{\partial^2}{\partial y^2} \qquad \hat{C} \equiv \frac{\omega(y)}{\mathrm{k_B} T} \tag{B.11}$$

In this notation the arc-length propagator in Equation B.10 is $\exp\left[\Delta N \hat{A}\right]$. The relationship in Equation B.8 suggests that when acting on the Green functions the operator $\hat{A}$ may be equivalent to the operator $\hat{B} - \hat{C}$; this further suggests that $\hat{B} - \hat{C}$ can be used in place of $\hat{A}$ in the arc-length propagator. However, Equation B.8 by itself is not enough to guarantee complete operator equivalence on the Green functions; in particular it does not guarantee equivalence of the operators under repeated application (which is required for operator substitution in the arc-length propagator). However, it can be quickly shown that if the operators $\hat{A}$ and $\hat{B} - \hat{C}$ commute then they are equivalent under repeated application on the Green functions. That is, the

operators are equivalent under repeated application if the following relation is true:

$$\hat{A}\left(\hat{B}-\hat{C}\right)G(y,y';N_s)=\left(\hat{B}-\hat{C}\right)\hat{A}\,G(y,y';N_s) \tag{B.12}$$

On the left side in Equation B.12 operator $\hat{B}-\hat{C}$ is the first being applied to the Green function, and it is known from Equation B.8 that a single application of $\hat{B}-\hat{C}$ is equivalent to a single application of $\hat{A}$. Thus the left side of Equation B.12 may be written as $\hat{A}^2\,G$. On the right side of Equation B.12 the operator $\hat{A}$ is the first being applied to the Green function, and it is known from Equation B.8 that a single application of $\hat{A}$ is equivalent to a single application of $\hat{B}-\hat{C}$. Consequently the right side of Equation B.12 may be written as $(\hat{B}-\hat{C})^2G$. Thus it can be seen that commutivity of $\hat{A}$ and $\hat{B}-\hat{C}$, along with Equation B.8, results in the equivalence of $\hat{A}^2$ and $(\hat{B}-\hat{C})^2$ on the Green functions. The same process may be repeated using higher powers of the operators, and it can be seen that commutivity $[\hat{A},\hat{B}-\hat{C}]=0$, and Equation B.8, together would imply that $\hat{A}^n$ is equivalent to $(\hat{B}-\hat{C})^n$ when acting on the Green functions for all positive integers n.

As a counter-example, consider the function $f(x)=x^2$. For this function it is true that $\frac{\partial f}{\partial x}=\frac{2}{x}f(x)$. However, it can be seen that the operators $\frac{\partial}{\partial x}$ and $\frac{2}{x}$ do not commute, and in this case $\frac{\partial^2 f}{\partial x^2}\neq(\frac{2}{x})^2 f$. Thus this is consistent with operator commutivity being required for operator equivalence under repeated application.

It can be seen from the operator definitions in B.11 that $\hat{A}$ and $\hat{B}-\hat{C}$ do indeed commute. It is apparent that $\hat{A}$ and $\hat{B}$ commute since partial derivatives commute; $\hat{A}$ and $\hat{C}$ commute as $\hat{C}$ depends only on the chemical potential field which is here a function only of the y dimension, and this commutes with the arc-length partial derivative which is $\hat{A}$. Altogether then, the operators $\hat{A}$ and $\hat{B}-\hat{C}$ commute and combined with Equation B.8 this implies that they are equivalent under repeated application to the Green functions.

The equivalence of the operators $\hat{A}$ and $\hat{B} - \hat{C}$ means that the arc-length propagator may be re-expressed:

$$G_y(y, y'; N_s + \Delta N) = \exp\left[\Delta N \left(\hat{B} - \hat{C}\right)\right] G_y(y, y'; N_s)$$
$$= \exp\left[\Delta N \left(\frac{b^2}{6}\frac{\partial^2}{\partial y^2} - \frac{\omega(y)}{\mathrm{k_B}T}\right)\right] G_y(y, y'; N_s) \quad \text{(B.13)}$$

The arc-length propagator as given in Equation B.13 can be used to solve for $G_y(y, y'; N_s)$. A computationally efficient way to apply the operator in Equation B.13 is to approximate it in the following way:

$$\exp\left[\Delta N \left(\frac{b^2}{6}\frac{\partial^2}{\partial y^2} - \frac{\omega(y)}{\mathrm{k_B}T}\right)\right] \approx \exp\left[-\frac{\Delta N}{2}\frac{\omega(y)}{\mathrm{k_B}T}\right] \exp\left[\Delta N \frac{b^2}{6}\frac{\partial^2}{\partial y^2}\right] \exp\left[-\frac{\Delta N}{2}\frac{\omega(y)}{\mathrm{k_B}T}\right] \quad \text{(B.14)}$$

Comparing the series expansions (with respect to ΔN) of the expressions on the left and right sides of Equation B.14 it is found that the leading terms are equal until the ΔN^3 term is reached, and is thus an approximate expression for the propagator accurate up to this order.

The approximate operator on the right side of Equation B.14 can be conveniently computationally implemented because the outside portions with $\exp\left[-\frac{\Delta N}{2}\frac{\omega(y)}{\mathrm{k_B}T}\right]$ can be implemented by simple multiplication down the y dimension of the G function array. The interior portion with $\exp\left[\Delta N \frac{b^2}{6}\frac{\partial^2}{\partial y^2}\right]$ can be implemented by simple multiplication after first taking the G function array into Fourier space via a fast Fourier transform; in Fourier space this interior portion of the operator becomes $\exp\left[-\Delta N \frac{b^2}{6} k_y^2\right]$, with k_y being the y dimension wave vector.

If the transform to Fourier space is represented by $\mathcal{F}$ and the inverse transform by $\mathcal{F}^{-1}$, then the computational algorithm used to solve for the polymer strand Green

functions can be expressed by the following equation:

$$G_y(y, y'; N_s + \Delta N) = \exp\left[-\frac{\Delta N}{2}\frac{\omega(y)}{\mathrm{k_B}T}\right]\mathcal{F}^{-1}\exp\left[-\Delta N\frac{b^2}{6}k_y^2\right]\mathcal{F}\exp\left[-\frac{\Delta N}{2}\frac{\omega(y)}{\mathrm{k_B}T}\right]G_y(y, y'; N_s) \quad \text{(B.15)}$$

In this algorithmic equation the exponential operators are applied by multiplication down the Green function array (in the relevant space, either real or Fourier). This algorithm is known as a pseudo-spectral method.

A further step is performed to increase the numerical accuracy of the solving algorithm. The algorithm described in Equation B.15 results in a global numerical error of order ΔN^2. The leading order error term can be subtracted off by a process now described. During each application of the propagator the next value of the Green function can be solved for twice, once using arc-length step ΔN, and once using two applications of the propagator with halved arc-length step $\Delta N/2$. Combining calculated with the full and halved arc-length in the following way subtracts of the leading error term:

$$G(y, y'; N_s) = (4G_{\Delta N/2} - G_{\Delta N})/3 \quad \text{(B.16)}$$

Here $G_{\Delta N}$ is the Green function calculated via the pseudo-spectral method with arc-length step ΔN, and $G_{\Delta N/2}$ is the Green function calculated with half the arc-length step. Combining the results of these two calculations according to Equation B.16 results in a Green function accurate to ΔN^4 (because of the symmetry of the propagators in the pseudo-spectral method the error terms are only of even powers of ΔN). The q functions are calculated in an analogous way with the same accuracy (the q function calculation proceeds along exactly the same lines as the Green function calculation except for a boundary condition difference).